



저작자표시-비영리-변경금지 2.0 대한민국

이용자는 아래의 조건을 따르는 경우에 한하여 자유롭게

- 이 저작물을 복제, 배포, 전송, 전시, 공연 및 방송할 수 있습니다.

다음과 같은 조건을 따라야 합니다:



저작자표시. 귀하는 원저작자를 표시하여야 합니다.



비영리. 귀하는 이 저작물을 영리 목적으로 이용할 수 없습니다.



변경금지. 귀하는 이 저작물을 개작, 변형 또는 가공할 수 없습니다.

- 귀하는, 이 저작물의 재이용이나 배포의 경우, 이 저작물에 적용된 이용허락조건을 명확하게 나타내어야 합니다.
- 저작권자로부터 별도의 허가를 받으면 이러한 조건들은 적용되지 않습니다.

저작권법에 따른 이용자의 권리는 위의 내용에 의하여 영향을 받지 않습니다.

이것은 [이용허락규약\(Legal Code\)](#)을 이해하기 쉽게 요약한 것입니다.

[Disclaimer](#)

工學博士學位論文

**Fabrication of Metal Nanoparticle Embedded  
Multichannel Carbon Nanofiber  
for Bio/Chemical Sensor Applications**

금속 나노입자가 도입된 다채널 탄소 나노 섬유 제조  
및 바이오/화학 센서로의 응용

2020年 8月

서울대학교 大學院

化學生物工學部

金 成 根

**Fabrication of Metal Nanoparticle Embedded  
Multichannel Carbon Nanofiber  
for Bio/Chemical Sensor Applications**

2020年

金成根

↑  
2cm  
↓

↑  
2.5cm  
↓

↑  
4cm  
↓

↑  
3cm  
↓

↑  
2cm  
↓

**Fabrication of Metal Nanoparticle Embedded  
Multichannel Carbon Nanofiber  
for Bio/Chemical Sensor Applications**

**금속 나노입자가 도입된 다채널 탄소 나노 섬유 제조  
및 바이오/화학 센서로의 응용**

指導教授 張 正 植

이 論文을 工學博士 學位論文으로 提出함  
2020 年 6 月  
서울大學校 大學院  
化學生物工學部  
金 成 根

金成根의 工學博士 學位論文을 認准함  
2020 年 6 月

委 員 長 \_\_\_\_\_ (印)

副委員長 \_\_\_\_\_ (印)

委 員 \_\_\_\_\_ (印)

委 員 \_\_\_\_\_ (印)

委 員 \_\_\_\_\_ (印)

**Fabrication of Metal Nanoparticle Embedded  
Multichannel Carbon Nanofiber  
for Bio/Chemical Sensor Applications**

by

Sung Gun Kim

Submitted to the Graduate School of Seoul National  
University in Partial Fulfillment of the Requirements for  
the Degree of Doctor of Philosophy

August, 2020

Thesis Adviser: Jyongsik Jang

## **Abstract**

In recent decades, nanomaterial research and the synthesis methods of novel nanomaterials with improved physical, chemical, and electrical properties are continuously expanding frontier at the material science. Among them, conductive nanomaterials including conducting polymers, nanostructured metal composite, and carbon nanomaterials have been studied because of their unique properties. One-dimensional (1D) conductive nanomaterials have been shown to be particularly effective sensor transducers due to their simple structure properties such as high aspect ratio and high specific surface area, and fast directional charge transport characteristics. One of the 1D conductive nanomaterials, carbon nanomaterials are important for electrochemical and biological applications since their surface can be easily modified using a variety of covalent or  $\pi$ -stacking methods. Especially, carbon nanofibers (CNFs) can be obtained via a simple electrospinning method, one of the methods for manufacturing 1D nanomaterials using a viscous polymer solution, has advantages relatively in terms of efficiency, cost, yield, and reproducibility. Electrospun CNFs are particularly attractive for sensing applications

because their electrochemical properties and structures can be easily controlled by varying the process conditions, including temperature, spinning solution component, precursor composition, etc. However, there remain some challenges such as the production of multidimensional nanofibers or hybrid nanomaterials require the optimization of a stable process for electrochemical and structural benefits.

This dissertation describes the fabrication of various hybrid materials using electrospun PAN-based multichannel carbon nanofibers for bio and chemical sensor applications. The multichannel carbon nanofibers were fabricated through single-nozzle co-electrospinning and heat treatment. It was confirmed that multichannel carbon nanofiber has utility as a sensor transducer through the biosensor applications. Firstly, bio-receptors-modified multichannel carbon nanofibers were prepared using the acid treatment and following catalytic reaction between the carboxyl group of the multichannel carbon nanofibers and the amine group of the bio-receptors. According to the bio-receptors, aptamers were applied for detecting the endocrine disruptor (bisphenol-A, BPA) and antibodies

were applied for detecting the salivary epilepsy biomarker (nesfatin-1, NES1).

Secondly, noble metal (Ru) and metal oxide ( $\text{Fe}_2\text{O}_3$ ) nanoparticles-embedded multichannel carbon nanofibers were suggested by the facile method including oxygen plasma treatment before heat treatment. The ruthenium nanoparticles-embedded multichannel carbon nanofibers (Ru-mCNFs) were applied for detecting neurotransmitter molecule (dopamine) and the iron oxide nanoparticles-embedded multichannel carbon nanofibers (Fe-mCNFs) were applied for detecting toxic gas (hydrogen sulfide).

This dissertation provides the possibility and facile fabrication methods of various types of multichannel carbon nanofibers-based hybrid nanomaterials exhibited ultrahigh ability in the bio/chemical sensor application due to its large active surface area originated from the multichannel and porous structure. The nanomaterials presented in this dissertation could be applied to various sensing systems such as liquid-ion-gated bio-receptor (aptamer or antibody) field-effect-transistor (FET) sensor, non-enzymatic FET sensor, and toxic gas wireless chemical sensor platform.

**Keywords:** multichannel carbon nanofiber; metal nanoparticles; endocrine disruptor; salivary epilepsy biomarker; neurotransmitter; toxic gas; sensor.

**Student Number:** 2014-21583

## **List of Abbreviations**

nm: nanometer

CPS: conducting polymers

1D: One-dimensional

PVA: poly(vinyl alcohol)

PI: polyimide

PVP: poly(vinyl pyrrolidone)

PAN: poly(acrylonitrile)

CVD: chemical vapor deposition

Au: gold

Pt: platinum

Pd: palladium

Ru: ruthenium

OER: oxygen evolution reaction

ORR: oxygen reduction reaction

FET: field-effect-transistor

S/N: signal-to-noise

BPA: bisphenol-A

EDC: endocrine-disrupting compound

ERs: estrogen receptors

MRL: maximum residue limit

TDI: tolerable daily intake

EFSA: European Food Safety Authority

HPLC: high-performance liquid chromatography

GC/MS: gas chromatography coupled with mass spectrometry

EEG: electroencephalography

PRL: prolactin

ESs: epileptic seizures

PVN: paraventricular nucleus

ARC: arcuate nucleus

NTs: neurotransmitters

DA: dopamine

n: nano

$\mu$ : micro

p: pico

f: femto

M: molar concentration

pH: potential of hydrogen

H<sub>2</sub>S: hydrogen sulfide

RFID: radio frequency identification

LF: low-frequency

HF: high-frequency

UHF: ultrahigh-frequency

kHz: kilohertz

MHz: megahertz

GHz: gigahertz

PMMA: poly(methyl methacrylate)

DMF: *N,N*-dimethylformamide

BPB: bisphenol-B

VA: 4,4-bis(4-hydroxyphenyl) valeric acid

BP: 4,4'-dihydroxybiphenyl, 4,4'-biphenol

6F: 4,4'-(hexafluoro-isopropylidene) diphenol

A: adenine

T: thymine

G: guanine

C: cytosine

DEPC: diethylpyrocarbonate

PC: polycarbonate

NES1: nesfatin-1

$M_w$ : molecular weight

‰: percent

wt‰: weight percent

°C: Celsius degree

eV: electron volt

RT: room temperature

*ex-situ*: off-site conservation

*in-situ*: in-site conservation

h: hour

rpm: revolutions per minute

ml: milliliter

min: minute

g: gram

IDA: interdigitated micro array

s: second

ppm: part of million

A: ampere

APS: 3-aminopropyltrimethoxysilane

DMT-MM: 4-(4,6-Dimethoxy-1,3,5-triazin-2-yl)-4-methyl-  
morpholinium chloride

CNF: PAN-based carbon nanofiber

MCNF: PAN/PMMA-based multichannel carbon nanofiber

cCNF: carboxyl-functionalized CNF

cmCNF: carboxyl-functionalized MCNF

A-MCNF: aptamer-modified MCNF

Ab-CNF: antibody-modified CNF

Ab-MCNF: antibody-modified MCNF

FE-SEM: field-emission scanning electron microscopy

HR-TEM: high-resolution transmission electron microscopy

TEM: transmission electron microscopy

CBERF: chemical & biological engineering research facilities

NCIRF: national center for inter-university research facilities

RIAM: research institute of advanced materials

BET: Brunauer-Emmett-Teller

BJH: Barrett-Joyner-Halenda

FTIR: Fourier-transform infrared spectroscopy

ATR: attenuated total reflection

XPS: X-ray photoelectron spectroscopy

XRD: X-ray diffraction

μm: micro-meter

PS: polystyrene

EP: epinephrine

NE: norepinephrine

PEA: phenethylamine

TR: tyrosine

AA: ascorbic acid

UA: uric acid

mCNF: PAN/PS-based multichannel carbon nanofiber

Ru-mCNF: ruthenium nanoparticles-embedded mCNF

Fe-mCNF: iron oxide nanoparticles-embedded mCNF

EELS: electron energy loss spectroscopy

EDS: energy dispersive spectroscopy

W: watt

MFC: mass flow controller

IC: integrated circuit

hcp: hexagonal close packed

a.u.: arbitrary unit

S: electrical conductivity

cm: centi-meter

I: current

V: voltage

SD: source-drain

MDL: minimum detectable level

NP: nanoparticle

Re: reflectance

dB: decibel

## List of Figures

- Figure 1.** Dimensionality classification of nanostructures
- Figure 2.** Classification of nanostructured materials from the point of view of nanostructures dimensions, morphology, composition, uniformity, and agglomeration state
- Figure 3.** (a) The structure of polyacetylene: The backbone contains conjugated double bonds. (b) The general conductivity range of conducting polymers (CPs).
- Figure 4.** Possible chemical structures in polypyrrole chains
- Figure 5.** Carbon allotropes in different dimensions
- Figure 6.** (a) Atomic structure of a carbon atom. (b) Energy levels of outer electrons in carbon atoms. (c) The formation of  $sp^2$  hybrids. (d) The crystal lattice of graphene, where A and B are carbon atoms belonging to different sub-lattices,  $a_1$  and  $a_2$  are unit-cell vectors. (e) Sigma bond and pi bond formed by  $sp^2$  hybridization.
- Figure 7.** Classification of 1D nanostructures
- Figure 8.** Schematic diagram of preparing electrospun nanofibers *via* electrospinning

- Figure 9.** Schematic diagram of the diverse variables affecting electrospinning
- Figure 10.** Illustration of electrospun fibers with multilevel micro-/nanostructures and their applications
- Figure 11.** Plausible mechanistic pathways for the thermo-oxidative stabilization of PAN, followed by carbonization
- Figure 12.** Surface functionalization of carbon nanotubes
- Figure 13.** Schematic diagram of the plasma system for the stabilization process
- Figure 14.** The suggested mechanism of thermal stabilization of electron-irradiated PAN fibers
- Figure 15.** Top-down and bottom-up approaches for producing controlled nanomaterials
- Figure 16.** Schematic explanation of sensor mechanism
- Figure 17.** Components of a typical biosensor
- Figure 18.** Schematic illustration of liquid-ion-gated FET-type sensor
- Figure 19.** Schematic diagram of the resistive-type gas sensor setup
- Figure 20.** Schematic illustration of electrical gas sensing process
- Figure 21.** Examples of active and passive RFID sensors. Active sensors with (a) thin-film and (b) AAA-type batteries.

Passive sensors with an analog input into an IC memory chip for operation at (c) LF, (d) HF, and (e) UHF frequency ranges; (f) passive sensor based on a common HF RFID tag with a sensing material applied directly to the resonant antenna of the sensor.

**Figure 22.** Schematic diagram of the single-nozzle co-electrospinning method. The upper insets show optical micrographs of the PAN/PMMA and PAN/PS phase-separated blend. The lower inset is a schematic diagram of multicore polymer nanofiber generation during electrospinning.

**Figure 23.** Schematic illustration and (inset) optical micrograph of the interdigitated micro array (IDA) on the glass substrate

**Figure 24.** Schematic diagram of the carboxyl-functionalized multi-channel carbon nanofiber (cMCNF)

**Figure 25.** (a), (d) FE-SEM and TEM micrographs show the multicore nanofiber and PAN nanofiber, (b), (e) FE-SEM micrographs of the multichannel carbon nanofiber (MCNF) and PAN carbon nanofiber (CNF). The insets of (b) and (e) show the magnified cross-section of MCNF and CNF. (c), (f) TEM micrographs of cMCNF and cCNF.

**Figure 26.** FE-SEM micrographs of the over-oxidized MCNFs. The inset shows a magnified image of a MCNF with collapsed multichannel structure when oxidized more than 12 h.

**Figure 27.** FTIR spectra of MCNFs and the cMCNFs formed with oxidation times of 2, 6, and 12 h.

**Figure 28.** XPS C (1s) survey spectra of MCNFs and the cMCNFs formed with oxidation times of 2, 6, and 12 h.

**Figure 29.** Schematic diagram of the immobilization of bio-receptors-modified cMCNFs on the electrode

**Figure 30.** TEM micrographs of (a) aptamer-modified MCNF (A-MCNF), (b) antibody-modified MCNF (Ab-MCNF), and (c) antibody-modified CNF (Ab-CNF). The insets are FE-SEM micrographs of the A-MCNF, Ab-MCNF, and Ab-CNF on the IDA electrode, respectively.

**Figure 31.** (a) N<sub>2</sub> adsorption-desorption isotherm curve (BET surface area: 798.25 m<sup>2</sup>g<sup>-1</sup>) and (b) Barrett-Joyner-Halenda (BJH) pore-size distribution curve for MCNFs.

**Figure 32.** (a) Source-drain current-voltage ( $I_{SD}$ - $V_{SD}$ ) curves of sensors formed using A-MCNFs are shown for oxidation times of 2, 6, and 12 h following the introduction of BPA-

binding aptamers. (b)  $I_{SD}$ - $V_{SD}$  characteristics of A-MCNFs FET electrodes are shown for gate voltages of  $-1.0 \text{ V} \leq V_g \leq +0.8 \text{ V}$  in steps of  $0.2 \text{ V}$  with a  $V_{SD}$  scan rate of  $10 \text{ mV s}^{-1}$ .

**Figure 33.** (a) Real-time response of the normalized current (i.e.,  $[\Delta I/I_0]_{SD} \times 100$ ) of A-MCNFs FET sensors formed with various oxidation times. (b) Calibration curves of FET sensors formed with various acid treatment times as a function of BPA concentration. Here  $S$  denotes the normalized current following 10 s of exposure to the BPA solution. Dark cyan, blue, and red correspond to oxidation times of 2, 6, and 12 h, respectively. The gate bias was  $V_g = 50 \text{ mV}$  and the source-drain bias was  $V_{SD} = 50 \text{ mV}$ .

**Figure 34.** Schematic diagram of the sensing mechanism of liquid-ion-gated FET sensor.

**Figure 35.** The real-time response of A-MCNFs FET sensor (a) to BPA structural analogs BPB, VA, 6F and BP, (b) to various analytes before and after being mixed with BPA, (c) to actual BPA extracted samples (real sample 1: polycarbonate (PC) bottle, sample 2: thermal printing

paper). The gate bias was  $V_g = 50$  mV and the source-drain bias was  $V_{SD} = 50$  mV.

**Figure 36.** Molecular diagrams of the structural analogs of BPA. (a) 4,4'-(propane-2,2-diyl)diphenol (Bisphenol-A, BPA), (b) 4,4'-(butane-2,2-diyl) diphenol (Bisphenol B, BPB), (c) 4,4-Bis(4-hydroxyphenyl) valeric acid (VA), (d) 4,4'-(hexafluoroisopropylidene) diphenol (6F), and (e) 4,4'-dihydroxybiphenyl (4,4'-Biphenol, BP).

**Figure 37.** Stability of the A-MCNFs FET sensors measured over 4 weeks with intervals of 7 days. Dark cyan, blue, and red correspond to oxidation times of 2, 6, and 12 h, respectively.

**Figure 38.** (a) Source-drain current-voltage ( $I_{SD}$ - $V_{SD}$ ) curves of sensors formed using Ab-CNFs and Ab-MCNFs which are shown with or without NES1-binding antibody.  $I_{SD}$ - $V_{SD}$  characteristics of (b) Ab-CNF and (c) Ab-MCNFs FET electrodes are shown for gate voltages of  $-0.8 \text{ V} \leq V_g \leq +0.8 \text{ V}$  in steps of 0.2 V with a  $V_{SD}$  scan rate of  $10 \text{ mV s}^{-1}$ .

**Figure 39.** (a) Real-time response of the normalized current of Ab-CNFs and Ab-MCNFs FET sensors. (b) Calibration curves

of FET sensors formed as a function of NES1 concentration. Here  $S$  denotes the normalized current following 10 s of exposure to the NES1 in PBS solution. The gate bias was  $V_g = 50$  mV and the source-drain bias was  $V_{SD} = 50$  mV.

**Figure 40.** The real-time response of Ab-MCNFs FET sensor (a) to non-target (glucose, hepatitis B, cortisol) and target (NES1), (b) to various analytes before and after being mixed with NES1. The gate bias was  $V_g = 50$  mV and the source-drain bias was  $V_{SD} = 50$  mV.

**Figure 41.** (a) Real-time response of the normalized current and (b) calibration curve of Ab-MCNFs FET sensor as various concentrations of NES1 in artificial saliva solution. The gate bias was  $V_g = 50$  mV and the source-drain bias was  $V_{SD} = 50$  mV.

**Figure 42.** Illustration of the sequential synthesis of the Ru-mCNF. (The inset: structural changes of the electrospun multicore nanofibers after each fabrication step.)

**Figure 43.** Fourier-transform infrared (FTIR) spectra of the electrospun multicore nanofibers (PAN/PS/RuCl<sub>3</sub>) before (black)

and after (red) oxygen plasma treatment.

**Figure 44.** (a) TEM and (b) HR-TEM images of stabilized multicore nanofiber after oxygen plasma.

**Figure 45.** (a), (d) FE-SEM micrographs show the multicore nanofiber without or with ruthenium precursor, (b), (e) FE-SEM micrographs of the multichannel carbon nanofiber (mCNF) and ruthenium nanoparticles-embedded mCNF (Ru-mCNF). The insets of (b) and (e) show the magnified cross-section of mCNF and Ru-mCNF. (c), (f) TEM micrographs of mCNF and Ru-mCNF. The inset of (f) show a high-resolution TEM (HR-TEM) image of the ruthenium nanoparticle component in the carbon nanofiber structure.

**Figure 46.** Electron energy-loss spectroscopy (EELS) dot mapping of the Ru-mCNF (cyan: C, yellow: Ru, magenta: O, red: N)

**Figure 47.** X-ray diffraction (XRD) spectra of mCNF (black) and Ru-mCNF (red).

**Figure 48.** X-ray photoelectron spectroscopy (XPS) spectra of (a) Ru-mCNF and mCNF, (b) High-resolution Ru3p XPS spectra of Ru-mCNF. High-resolution C1s, O1s XPS spectra of

(c), (e) mCNF and (d), (f) Ru-mCNF.

**Figure 49.** TEM micrographs of Ru-mCNFs with various amount of ruthenium precursor (0.05, 0.10, 0.15 g) resulting various RuNPs size distribution.

**Figure 50.** Raman spectra of (black) mCNF, (red) Ru-mCNF\_0.05, (blue) Ru-mCNF\_0.10, and (dark cyan) Ru-mCNF\_0.15.

**Figure 51.** Schematic illustration of the liquid-ion-gated FET with the immobilized Ru-mCNF arrays on the IDA electrode.

**Figure 52.** (a) Source-drain current-voltage ( $I_{SD}$ - $V_{SD}$ ) curves of sensors with mCNF, Ru-mCNF\_0.05, Ru-mCNF\_0.10, and Ru-mCNF\_0.15. (b)  $I_{SD}$ - $V_{SD}$  characteristics of Ru-mCNFs FET electrodes are shown for gate voltages of  $-0.8 \text{ V} \leq V_g \leq +0.6 \text{ V}$  in steps of 0.2 V with a  $V_{SD}$  scan rate of  $10 \text{ mV s}^{-1}$ .

**Figure 53.** Schematic diagram of the dopamine sensing mechanism of liquid-ion-gated non-enzymatic FET sensor.

**Figure 54.** (a) Real-time response of the normalized current (i.e.,  $[\Delta I/I_0]_{SD} \times 100$ ) of Ru-mCNFs FET sensors. (b) Calibration curves of FET sensors formed with various ruthenium amount as a function of DA concentration.

Here  $S$  denotes the normalized current following 10 s of exposure to the DA solution. Dark cyan, blue, and red correspond to ruthenium precursor 0.05, 0.10, and 0.15 g, respectively. The gate bias was  $V_g = 50$  mV and the source-drain bias was  $V_{SD} = 50$  mV.

**Figure 55.** The real-time response of Ru-mCNFs FET sensor (a) to various non-target (phenethylamine (PEA), tyrosine (TR), ascorbic acid (AA), uric acid (UA), epinephrine (EP), and norepinephrine (NE)) analytes and target (dopamine (DA)), and (b) to various analytes before and after being mixed with NES1. The gate bias was  $V_g = 50$  mV and the source-drain bias was  $V_{SD} = 50$  mV.

**Figure 56.** Molecular diagrams of (a) dopamine (DA), (b) epinephrine (EP), (c) norepinephrine (NE), (d) phenethylamine (PEA), (e) tyrosine (TR), (f) ascorbic acid (AA), and (g) uric acid (UA).

**Figure 57.** Stability of the Ru-mCNFs FET sensors measured over 4 weeks with intervals of 7 days. Dark cyan, blue, and red correspond to Ru-mCNF\_0.05, Ru-mCNF\_0.10, and Ru-mCNF\_0.15, respectively.

**Figure 58.** Illustration of the sequential synthesis of the Fe-mCNF (The inset: structural changes of the electrospun multicore nanofibers after each fabrication step.)

**Figure 59.** Fourier-transform infrared (FTIR) spectra of the electrospun multicore nanofibers (PAN/PS/FeCl<sub>3</sub>) before (black) and after (red) oxygen plasma treatment

**Figure 60.** (a)~(c) High-magnified and (d)~(f) low-magnified TEM micrographs of Fe-mCNFs with various amount of Fe precursor (0.10, 0.16, 0.24 g) resulting various Fe<sub>2</sub>O<sub>3</sub> NPs size distribution.

**Figure 61.** (a) Scanning TEM and energy dispersive spectroscopy (STEM-EDS) line mapping of the Fe-mCNF. (b)~(f) Electron energy-loss spectroscopy (EELS) dot mapping of the Fe-mCNF (cyan: C, green: Fe, magenta: O, red: N).

**Figure 62.** High-resolution TEM (HR-TEM) image of Fe<sub>2</sub>O<sub>3</sub> nanoparticle component in the carbon nanofiber structure

**Figure 63.** X-ray diffraction (XRD) spectra of mCNF (black) and Fe-mCNF (red).

**Figure 64.** Raman spectra of (black) mCNF, (red) Fe-mCNF\_0.10, (blue) Fe-mCNF\_0.16, and (dark cyan) Fe-mCNF\_0.24.

**Figure 65.** (a) Source-drain current-voltage ( $I_{SD}$ - $V_{SD}$ ) curves of sensors with mCNF, Fe-mCNF\_0.10, Ru-mCNF\_0.16, and Ru-mCNF\_0.24. Real-time responses of normalized resistance changes of the different Fe-mCNFs at room temperature on (b) sequential exposure to various H<sub>2</sub>S gas concentrations and (c) periodic exposure to 5 ppm of H<sub>2</sub>S gas (at a constant current: 10<sup>-6</sup> A). (d) Calibration curves of the different Fe-mCNFs as a function of various H<sub>2</sub>S gas concentration. (dark cyan: Fe-mCNF\_0.10; red: Fe-mCNF\_0.16; blue: Fe-mCNF\_0.24)

**Figure 66.** Schematic diagram of the H<sub>2</sub>S sensing mechanism of the Fe-mCNF sensor

**Figure 67.** Stability of the Fe-mCNFs FET sensors measured over 20 days with intervals of 5 days. Dark cyan, red, and blue correspond to Fe-mCNF\_0.10, Fe-mCNF\_0.16, and Fe-mCNF\_0.24, respectively.

**Figure 68.** Schematic diagram of the RFID based-wireless sensor system consisting of reader antenna-connected network analyzer and a sensor tag

**Figure 69.** (a) Schematic diagram of the sequential fabrication

process of the RFID sensor tag. (b) Photographs of the RFID-tag sensor under various deformations.

**Figure 70.** (a) Variation of reflectance characteristics of the Fe-mCNF-based wireless sensor with various H<sub>2</sub>S gas concentrations (purple: without; blue: 0.5 ppm; green: 1 ppm, yellow: 5 ppm; orange: 25 ppm; red: 100 ppm). (b) Calibration of reflectance and phase shift curves as a function of the H<sub>2</sub>S concentration.

**Figure 71.** (a) Reflectance change of the wireless sensor system for different distances between RFID sensor tag and antenna with various H<sub>2</sub>S gas concentrations. (b) Reflectance properties under different deformations at 5 ppm (flat, twist, and bend). (c) The normalized reflectance curves under various bending angles at 10 cm distance apart with different H<sub>2</sub>S gas concentrations. (d) The long-term stability of the Fe-mCNF-based wireless sensor under 0.2 ppm H<sub>2</sub>S gas.

## List of Tables

**Table 1.** Performances of various sensors developed for the analysis of bisphenol-A (BPA).

<b>Abstract .....</b>	<b>i</b>
<b>List of Abbreviations .....</b>	<b>v</b>
<b>List of Figures .....</b>	<b>xii</b>
<b>List of Tables.....</b>	<b>xxv</b>
<b>Table of Contents.....</b>	<b>xxvi</b>
<b>1. Introduction .....</b>	<b>1</b>
<b>1.1. Background .....</b>	<b>1</b>
1.1.1. Conductive nanomaterial.....	1
1.1.1.1. One-dimensional (1D) nanomaterial .....	10
1.1.1.1.1. Electrospinning method.....	12
1.1.1.1.2. Electrospinning-based carbon nanomaterial.....	17
1.1.1.2. Hybrid nanomaterial .....	24
1.1.1.2.1. Noble metal/carbon nanomaterial.....	27
1.1.1.2.2. Metal oxide/carbon nanomaterial .....	28
1.1.2. Sensor application .....	29
1.1.2.1. Liquid-ion-gated FET biosensor.....	31
1.1.2.1.1. Bisphenol-A (BPA) sensor.....	34
1.1.2.1.2. Nesfatin-1 (NES1) sensor.....	36
1.1.2.1.3. Dopamine (DA) sensor.....	38
1.1.2.2. Resistive type chemical sensor .....	40

1.1.2.2.1. Hydrogen sulfide (H <sub>2</sub> S) sensor .....	44
1.1.2.3 Wireless sensor .....	45
1.1.2.3.1. RFID wireless sensor.....	46
<b>1.2. Objectives and Outlines .....</b>	<b>48</b>
1.2.1. Objectives .....	48
1.2.2. Outlines.....	49
<b>2. Experimental Details.....</b>	<b>51</b>
<b>2.1. Bio-receptors-modified multichannel carbon nanofibers for liquid-ion-gated FET sensor detecting bisphenol-A and nesfatin-1 .....</b>	<b>51</b>
2.1.1. Fabrication of bio-receptors-modified MCNFs FET sensor (anti-BPA aptamer & anti-NES1 antibody).....	51
2.1.2. Characterization .....	55
2.1.3. Electrical measurement.....	56
<b>2.2. Ruthenium nanoparticles-embedded multichannel carbon nanofibers for liquid-ion-gated non-enzymatic FET sensor detecting dopamine .....</b>	<b>57</b>
2.2.1. Fabrication of Ru-mCNFs non-enzymatic FET sensor .....	57
2.2.2. Characterization .....	59
2.2.3. Electrical measurement.....	60
<b>2.3. Iron oxide nanoparticles-embedded multichannel carbon</b>	

<b>nanofibers for wireless chemical sensor detecting hydrogen sulfide.....</b>	<b>61</b>
2.3.1. Fabrication of Fe-mCNF .....	61
2.3.2. Characterization .....	62
2.3.3. Electrical measurement.....	63
2.3.4. Fabrication of Fe-mCNFs UHF-RFID wireless sensor .....	64
2.3.5. Wireless sensor measurement.....	65
<b>3. Results and Discussion .....</b>	<b>68</b>
<b>3.1. Bio-receptors-modified multichannel carbon nanofibers for liquid-ion-gated FET sensor detecting bisphenol-A and nesfatin-1 .....</b>	<b>68</b>
3.1.1. Fabrication of carboxyl-functionalized MCNFs (cMCNFs) .....	68
3.1.2. Fabrication of bio-receptors-modified MCNFs FET sensors (anti-BPA aptamer & anti-NES1 antibody).....	77
3.1.3. Electrical measurement of anti-BPA aptamer-modified MCNFs (A-MCNFs) FET sensor detecting BPA .....	83
3.1.4. Electrical measurement of anti-NES1 antibody-modified MCNFs (Ab-MCNFs) FET sensor detecting NES1 .....	97
<b>3.2. Ruthenium nanoparticles-embedded multichannel carbon nanofibers for liquid-ion-gated non-enzymatic FET sensor detecting dopamine .....</b>	<b>105</b>
3.2.1. Fabrication of Ru-mCNFs .....	105

3.2.2. Fabrication of Ru-mCNFs non-enzymatic FET sensor ...	120
3.2.3. Electrical measurement of Ru-mCNFs non-enzymatic FET sensor .....	122
<b>3.3. Iron oxide nanoparticles-embedded multichannel carbon nanofibers for resistive type wireless chemical sensor detecting hydrogen sulfide.....</b>	<b>134</b>
3.3.1. Fabrication of Fe-mCNFs .....	134
3.3.2. Electrical measurement of Fe-mCNFs chemical sensor ..	146
3.3.3. Wireless sensor measurement of Fe-mCNFs UHF-RFID wireless sensor .....	153
<b>4. Conclusion.....</b>	<b>161</b>
<b>Reference.....</b>	<b>166</b>
<b>국문초록.....</b>	<b>180</b>

# **1. Introduction**

## **1.1.1. Conductive nanomaterial**

In recent years, the development of materials science and technology achieves higher precision and improved performance through the adjustment at the extremely small size dimension. Nanotechnology relates to the production of functional materials and structures of these nano-sized materials in the 1 to 100 nm range using chemical and physical methods and application areas [1-8]. Size control of nanoscale material leads to superior physical and chemical properties with molecular and supramolecular structure. Enhanced novel nanostructured materials and devices can be generated by the combination of nano-building units and the strategies which assemble nanostructures into the ordered array to render them functional and operative.

Nanomaterials are divided into nano-sized metals, metal oxides, semiconductors, biomaterials, oligomers, and polymers. Structurally, nanomaterials include various forms of 0, 1, 2, and 3-dimensional structures such as nanoparticles, core-shell nanostructures, hollow nanospheres, nanofibers, nanotubes, nanopatterns, nano sponges, and

nanocomposites, etc., and compositionally contain single or composite hybrid materials (**Figure 1** and **Figure 2**) [9, 10].

The widespread interest in nanostructured materials stems not only from size differences but mainly from their properties (optical, electrical, mechanical, and chemical performance) differ from those of the bulk materials [11-13]. These phenomena, occurring not only in nano-sized filler effects but also in quantum chemical effects including quantum confinement and finite-size effects, especially have motivated the development of various methods to fabricate metallic, inorganic, and polymeric nanomaterials with selectively adjusting factors such as defects, electronic states, and surface chemistry, etc.

As a result, through such fine control researches, recently nanomaterial research and the synthesis methods of novel nanomaterials with improved physical, chemical, and electrical properties are continuously expanding frontier at the material science. Among them, conductive nanomaterials including conducting polymers, nanostructured metal composite, and carbon nanomaterials have been studied because of their unique properties [14-19]. For example, among the synthetic polymers, conducting polymers have attracted considerable attention as important polymer materials since

their conjugated double-bonded backbone that provides the electronic conductivity after doping with suitable dopants (**Figure 3** and **Figure 4**) [20, 21]. Another example, one of the carbon nanomaterials, graphene is a basic allotrope of carbon in the form of a single layer of atoms in a two-dimensional hexagonal lattice, and its notable electronic properties and stability is due to the  $sp^2$  orbital hybridization (**Figure 5** and **Figure 6**) [22, 23]. Since their surface can be easily modified using a variety of covalent or  $\pi$ -stacking methods, carbon nanomaterials are important for electrochemical and biological applications. With such unique conductivity and characters, conductive nanomaterials applied various fields of research, sensor, energy, catalytic, biomedical, etc.

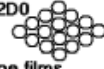
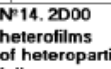
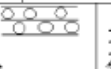
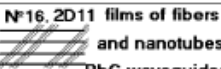
Dimensionality classification of nanostructures ( L < 100 - 500 nm )

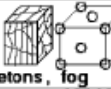
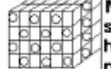
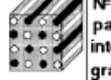
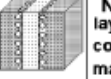
Designation: dimensionality of NS → **kDlmn** ← dimensionality of elementary units  
 $k > l, m, n \quad \{k, l, m, n\} = \{0, 1, 2, 3\}$

Elementary building units :

№1. 0D 	№2. 1D nanotubes, fibers, filaments, whiskers, spirals, belts, springs, horns, columns, needles, pillars, helicoids, wires, ribbons	№3. 2D layers
---	--	------------------

0D-nanostructures :	№4. 0D0 uniform particles arrays 	№5. 0D00 heterogeneous particles arrays, "core-shell" dendrimers, onions 	
1D-nanostructures :	№6. 1D0 molecular chains, polymers 		
№7. 1D00 heteropolymers 	№8. 1D1 bundles, ropes, cables, corals 	№9. 1D11 heterochains, heterocables, saws, hair, heterobundles, junctions, combs, bows 	№10. 1D10 beads, pea-pods, fullereno-fibers 

2D-nanostructures :	№11. 2D0 fullerene films 	№12. 2D1 nanostraw, PhC, fibers films 	
№13. 2D2 tiling, mosaic, layered films 	№14. 2D00 heterofilms of heteroparticles, fullereno-powders 	№15. 2D10 films of pods, fullereno-fibers 	№16. 2D11 films of fibers and nanotubes, PhC-waveguides 
№17. 2D20 fullereno-plate films 	№18. 2D21 bridges, fiber-layer films 	№19. 2D22 hetero-layers, MOS-structures 	№20. 2D210 fullerene-fiber-layer films 

3D-nanostructures :	№21. 3D0 Fullerites, clathrates, powder skeletons, fog 	№22. 3D1 skeletons of fibers, nanotubes 	№23. 3D2 layer skeletons, buildings, honeycombs, foams 	№24. 3D00 sols, colloids, smogs, heteroparticles composites 
№25. 3D10 skeletons of fibers-powders 	№26. 3D11 skeletons of heterofibers, nanotubes 	№27. 3D20 intercalates, skeletons of layers and powders 	№28. 3D21 Cross-bar-layers, layer-fiber skeletons 	
№29. 3D22 heterolayers 	№30. 3D30 opals, dispersions, particles, pores, fullerenes in matrix 	№31. 3D31 membranes, PhC, fiber composites, waveguides 	№32. 3D32 friction pairs, contacts, interfaces, cavities, grain boundaries 	
№33. 3D210 composites of layers, fibers and particles in matrix 	№34. 3D310 membranes + impurities, powder-fiber composites 	№35. 3D320 powder-layers composites 	№36. 3D321 layers-fibers-composites in matrix, VCSEL 	

Notices :

1. Interfaces between building units not regarded as additional 2D-NSs
2. Inverse NSs with cavity building units not regarded as separate ones
3. The classification may be extended with account of fourfold combinations

**Figure 1.** Dimensionality classification of nanostructures [9]

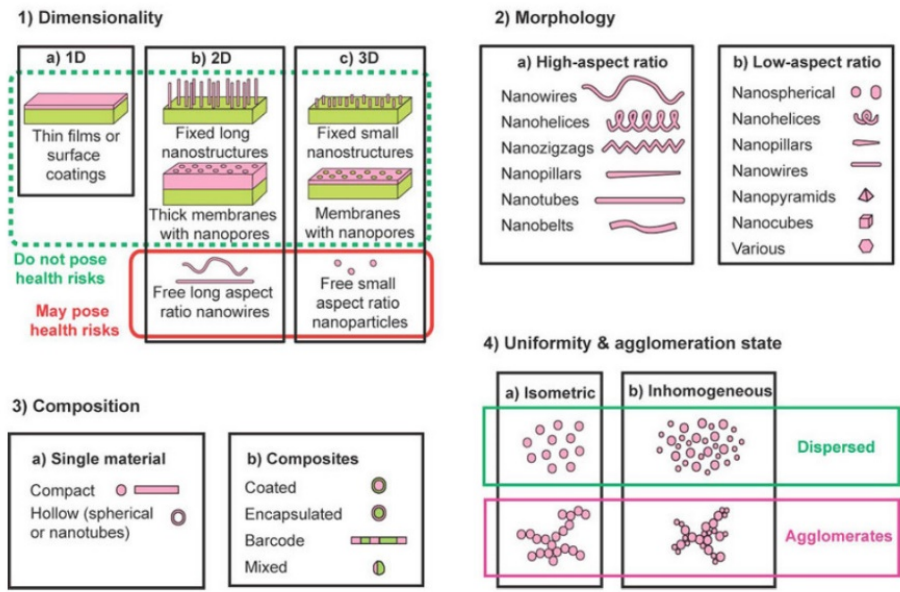


**Figure 2.** Classification of nanostructured materials from the point of view of nanostructures dimensions, morphology, composition, uniformity, and agglomeration state [10]

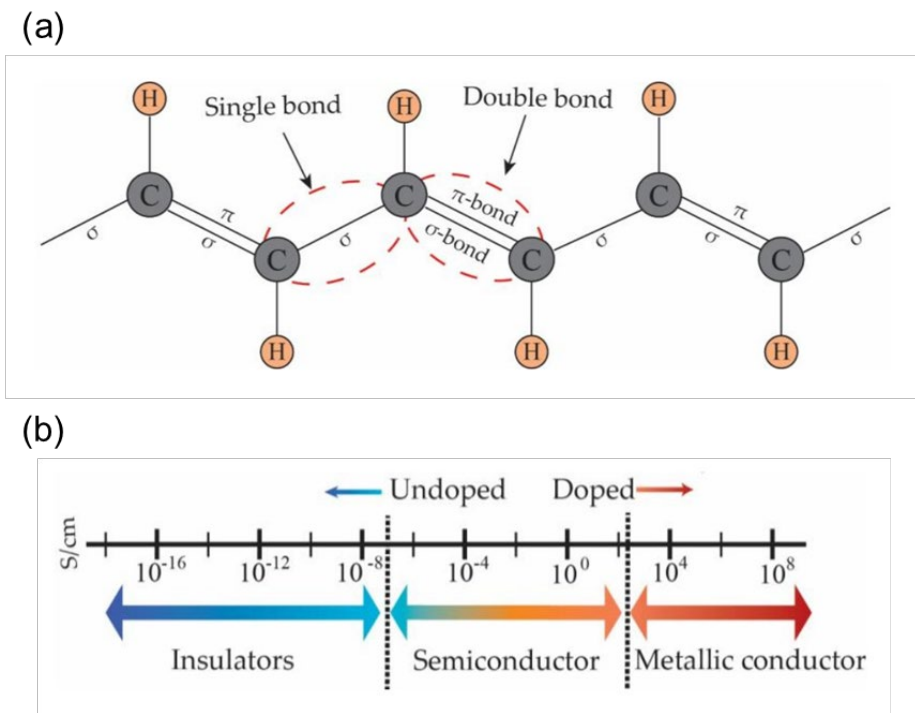


**Figure 3.** (a) The structure of polyacetylene: The backbone contains conjugated double bonds. (b) The general conductivity range of conducting polymers (CPs) [20].

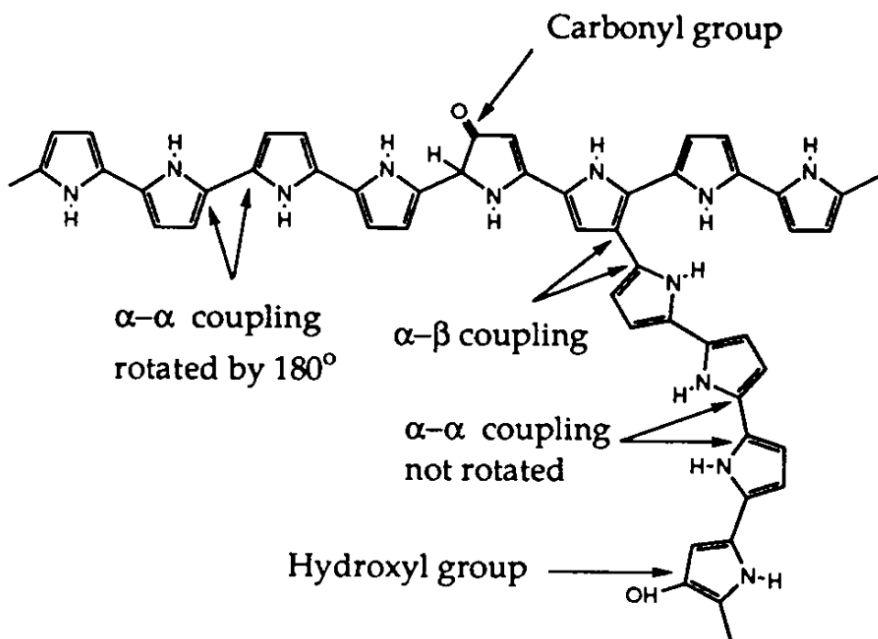


**Figure 4.** Possible chemical structures in polypyrrole chains [21].

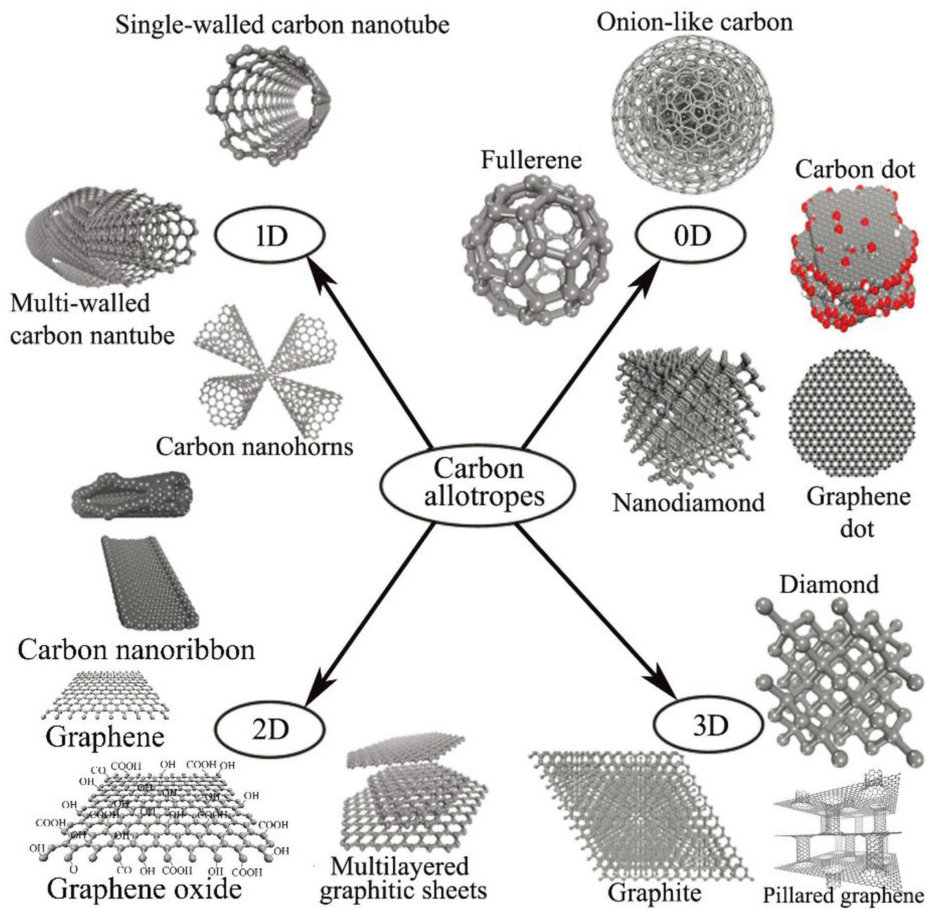


**Figure 5.** Carbon allotropes in different dimensions [22]

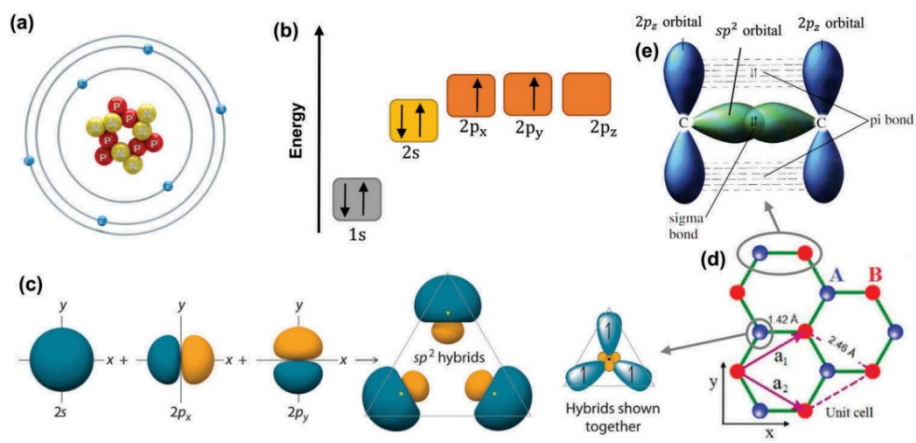


**Figure 6.** (a) Atomic structure of a carbon atom. (b) Energy levels of outer electrons in carbon atoms. (c) The formation of  $sp^2$  hybrids. (d) The crystal lattice of graphene, where A and B are carbon atoms belonging to different sub-lattices,  $a_1$  and  $a_2$  are unit-cell vectors. (e) Sigma bond and pi bond formed by  $sp^2$  hybridization [23].

#### **1.1.1.1. One-dimensional (1D) nanomaterial**

One-dimensional (1D) nanomaterials have received a lot of attention due to their intrinsic properties and potential in various applications such as energy conversion/storage device, catalysts, and sensors [24-35]. The morphological features of the 1D material not only enable more efficient charge carrier movement in the long axis direction but also have a high surface area due to the high aspect ratio. As a basic building block of such nanostructures, 1D nanomaterials such as nanofibers, nanotubes, nanoneedles, nanowires, and nanoribbons have played an important role to construct advanced nanostructures (**Figure 7**) [36].

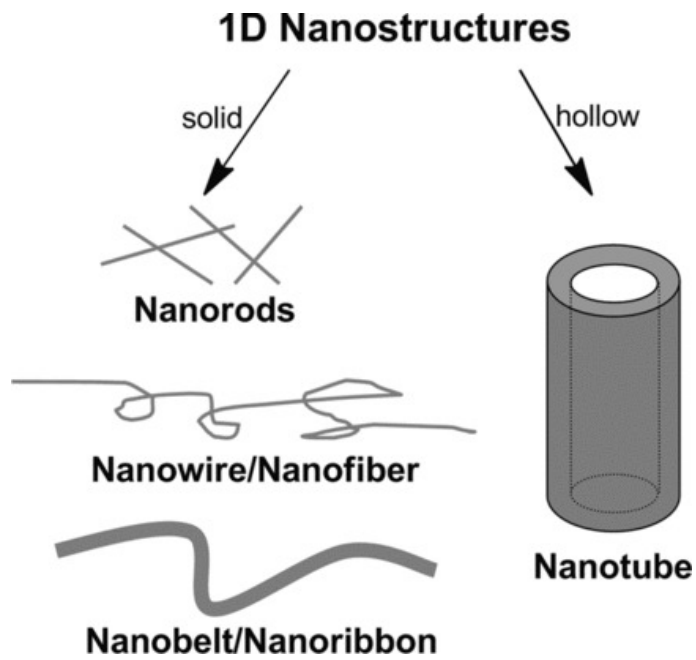


**Figure 7.** Classification of 1D nanostructures [36]

#### **1.1.1.1.1. Electrospinning method**

Electrospinning is an easy and simple way to create 1D materials of various sizes. It is a method of extracting nanofibers by applying high electric force to polymer droplets, which shares the characteristics of electrospray and conventional solution dry spinning but does not require high temperature. Applying a sufficient voltage to the metal needle creates a charge inside the polymer droplet, and the droplet stretches when the applied charge exceeds the surface tension of the polymer solution. When the critical point is exceeded, the liquid flow is ejected from the surface, and if the molecular cohesive force of the liquid is sufficiently high, liquid stream breakage does not occur and a charged polymer liquid jet is formed. The resulting liquid jet is received by the collector in the form of a thin, uniform fiber through elongation and thinning (**Figure 8**) [37-40].

The nanofiber produced by electrospinning can be tuned and prepared by adjusting various parameters such as polymer solution concentration, applied voltage, atmosphere condition, and needle type. In addition, various types of nanofibers could be prepared by using a mixed polymer solution or metal precursor/polymer solution (**Figure 9**) [41]. Lately, the method of preparing carbon or metal/carbon

nanofibers based on heat treatment of electrospun nanofibers is widely studied [42-49].

In particular, the multilevel nanostructured electrospun nanofibers show many attractive changes in properties and functions (**Figure 10**) [50]. These materials are divided into two categories; one is a surface multi-level structures, including branched, porous, necklace-like, and non-cylindrical structures and the other is an internal multilevel structure such as peas, wire-tubes, multiwalled, and multichannel structures. Since the multilevel structures play an important role in enhancing the nano-sized effect by providing a larger specific area and additional heterogeneous interfaces, they exhibit superior properties to bulk or the same size counterparts, which make them widely applicable in sensors, energy storage, catalysis, biomedicine, filtration, etc.

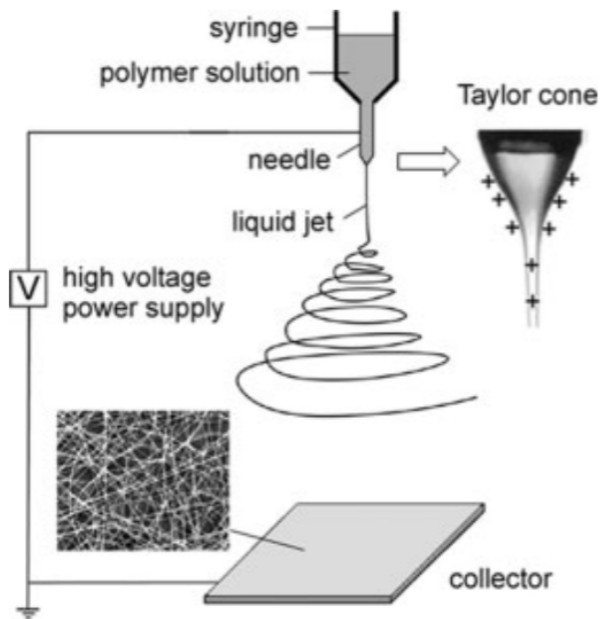


**Figure 8.** Schematic diagram of preparing electrospun nanofibers *via* electrospinning [40]

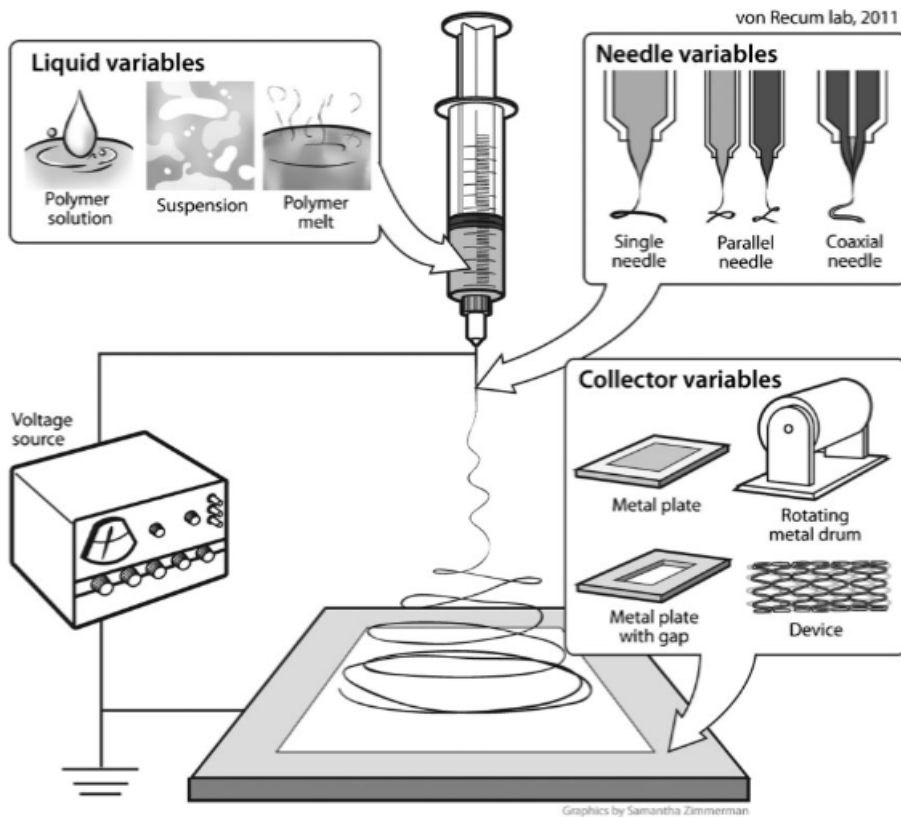


**Figure 9.** Schematic diagram of the diverse variables affecting electrospinning [41]

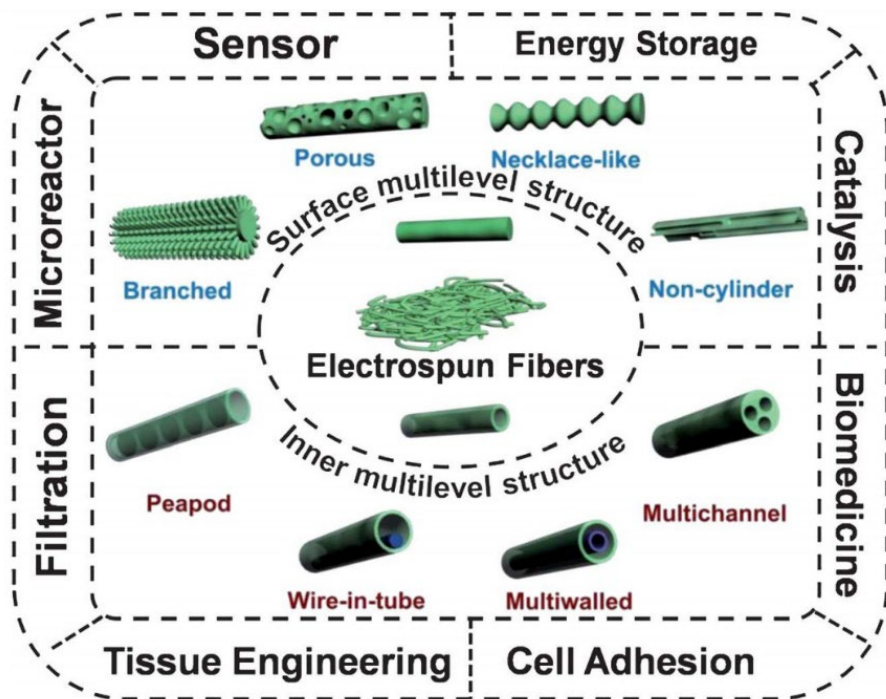


**Figure 10.** Illustration of electrospun fibers with multilevel micro-/nanostructures and their applications [50]

#### **1.1.1.1.2. Electrospinning-based carbon nanomaterial**

Carbon nanomaterial research using electrospun nanofibers has been widely conducted so far, with the advantage of being able to manufacture carbon nanomaterials of various shapes and configurations through a relatively simple method. Various polymers such as poly (vinyl alcohol) (PVA), polyimide (PI), poly (vinyl pyrrolidone) (PVP) and poly (acrylonitrile) (PAN) are used as carbon sources [51-55]. The electrospun nanofibers become carbon nanofibers through a heat stabilization process that converts and carbonizes the aliphatic chain structure into a ring at about 600 to 1000 °C.

Among various polymers, PAN received great interest as a carbon source owing to its unique properties [56-61]. PAN is a semi-crystalline thermoplastic polymer with remarkable properties such as stiffness, chemical stability, carbon abundance, low cost, and ease of deformation to multidimensional structural forms, therefore, it is used as a carbon source precursor for common carbon nanomaterials. The crystallinity of PAN is driven by the high dipole moment of the nitrile group, and these interactions can dissolve PAN in polar organic solvents, inducing a spiral chain structure and hexagonal chain arrangement of PAN.

In order to convert the PAN to the carbon in the heat treatment process of PAN, two steps are carried out: an oxidation stabilization step in which cross-linking, dehydration, oxidation, and partial cyclization proceeds, and a carbonization step in which complete cyclization of these cyclized carbons proceeds. Due to the higher stabilization temperature of PAN as its melting point is 300 °C which is higher than polymers such as PVP (150 °C) and PVA (200 °C), PAN has a relatively high decomposition temperature in air and easier chemical treatment. In addition, the nitrogen in the molecular structure remains after carbonization, making n doping carbon nanofibers (**Figure 11**) [62]. Free radicals occurring at low temperature initiate the oxidative reactions for the cyclization of the nitrile side chains in PAN, and intermolecular condensation of the ladder-like structures with HCN and N<sub>2</sub> generation at high temperature finally results in the graphitic structures.

In recent years, researches have been carried out to change the surface and structural morphology of the electrospun carbon nanofibers using various methods such as multilevel nanostructured polymer, chemical vapor deposition (CVD), mixing precursors, chemical treatment, etc. Especially, porous one-dimensional nanomaterials

produced by methods such as a multilevel nanostructure polymer-based polymer blend carbonization method, have received great attention due to their large specific surface area and high aspect ratio [63-73]. For biological and electrochemical applications, the surface of carbon nanomaterials can be easily functionalized using various chemical treatments to apply covalent or  $\pi$ -stacking methods (**Figure 12**) [74, 75]. Furthermore, researches for more time-efficient and performance-enhancing heat treatment methods have been carried out using plasma or e-beam treatment, etc. (**Figure 13** and **Figure 14**) [76-81].

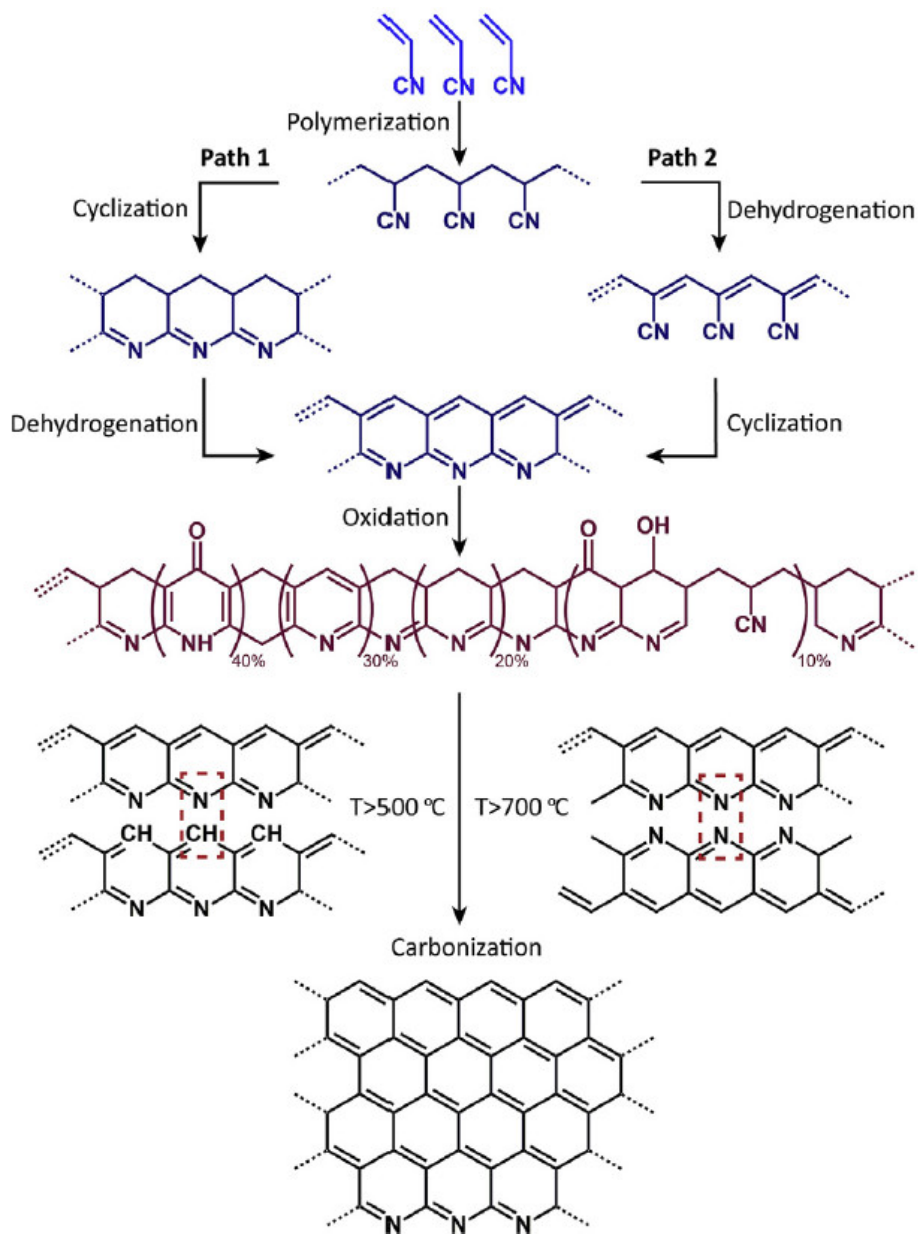


**Figure 11.** Plausible mechanistic pathways for the thermo-oxidative stabilization of PAN, followed by carbonization [62]

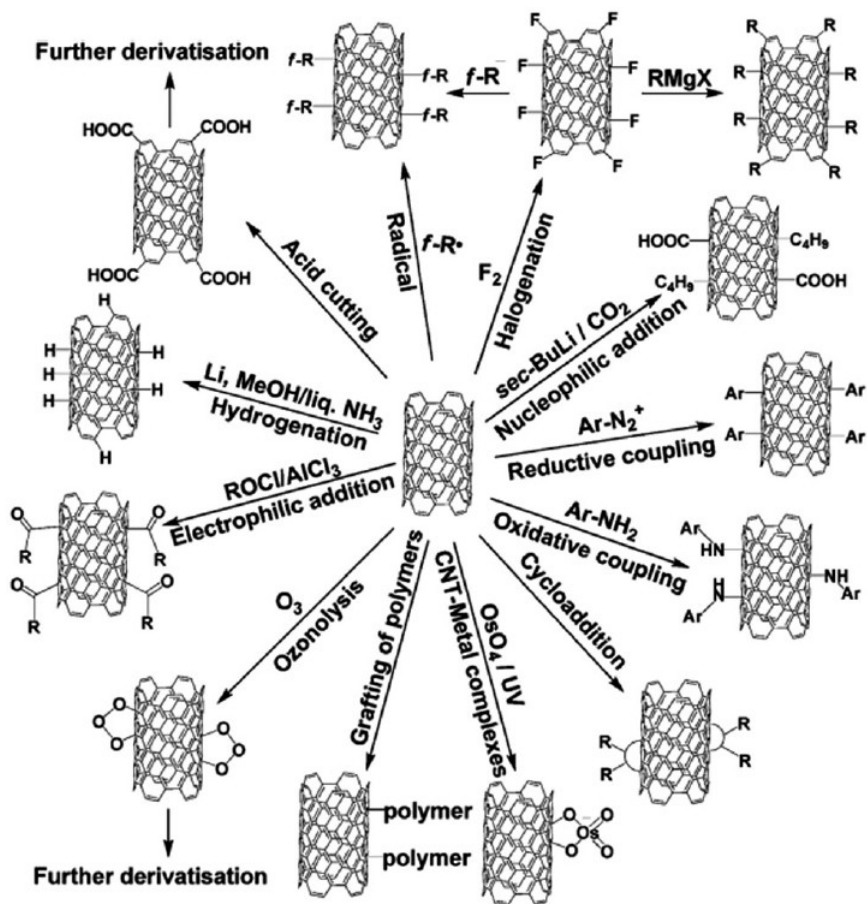


**Figure 12.** Surface functionalization of carbon nanotubes [75]

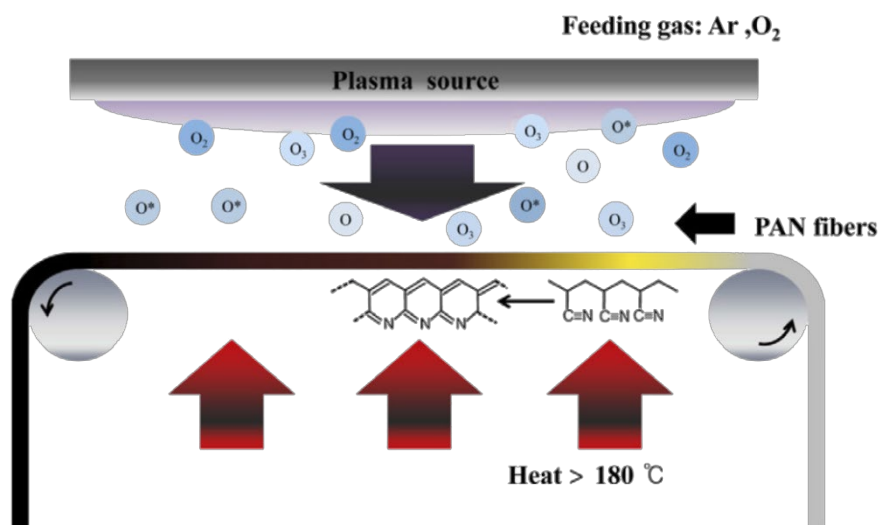


**Figure 13.** Schematic diagram of the plasma system for the stabilization process [80]

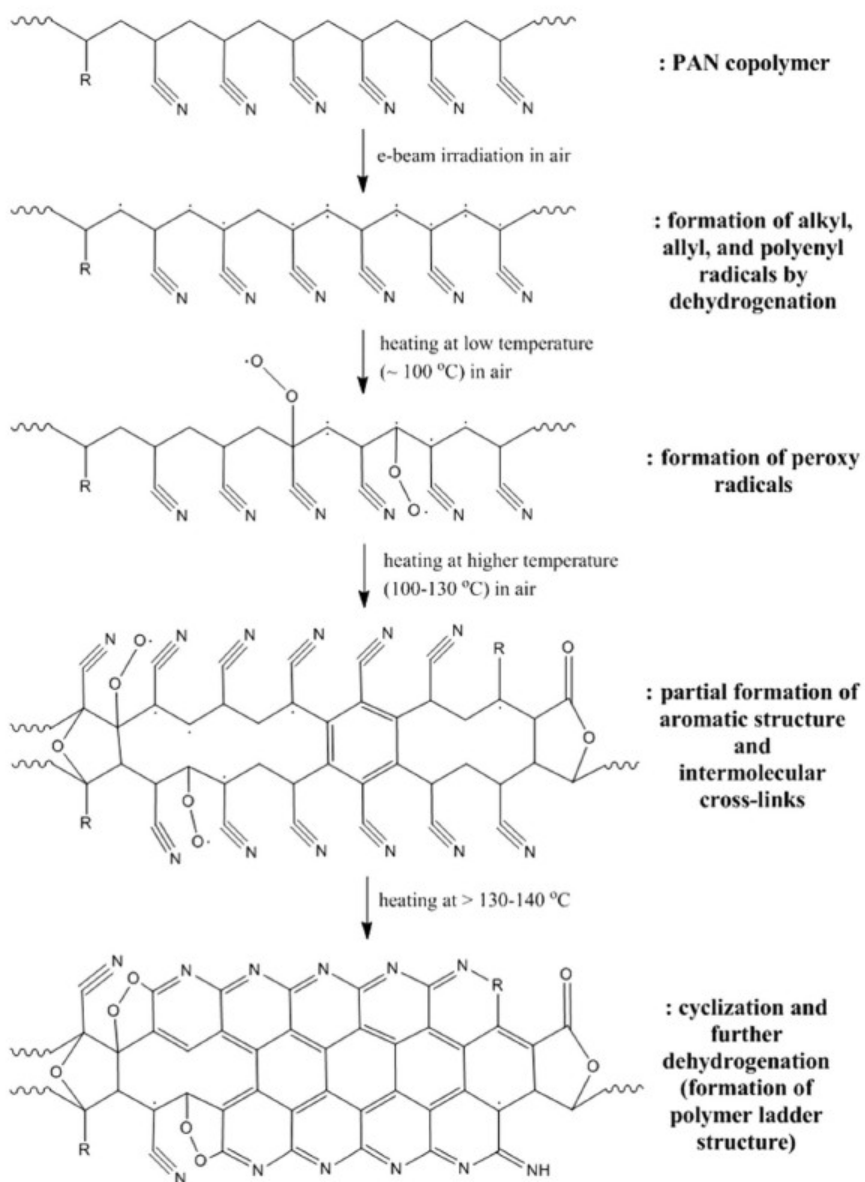


**Figure 14.** The suggested mechanism of thermal stabilization of electron-irradiated PAN fibers [81]

### 1.1.1.2. Hybrid nanomaterial

Metal nanomaterials have revolutionized many applications in nanoscience, including plasmonic, catalysis, sensing, electronics, photonics, information storage, pharmaceuticals, energy conversion, and cosmetics [82, 83]. Their excellent and controllable performance is markedly different from when in bulk form, and the properties such as composition (single metal vs. bimetallic), size (faceting or arrangement of an atom), geometry/shape (surface of atom on surface or arrangement) and structure (hollow vs. solid interior) are closely related to individual or combined physical and chemical properties resulting from nanoscale reduced size.

There are two fundamental strategies used to prepare metal nanomaterials: bottom-up and top-down (**Figure 15**) [84]. The bottom-up approach, including chemical reduction, photochemical reduction, electrochemical reduction, templating, and thermal methods [85-89], is a basic technique to prepare metal nanostructures by reducing their ions to metals, and the growth of the nano-architectures is usually controlled by agents such as surfactants or stabilizers. On the other hand, the top-down approach involves removing materials from the bulk substrate to leave behind the desired nanostructures.

Common top-down methods include photolithography, electron beam lithography, and nanosphere lithography [90, 91].

In the past few years in research and industry, interest in organic-inorganic composite materials has increased due to the improved chemical and mechanical properties through mutual complementary interactions that offset each drawback [92, 93]. Therefore, research has been conducted on the manufacture of composite materials of various combinations and types such as metal/polymer, metal/polymer, metal oxide/carbon. For energy storage devices, high capacity and stability can be achieved simultaneously when a composite material of inorganic material with a large theoretical but poor durability and a stable but small capacity organic material is used. For chemical sensors, a composite material of inorganic material with high sensitivity but high operating temperature and fast response/recovery action but poor stability can be used as a transducer for the sensor to operate more efficiently at room temperature [94-98].

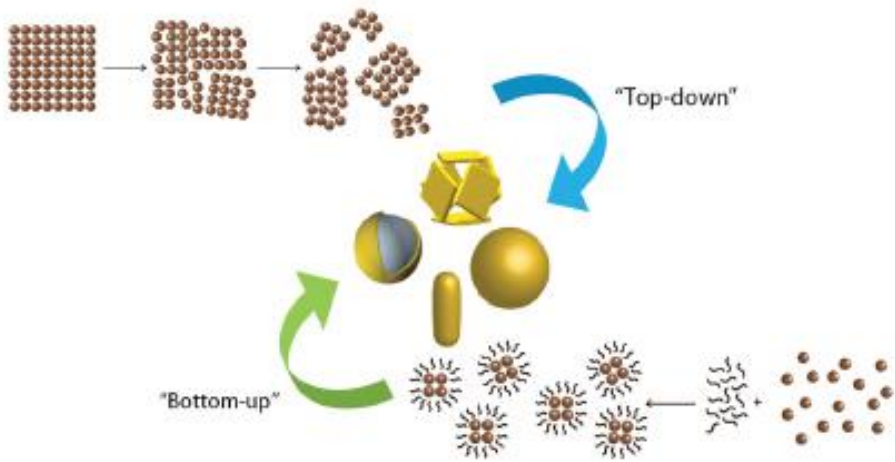


**Figure 15.** Top-down and bottom-up approaches for producing controlled nanomaterials [84]

#### **1.1.1.2.1. Noble metal/carbon nanomaterial**

Noble metal such as gold (Au), platinum (Pt), palladium (Pd), ruthenium (Ru) have been received much attention because of their intrinsic properties that turned up at nanoscale. Among them, catalytic characteristics are applied to various fields such as non-enzyme sensors, automobile exhaust catalysts, oxygen evolution reaction (OER), and oxygen reduction reaction (ORR).

Recently, noble metal/carbon nanomaterial composites are attracting attention because of their unique structure and potential for use as improved sensors or catalysts. There are a variety of methods, such as fixing a precious metal on a polymer surface by interacting with the functional groups of the polymer or applying a current or voltage to the metal ion using chemical reduction. Typically, electrodeposition, ultrasonication, liquid phase reduction using an oxidizing agent, etc. are reported to be widely used [99-103].

#### **1.1.1.2.2. Metal oxide/carbon nanomaterial**

Metal oxides are chemical compounds that consisted of metal, especially cation or transition metal and oxygen. This material is used in diverse applications such as catalysts, supercapacitors, batteries, and sensors due to catalytic properties, high surface area to volume ratio, and porosity. Because of this feature, it showed high performance in devices such as sensors and energy devices, but the redox cycle proceeding during device operation collapses structure which means poor device stability. Also, low conductivity made it difficult to operate a gas sensor at room temperature. To overcome these shortcomings, efforts have been made to increase the surface area of metal oxides or to make composites with other materials. Especially, metal oxide/carbon composite materials are promising alternatives due to high conductivity and considerable mechanical properties of carbon. In addition, it is easy to combine carbon and metal oxide sources, which has the advantage of simultaneously producing carbon and metal oxide. A typical example is the stabilization of a metal hydroxide/polymer composite in the air followed by carbonization at high temperatures [104-110].

### 1.1.2. Sensor application

Sensor application is electronic devices, modules, or subsystems that detect changes or stimuli and turn them into identifiable signals. This device consists of an active sensing material and a signal transducer (**Figure 16**) [111]. They react with the target and transmit the signal without distortion. Various methods such as high-pressure liquid chromatography, gas chromatography coupled with mass spectrometry, and infrared spectroscopy have been used as sensors. However, due to high cost, huge data sampling, expensive, the complexity of sample preparation and measurement, and mental maintenance, the application of these techniques for the real-time sensors is unrealistic. As an alternative, solid-state sensors have been used to detect a variety of targets over the last two decades [112-117].

There are several critical sensor elements for high performance such as sensitivity, selectivity, response/recovery time, working temperature, and stability. To satisfy these various factors, the nanomaterial is a promising candidate for transducer because of its small size, high surface area, and unique electrical properties [118, 119].

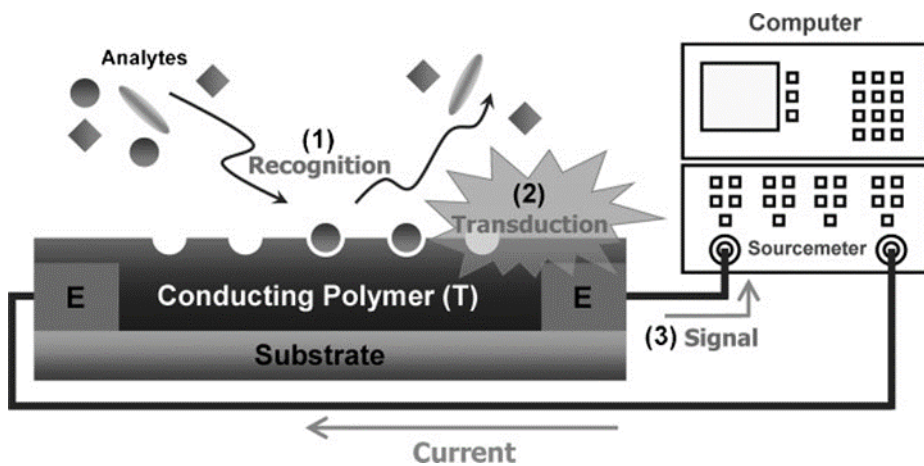


**Figure 16.** Schematic explanation of sensor mechanism [111]

### 1.1.2.1. Liquid-ion-gated FET sensor

Biosensor consists of reaction units such as metal, antibodies, enzymes and aptamers, and transducers to detect bio-target analytes. Measurement of the target analyte mechanism could be explained by converting a signal that arises from an analyte-receptor combination to an electrical signal that could be analyzable (**Figure 17**) [120-124].

Biosensors can be classified by output signal type for instance, electrical, optical, piezoelectric, fluorescent, and so on. Among various biosensors, FET type biosensors have received considerable attention as a desirable candidate due to their current amplification and enhanced signal-to-noise (S/N) ratio (**Figure 18**) [125]. In addition, miniaturization, low operating voltage, and ultra-low minimum detectable concentration (in femto- and pico- level) are also the reason for attention. This type of sensor composed of metal (e.g. gold, silver) electrode, transducer materials (e.g. conducting polymer, carbon) and target selective receptor [126-130].

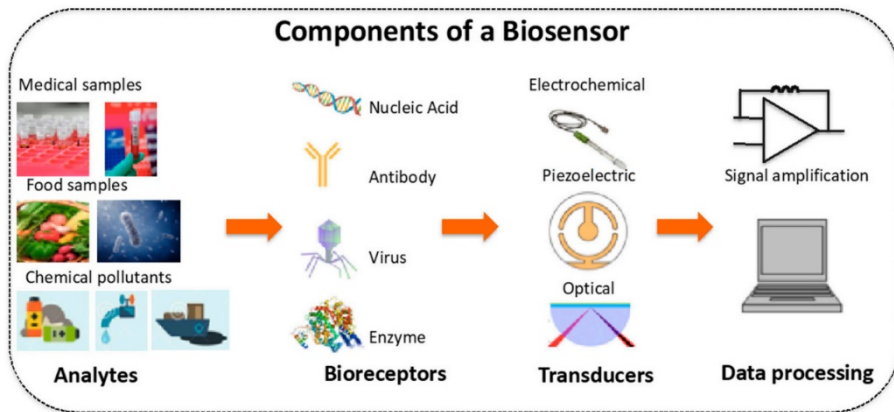


**Figure 17.** Components of a typical biosensor [120]

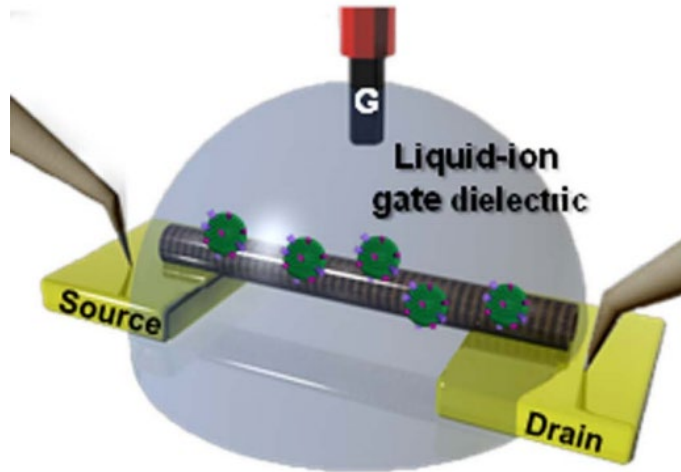


**Figure 18.** Schematic illustration of liquid-ion-gated FET-type sensor

[125]

#### **1.1.2.1.1. Bisphenol-A (BPA) FET sensor**

In recent years, precise sensing platforms for the solution-phase detection of small molecules have become increasingly important for monitoring human diseases, food safety, and environmental contaminants. Bisphenol-A (BPA) is a particularly important xenoestrogen, with a structure similar to that of the hormone estrogen, and is a known endocrine-disrupting compound (EDC) [131-134]. Because of the structural similarity, even low concentrations (ca. 100 pM) of BPA are able to bind estrogen receptors (ERs), thereby inducing adverse changes such as reproductive disorders, chronic diseases, and various types of cancer, via both endocrine pathways [135-139] and genomic pathways [140-144]. Despite such serious effects on human health, the use of BPA still remains widespread for food storage and packaging which is of particular concern as BPA can readily migrate into food at high temperatures, as well as for thermal printing paper, medical materials, and adhesives [145-147]. In addition, since residual trace amounts of BPA is a potential endocrine disruptor, the maximum residue limit (MRL) for BPA in food or food packages was established at 0.6  $\mu\text{g/g}$  by the European Union Legislation, and also the maximum acceptable dose and tolerable daily

intake (TDI) for BPA were established by the European Food Safety Authority (EFSA) [148, 149]. Therefore, monitoring of both dietary and non-dietary exposure to BPA is important for human healthcare.

Several approaches have been reported for detecting BPA at low concentrations [150-154]. High-performance liquid chromatography (HPLC) and gas chromatography coupled with mass spectrometry (GC/MS) are the most widely used methods to detect BPA. However, these techniques require large and expensive equipment that needs labor-intensive processes, and the interpretation of data from these techniques is not always straightforward, as well. Immunoassays, using anti-bodies as biological recognition compounds, are another attractive simple method for screening small toxins such as BPA due to their low-cost aspect and high sensitivity. Nevertheless, in complex matrices including pH, salt concentrations, and other substances, the matrix effect associated with the quality of the antibody can cause non-specific binding to the antibodies with structural analogs, and then bring on the degradation of the detection accuracy towards the antigen.

#### **1.1.2.1.2. Nesfatin-1 (NES1) FET sensor**

Epilepsy is one of the world's health problems and one of the most difficult to diagnose. In the diagnosis of epilepsy, electroencephalogram (EEG) measurements help beyond going through the clinical history of seizure symptoms. However, practical diagnosis is still a difficult task, as EEG with cumbersome instruments is expensive for patients and sometimes even with a definitive diagnosis, which leads to non-pathological consequences [155]. In conclusion, the current epilepsy diagnosis has problems estimating the disease after the onset of seizure symptoms, and the diagnosis also has inaccuracy, costliness, or incidental discomfort. Therefore, a more cost-effective and easily accessible alternative is of great value. By the way, a recent relationship between animal and human hormones and seizures has been reported. Changes in serum hormone levels are associated with temporary deformation during seizures and affect brain function, metabolism, and temporal epilepsy secretion [156]. Although epilepsy diagnosis has been reported in several studies, including serum prolactin (PRL) levels, the sensitivity and specificity of serum PRL analysis for the diagnosis of epilepsy seizure (ES) remain controversial. [157-159].

Nesfatin-1 is involved in a variety of physiological functions including food intake, appetite stimulation, and energy homeostasis, with decreased expression in the hypothalamic ventricle nucleus (PVN) during starvation [160, 161]. In addition, electrophysiological studies have shown that nesfatin-1 stimulates hyperpolarization and depolarization in PVN neurons and arcuate nucleus (ARC) and is a potential candidate marker of increased epilepsy in serum and saliva [162, 163]. Currently, in addition to EEG, increased prolactin levels are used to distinguish epileptic seizures from non-epileptic events [164]. However, in this regard, the use of prolactin has some limitations that should be measured 10-20 minutes after the event and not suitable for use in status epilepsy, repetitive seizures, and neonatal seizure conditions [165]. Nesfatin-1 levels have been reported to increase in patients with epilepsy and may be useful in identifying individuals suffering from epileptic seizures [166].

### **1.1.2.1.3. Dopamine (DA) FET sensor**

Neurotransmitters (NTs) are chemical messengers through secretion from one neuron to the next until binding onto specific receptors located on the membranes of the target cell [167, 168]. Among various NTs, dopamine (DA) has been widely studied since the 1950s due to its important role in the functions of the central nervous system, renal, hormonal, and cardiovascular system [169, 170]. Especially, the abnormal level of DA is believed to be associated with certain neurological disorders known as sleeping and eating disorders, Parkinson's disease, and addictive behaviors associated with drug abuse [171, 172]. However, the clinical concentration of DA is very low; for example, the DA levels in plasma, urine, and single adrenal chromaffin cell are in the range of nM ( $10^{-9}$  M),  $\mu$ M ( $10^{-6}$  M), and fM ( $10^{-15}$  M), respectively [173, 174]. Therefore, the rapid and sensitive detection of DA in a biological system is important for the routine analysis and diagnosis of neurological disorders. Several analytical methods have been conducted for detection DA at low concentrations [175, 176]. Among them, enzymatic-assay-based methods have attracted considerable attention due to their high sensitivity for DA and comparable low cost [177, 178]. However, these techniques are

not used as frequently owing to accurate DA detection depends strongly on the quality of the prepared enzyme and non-specific binding to analytes having a similar structure. In this regard, the electrochemical sensing technique based on field-effect-transistors (FETs) for dopamine detection is an attractive method due to low cost, easy operation, fast response, high sensitivity, and feasibility of miniaturization.

### 1.1.2.2. Chemiresistive sensor

With the recent development of the industry, research on chemical gas sensors has been increasing along with interest in public safety and environmental pollution. The detection technology for toxic or dangerous chemical gases and specific disease factors, chemical gases, is becoming increasingly important not only in biochemical terrorism, but also in industrial fields, environmental pollution, and medical health. Among various gas sensors, it is highly desirable to measure resistance change due to simple operation, low production cost, miniaturization, and relatively high sensitivity (**Figure 19**) [179].

Typical gas sensors include active materials that are sensitive to the target and gas. When the active layer reacts with target molecules, resistance change occurred. This change in resistance is due to changes in the electrical properties of the active layer during the reaction, and the electron-withdrawing or electron-donating action with the target produces a change in resistance depending on what is the main charge carrier of the active layer [180, 181]. For example, in **Figure 20**, the gas molecule interacts with the sensing material to change some of its physical properties such as conductivity(s), work function ( $\phi$ ) and permittivity ( $\epsilon$ ). The transducer converts one of these

physical quantities into a change in electrical parameters such as capacitance C, inductance L and resistance R. Finally, the circuit to which the sensor is connected generates a sensed electrical signal that becomes a current (I) or voltage (V) and can measure each magnitude, frequency (F) and phase ( $\phi$ ) [182].

Traditionally, a metal oxide semiconductor has been widely used as an active layer for resistive chemical sensors with a wide range of detecting molecules such as hydrogen sulfide ( $\text{H}_2\text{S}$ ), hydrogen gas ( $\text{H}_2$ ), ammonia ( $\text{NH}_3$ ), nitrogen dioxide ( $\text{NO}_2$ ) and ethanol. However, there is a disadvantage that requires a high operating temperature. To overcome this problem, research has been conducted for fabricating organic/metal oxide composite that is widely studied [183, 184].

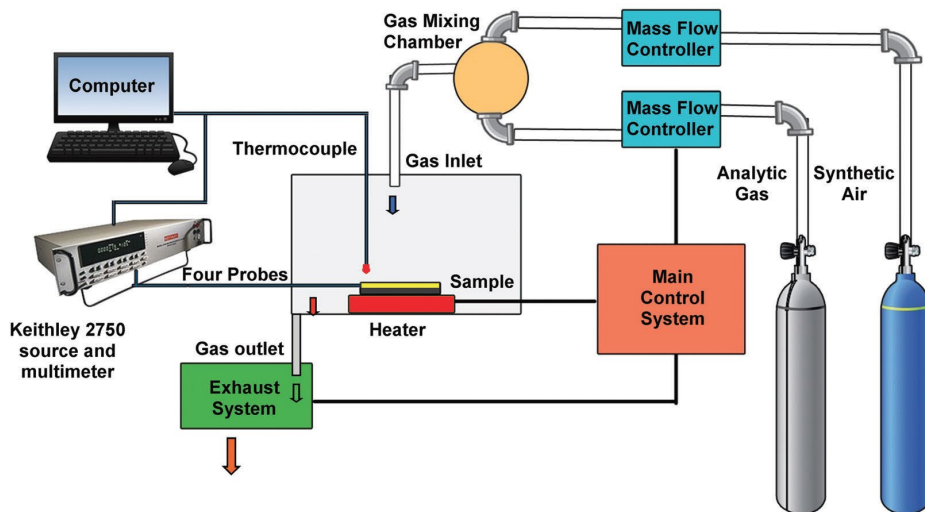


**Figure 19.** Schematic diagram of the resistive-type gas sensor setup

[179]

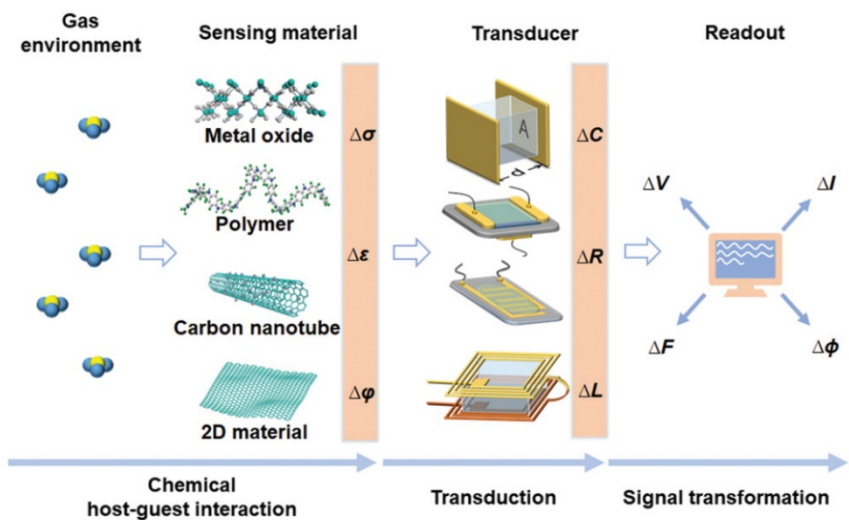


**Figure 20.** Schematic illustration of the electrical gas sensing process

[182]

#### **1.1.2.2.1. Hydrogen sulfide (H<sub>2</sub>S) sensor**

Due to recent environmental concerns and the need to control hazardous chemicals in the industry, interest in developing sensor systems for various toxic gases has increased [185, 186]. Hydrogen sulfide (H<sub>2</sub>S), derived from microbial decomposition of plants and animals, is one of the most abundant toxic gases found as a cause of bad breath in our bodies as well as in the coal mine, manhole and semiconductor device industries [187, 188]. H<sub>2</sub>S is broadly hazardous in the human body causing the collapse of the nervous system and disturbance of cellular respiration due to binding iron in the mitochondrial cytochrome enzymes [189, 190], and according to the Occupational Safety and Health Administration (OSHA), the threshold limit value (TLV) and recommended acceptable ambient levels of H<sub>2</sub>S are 10 ppm for 8 h and lower than 0.1 ppm, respectively [191]. Therefore, detecting H<sub>2</sub>S sensitively (<10 ppm) and selectively is an important issue emerging in environmental surveillance, disease diagnosis, and food safety. However, conventional H<sub>2</sub>S gas sensors have some limitations, such as slow response/recovery time and high operating temperature, which cause complex sensing platforms and are difficult to deploy in restricted areas.

### **1.1.2.3. Wireless sensor**

A wireless sensor is a device in which sensing electronic transducers are spatially and galvanically separated from their associated readout/display components. Compared to the traditional tethered sensor, the wireless sensor includes the non-obtrusive nature of its installation, higher nodal density, and lower installation cost without the need for extensive wiring [192, 193]. These attractive features of wireless sensors facilitate its development toward measurements in a wide range of physical, chemical, and biological parameters of interest. Examples of currently available wireless sensors include devices for sensing of pH, pressure, and temperature in medical, pharmaceutical, animal health, livestock condition, automotive, and other applications [194, 195]. Unfortunately, although there are numerous practical applications, the available wireless gas sensors fall short of meeting emerging measurement needs in complex environments. Especially, existing wireless gas sensors cannot perform highly selective gas detection in the presence of high levels of interferences and cannot quantitate several components in gas mixtures.

### 1.1.2.3.1. RFID wireless sensor

The wireless gas sensors are based on different detection principles depending on the type of sensing materials and associated transducers used to provide the required sensitivity, selectivity, and stability of measurements [196, 197]. In particular, the power requirements for different gas sensing transducers and sensing systems can be applied for wireless sensing, and there are two types of wireless sensors, active and passive, depending on the available power for operation.

A radio frequency identification (RFID) sensor is a field that is expected to have a commercial effect with several advantages such as inexpensive, effective, invisible installation, and having a long-range coverage, but there are still difficulties in introducing sensor transducer materials. Several representative examples of active and passive RFID sensors are presented in **Figure 21** [198]. The limiting form factor for active RFID sensors (**Figure 21a and b**) is the size of their power source. The limiting form factor for passive RFID sensors is the antenna size (**Figure 21c-f**). Typical operating frequencies of RFID devices are 125 - 135 kHz (LF, low-frequency tags), 13.56 MHz (HF, high-frequency tags), 868 - 956 MHz (UHF, ultrahigh-frequency tags), and 2.45 GHz (microwave tags).

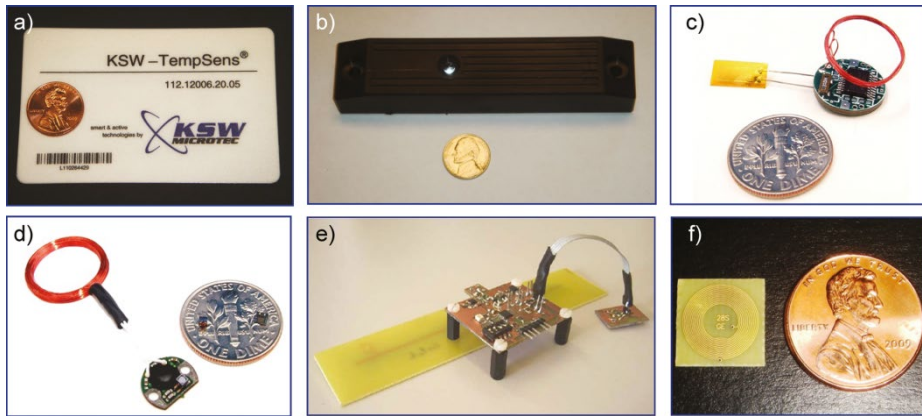


**Figure 21.** Examples of active and passive RFID sensors. Active sensors with (a) thin-film and (b) AAA-type batteries. Passive sensors with an analog input into an IC memory chip for operation at (c) LF, (d) HF, and (e) UHF frequency ranges; (f) passive sensor based on a common HF RFID tag with a sensing material applied directly to the resonant antenna of the sensor [198].

## **1.2. Objectives and Outlines**

### **1.2.1. Objectives**

The aim of this dissertation is for providing novel methods to fabricate electrospun polyacrylonitrile (PAN)-based various metal nanoparticles-embedded-multichannel carbon nanofibers for bio and chemical sensor applications. In detail, firstly it was confirmed that multichannel carbon nanofiber has utility as a sensor transducer through the biosensor applications. Then the metal nanoparticles-embedded multichannel carbon nanofibers were produced by electrospinning precursor-mixed blend polymer followed by plasma treatment before carbonization. The as-fabricated nanomaterials were applied as a biosensor and wireless chemical sensor. Different kinds of materials such as bio-receptors (aptamer, antibody), ruthenium (Ru) nanoparticles, iron oxide ( $\text{Fe}_2\text{O}_3$ ) nanoparticles were introduced. Through the facile synthesis method in each experimental condition, the hybrid nanomaterials could be obtained with unique and enhanced properties and applied to several bio/chemical sensor applications, such as endocrine-disruptor (bisphenol-A), epileptic salivary biomarker (nesfatin-1), neurotransmitter (dopamine), toxic gas (hydrogen sulfide), respectively.

### 1.2.2. Outlines

The doctoral dissertation involves the following subtopics:

- I. Bio-receptors-modified multichannel carbon nanofibers for liquid-ion-gated FET sensor detecting bisphenol-A and nesfatin-1
  - I-1. Fabrication of multichannel carbon nanofibers
  - I-2. Application for endocrine-disruptor sensor
  - I-3. Application for epileptic salivary biomarker sensor
  
- II. Ruthenium nanoparticles-embedded multichannel carbon nanofibers for liquid-ion-gated non-enzymatic FET sensor detecting dopamine
  - II-1. Fabrication of ruthenium nanoparticles-embedded multichannel carbon nanofibers
  - II-2. Application for neurotransmitter sensor
  
- III. Iron oxide nanoparticles-embedded multichannel carbon nanofibers for wireless chemical sensor detecting hydrogen sulfide

III-1. Fabrication of iron oxide nanoparticles-embedded multi-channel carbon nanofibers

III-2. Application for toxic gas wireless gas sensor

Each subtopic contains experimental details, characterization of fabricated material, and real-time sensing performance.

## 2. Experimental Details

### 2.1. Bio-receptors-modified multichannel carbon nanofibers for liquid-ion-gated FET sensor detecting bisphenol-A and nesfatin-1

#### 2.1.1. Fabrication of bio-receptors-modified MCNFs FET sensor (anti-BPA aptamer & anti-NES1 antibody)

All chemicals were used as received without any further purification. Poly(acrylonitrile) (PAN), with a molecular weight of  $M_w = 150\ 000$ , and poly(methyl methacrylate) (PMMA), with a molecular weight of  $M_w = 350\ 000$ , were purchased from Sigma-Aldrich. N,N-dimethylformamide (DMF) (Sigma-Aldrich) was used as the solvent for both the PAN and PMMA solutions. Bisphenol-A (BPA) (i.e., 4,4'-(propane-2,2-diyl)diphenol), as well as the BPA structural analogs 4,4'-(butane-2,2-diyl) diphenol (bisphenol-B, BPB), 4,4-bis(4-hydroxyphenyl) valeric acid (VA), 4,4'-dihydroxybiphenyl (4,4'-biphenol, BP) and 4,4'-(hexafluoro-isopropylidene) diphenol (6F) were purchased from TCI. The BPA-binding aptamer was synthesized by Bioneer Co. (Daejeon, Korea). The sequence of the aptamer was 5'-NH<sub>2</sub>-(CH<sub>2</sub>)<sub>6</sub>-CCG GTG GGT GGT CAG GTG GGA TAG CGT TCC GCG TAT GGC CCA GCG CAT CAC GGG TTC GCA CCA-3',

where A, T, G, and C represent adenine, thymine, guanine, and cytosine, respectively. The aptamer stock solution was diluted with diethylpyrocarbonate (DEPC) and water, stored in a freezer at  $-20\text{ }^{\circ}\text{C}$  prior to using. To prepare the actual BPA samples, a polycarbonate (PC) bottle and thermal printing paper were prepared to extract BPA. The PC bottle filled with distilled water was sonicated and was then immersed in an oil bath at  $70\text{ }^{\circ}\text{C}$  for 1 h. After filtration, the liquid was collected. The thermal printing paper (10 mg) was immersed in 10 ml absolute ethanol at  $70\text{ }^{\circ}\text{C}$  for 1 h. After filtration, extracts were diluted 1:1,000 in distilled water. Nesfatin-1 (NES1) and anti-NES1 antibody were purchased from LSBio. Recombinant hepatitis B virus surface antigen protein was purchased from Abcam. Commercial artificial saliva for xerostomia was used as an artificial saliva solution sample.

PAN/PMMA-based multichannel carbon nanofiber (MCNF) were fabricated by electrospinning and subsequent heat treatment. PAN solution was prepared by dissolving 1.0 g of PAN in 10 mL of DMF at  $60\text{ }^{\circ}\text{C}$  followed by vigorous stirring for 2 h. PMMA solution was prepared in the same manner as the PAN solution. These polymer solutions were mixed in a 1:1 ratio and stirred vigorously for 3 h. Another 12 wt% PAN solution for fabricating CNF was prepared in

the same manner of stirring. The resulting mixture and 12 wt% PAN solution each were electrospun using a single-0.1-mm-diameter syringe nozzle with an applied voltage of 18 kV and a flow rate of 10  $\mu\text{L min}^{-1}$  (**Figure 22**). The distance from the tip to the collector was fixed at 15 cm. The electrospun NFs were calcined at 400 °C for 2 h in air and then carbonized in flowing argon at 800 °C for 1 h.

Carboxyl-functionalized MCNF (cMCNF) was prepared *via* an oxidative treatment. MCNF (250 mg) was added to 20 mL of a 3:1 volume mixture of 1 M sulfuric acid ( $\text{H}_2\text{SO}_4$ ) and 1 M nitric acid ( $\text{HNO}_3$ ) for a systematically varied time and diluted with distilled water. The mixed MCNF solution was purified by repeated centrifugation and multiple washing steps. The resulting cMCNF solution was evaporated at 60 °C. Carboxyl-functionalized CNF (cCNF) was prepared in the same manner as cMCNF.

To form bio-receptors-modified MCNFs FET-type biosensor, interdigitated array (IDA) electrodes (**Figure 23**) were treated with 5 wt% aqueous amino silane (i.e., 3-aminopropyltrimethoxysilane, APS) for 6 h to form amino groups on the electrode. The electrodes were then exposed to 40  $\mu\text{L}$  of a mixture of 0.1 wt% aqueous cMCNFs solution and 40  $\mu\text{L}$  of 1 wt% aqueous 4-(4,6-dimethoxy-1,3,5-triazin-2-yl)-4-

methylmorpholinium chloride (DMT-MM) for 12 h. The resulting electrodes, with immobilized cMCNFs, were rinsed with distilled water to remove extra residues including DMT-MM and unbound cMCNFs. Likewise, cCNF was immobilized in the same way as cMCNF. Depending on different binding receptors, anti-BPA aptamer-modified MCNF (A-MCNF) and anti-NES1 antibody-modified MCNF (Ab-MCNF) consists of FET-type sensor immobilized on IDA electrodes. To attach the BPA-binding aptamer and NES1-binding antibody to the cMCNF surface, a coupling reaction was then carried out using a mixture of the binding receptor and 1 wt% aqueous DMT-MM (40  $\mu$ L) for 12 h. The A-MCNF immobilized electrodes and the Ab-MCNF immobilized electrodes were then rinsed with distilled water repeatedly and dried at room temperature. The anti-NES1 antibody-modified CNF (Ab-CNF) immobilized electrodes were prepared in the same way.

### **2.1.2. Characterization**

Field-emission scanning electron microscopy (FE-SEM) images were obtained using a JEOL-6700 (JEOL) (JEOL Ltd., Tokyo, Japan) installed at Chemical & Biological Engineering Research Facilities (CBERF) at Seoul National University. Transmission electron microscopy (TEM) images were obtained using a JEM-2100 installed at the National Center for Inter-university Research Facilities (NCIRF) at Seoul National University. The nitrogen adsorption–desorption isotherms were analyzed using an ASAP 2010 (Micrometrics) equipment. In detail, pore size distribution and surface area were measured by Brunauer–Emmett–Teller (BET) and Barrett–Joyner–Halenda (BJH) methods. FTIR spectra were collected with Spotlight 200i Frontier (PerkinElmer) spectrophotometer in attenuated total reflection (ATR) mode. XPS spectra were recorded on an Axis-His system (KRATOS).

### 2.1.3. Electrical measurement

All electrical measurements were carried out using a Keithley 2612A source meter and a probe station (MS TECH, model 4000). A 300  $\mu\text{L}$  chamber was used for solution-based measurements. The measured current was normalized as follows:

$$\left[ \frac{\Delta I}{I_0} \right]_{SD} (\%) = \frac{(I - I_0)}{I_0} \times 100$$

, where  $I_0$  is the initial measured current, and  $I$  is the time-varying measured current.

The A-MCNFs FET sensors were carried out the following recycling process: (i) immobilizing BPA-binding aptamers on IDA electrodes as mentioned above, (ii) injecting BPA molecule into the A-MCNFs FET sensor, (iii) washing with 10 % sodium chloride solution and air-drying.

## **2.2. Ruthenium nanoparticles-embedded multichannel carbon nanofibers for liquid-ion-gated non-enzymatic FET sensor detecting dopamine**

### **2.2.1. Fabrication of Ru-mCNFs non-enzymatic FET sensor**

All chemicals were used as received without any further purification. Poly(acrylonitrile) (PAN) (M<sub>w</sub> = 150 000), polystyrene (PS) (M<sub>w</sub> = 192 000), and ruthenium (III) chloride hydrate (99.98%) were purchased from Sigma-Aldrich. N,N-dimethylformamide (DMF) (Sigma-Aldrich) was used as the solvent for both the PAN and PS solutions. Dopamine (DA), epinephrine (EP), norepinephrine (NE), phenethylamine (PEA), tyrosine (TR), ascorbic acid (AA), uric acid (UA) were purchased from Sigma-Aldrich.

PAN/PS-based multichannel carbon nanofiber (mCNF) and ruthenium nanoparticles-embedded mCNF (Ru-mCNF) were fabricated by electrospinning and subsequent heat treatment. PAN solution was prepared by dissolving 0.75 g of PAN in 4.25 mL of DMF at 60 °C followed by vigorous stirring for 2 h. PS solution was prepared in the same manner as the PAN solution. A controlled amount of ruthenium (III) chloride hydrate was added to the PS solution before vigorous stirring. These polymer solutions were mixed

in a 1:1 ratio and stirred vigorously for 3 h. The resulting viscous mixture was electrospun using a single-0.1-mm-diameter syringe nozzle with an applied voltage of 18 kV and a flow rate of  $10 \mu\text{L min}^{-1}$  (**Figure 22**). The distance from the tip to the collector was fixed at 15 cm. The collected electrospun NFs were treated by atmospheric-pressure Ar/O<sub>2</sub> plasma (180 W, 0.02/0.008 L/h) for 5 min, following calcined at 270 °C for 1 h in air and then carbonized 1 h in flowing argon at 800 °C for.

To construct Ru-mCNFs-immobilized non-enzymatic FET-type sensor, inter-digitated array (IDA) electrodes (**Figure 23**) were treated with 5 wt% aqueous amino silane (i.e., 3-aminopropyltrimethoxysilane, APS) for 6 h to form amino groups on the electrode. The electrodes were then exposed to 40  $\mu\text{L}$  of a mixture of 0.1 wt% aqueous Ru-mCNFs solution and 40  $\mu\text{L}$  1 of wt% aqueous 4-(4,6-dimethoxy-1,3,5-triazin-2-yl)-4-methylmorpholinium chloride (DMT-MM) for 12 h. The resulting electrodes, with immobilized Ru-mCNFs, were rinsed with distilled water to remove extra residues including DMT-MM and unbound Ru-mCNFs.

### 2.2.2. Characterization

Field-emission scanning electron microscopy (FE-SEM) images were obtained using a JEOL-6700 (JEOL) (JEOL Ltd., Tokyo, Japan) installed at Chemical & Biological Engineering Research Facilities (CBERF). Transmission electron microscopy (TEM) images were obtained using a JEM-2100 installed at the National Center for Inter-university Research Facilities (NCIRF) at Seoul National University. High-resolution transmission electron microscopy (HR-TEM) images and electron energy loss spectroscopy (EELS) mapping images were obtained from a JEM-2100F installed at the Research Institute of Advanced Materials (RIAM) at Seoul National University. FTIR spectra were collected with Spotlight 200i Frontier (PerkinElmer) spectrophotometer in attenuated total reflection (ATR) mode. X-ray diffraction (XRD) measurements were performed on a SmartLab X-ray Diffractometer (Rigaku) using Cu K $\alpha$  radiation ( $\lambda = 1.5406 \text{ \AA}$ ) at 40 kV and 300 mA (12 W). Raman spectra were recorded with LabRam Aramis (Horiba Jobin Yvon) spectrometer. X-ray photoelectron spectroscopy (XPS) spectra were recorded using M16XHF-SRA (Mac Science Co., Yokohama, Japan).

### 2.2.3. Electrical measurement

All electrical measurements were carried out using a Keithley 2612A source meter and a probe station (MS TECH, model 4000). A 300  $\mu\text{L}$  chamber was used for solution-based measurements. The measured current was normalized as follows:

$$\left[ \frac{\Delta I}{I_0} \right]_{SD} (\%) = \frac{(I - I_0)}{I_0} \times 100$$

, where  $I_0$  is the initial measured current, and  $I$  is the time-varying measured current.

## **2.3. Iron oxide nanoparticles-embedded multichannel carbon nanofibers for wireless chemical sensor detecting hydrogen sulfide**

### **2.3.1. Fabrication of Fe-mCNF**

All chemicals were used as received without any further purification. Poly(acrylonitrile) (PAN) ( $M_w = 150\,000$ ), polystyrene (PS) ( $M_w = 192\,000$ ), and iron chloride (97%) were purchased from Sigma-Aldrich. N,N-dimethylformamide (DMF) (Sigma-Aldrich) was used as the solvent for both the PAN and PS solutions.

PAN/PS-based multichannel carbon nanofiber (mCNF) and iron oxide nanoparticles-embedded mCNF (Fe-mCNF) were fabricated by electrospinning and heat treatment. PAN solution was prepared by dissolving 0.75 g of PAN in 4.25 mL of DMF at 60 °C followed by vigorous stirring for 2 h. PS solution with iron oxide precursor was prepared in the same manner as the PAN solution, adding a controlled amount of iron chloride. These polymer solutions were mixed in a 1:1 ratio and stirred vigorously for 3 h. The resulting viscous mixture was electrospun using a single-0.1-mm-diameter syringe nozzle with an applied voltage of 18 kV and a flow rate of 10  $\mu\text{L min}^{-1}$  (**Figure 22**). The distance from the tip to the collector was fixed at 15 cm. The collected electrospun NFs were treated by atmospheric-pressure Ar/O<sub>2</sub>

plasma (180 W, 0.02/0.008 L/h) for 5 min, following stabilized at 250 °C for 1 h in air and then carbonized at 600 °C for 1 h in flowing argon.

### **2.3.2. Characterization**

Transmission electron microscopy (TEM) images were obtained using a JEM-2100 (JEOL) (JEOL Ltd., Tokyo, Japan) installed at the National Center for Inter-university Research Facilities (NCIRF) at Seoul National University. High-resolution transmission electron microscopy (HR-TEM) images and electron energy loss spectroscopy (EELS) mapping and energy dispersive spectroscopy (EDS) line mapping images were obtained from a JEM-2100F (JEOL) installed at the Research Institute of Advanced Materials (RIAM) at Seoul National University. X-ray diffraction (XRD) measurements were performed on a SmartLab X-ray Diffractometer (Rigaku) using Cu K $\alpha$  radiation ( $\lambda = 1.5406 \text{ \AA}$ ) at 40 kV and 300 mA (12 W). Raman spectra were recorded with LabRam Aramis (Horiba Jobin Yvon) spectrometer. X-ray photoelectron spectroscopy (XPS) spectra were recorded using M16XHF-SRA (Mac Science Co., Yokohama, Japan).

### 2.3.3. Electrical measurement

The electrical measurement of the Fe-mCNF was examined using an interdigitated micro array (IDA) (**Figure 23**). Fe-mCNF (0.5 wt% in ethanol solution) was prepared by sonication for deposition onto the IDA electrode, and a spin-coating method (1000 rpm, 60 s) was used for introducing the uniformly controlled array. Then, the Fe-mCNF IDA electrode was placed in a vacuum chamber for gas sensing. Various gas concentrations were controlled by a mass controlled (MFC) (KNH Instruments, Korea) system. The real-time resistance monitoring was conducted at a constant applied current of  $10^{-6}$  A and the resistance change was defined as follows:

$$S = \frac{\Delta R}{R_0} = \frac{(R - R_0)}{R_0}$$

, where R and  $R_0$  are the real-time resistance and initial resistance, respectively. After detecting  $H_2S$  gas for several minutes, a compressed inert gas was introduced to remove the  $H_2S$  molecules on the Fe-mCNF.

#### **2.3.4. Fabrication of Fe-mCNFs UHF-RFID wireless sensor**

The Fe-mCNF-based conductive paste was prepared by mixing the Fe-mCNF (80 wt%), super-P (10 wt%), and PVDF binder (10 wt%) in an *N*-methyl-2-pyrrolidone solvent. To fabricate the RFID sensor tag, one component of the RFID-based wireless sensor system, the passive UHF-RFID tag (nominal frequency: *ca.* 904 MHz (EMPO Corp.)) was generated 4 mm of the hole in the antenna pattern and covered with plastic tape, with the exception of a 3x6 mm<sup>2</sup> area. The Fe-mCNF-based conductive paste was screen printed onto the exposed antenna pattern area. The RFID reader apparatus, the other part of the wireless sensor system, was constructed from the RFID reader antenna (activated at 865 - 956 MHz) and a network analyzer (E5071B, Agilent Technologies).

### **2.3.5. Wireless sensor measurement**

The wireless sensor tag was placed in a vacuum chamber for gas sensing by the MFC (KNH instruments). A sensing response corresponded to backscattering effects between the sensor tag and signal receiver (RFID reader antenna connected network analyzer). The network analyzer scanned the frequencies over the range of interest and collected the complex impedance response from the sensor tag. The RFID reader antenna was positioned at different distances from the sensor tag, and each sensor tag was read individually. The collected complex impedance data was analyzed using Kaleida Graph (Synergy Software, Reading, PA) and PLS\_Toolbox (Eigenvector Research Co.) operated with Matlab (The Mathworks Inc.).

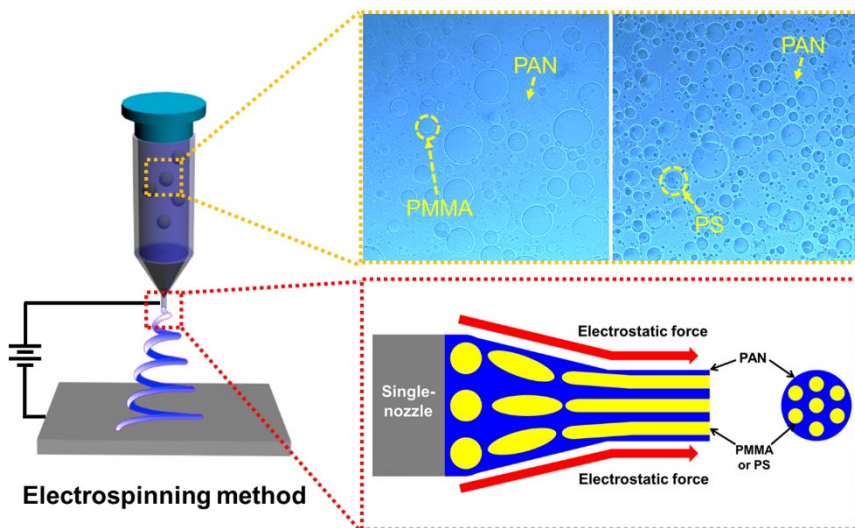


**Figure 22.** Schematic diagram of the single-nozzle co-electrospinning method. The upper insets show optical micrographs of the PAN/PMMA and PAN/PS phase-separated blend. The lower inset is a schematic diagram of multicore polymer nanofiber generation during electrospinning.

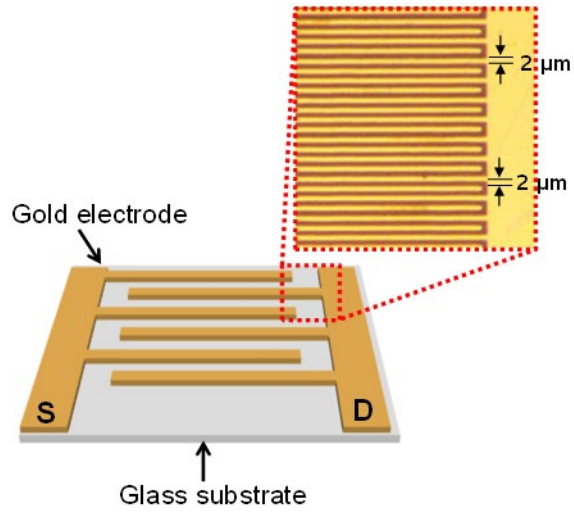


**Figure 23.** Schematic illustration and (inset) optical micrograph of the interdigitated micro array (IDA) on the glass substrate

## 3. Results and Discussion

### 3.1. Bio-receptors-modified multichannel carbon nanofibers for liquid-ion-gated FET sensor detecting bisphenol-A and nesfatin-1

#### 3.1.1. Fabrication of carboxyl-functionalized MCNFs (cMCNFs)

**Figure 24** illustrates an overview of the fabrication process of carboxyl-functionalized multichannel carbon nanofibers (cMCNFs) *via* single-nozzle co-electrospinning and oxidative treatment. First, a 1:1 (by volume) solution of poly(acrylonitrile) (PAN) and poly(methyl methacrylate) (PMMA) was prepared, which resulted in a phase-separated polymer blend because of the interfacial tension, viscosity, and elasticity of the polymers (see inset of **Figure 22**). In this phase-separated blend, the high surface tension of the PMMA resulted in the formation of discontinuous droplets, whereas the more viscous PAN occupied the continuous phase of the solution. During co-electrospinning of this mixed solution, the discrete PMMA droplets elongated along the inside of the PAN shell due to the stretching force of the applied voltage, leading to the formation of multi-core nanofibers (**Figure 22** and **Figure 25a**). These multi-core nanofibers were uniform with a diameter of *ca.* 300 nm. The phase-separated

polymer nanofibers were then stabilized at 400 °C for 2 h and carbonized at 800 °C for 1 h in a flowing argon atmosphere. Multichannel carbon nanofibers (MCNFs) were formed during this heat treatment step. The continuous PAN phase (shell) was transformed into carbon while the inner elongated PMMA phase (cores) decomposed, resulting in the formation of internal multichannel (**Figure 25b**). Owing to the elimination of PMMA from within the fibers, the multi-core nanofibers constricted over the heating process. Eventually, the diameter of the resulting MCNF was *ca.* 150 nm with *ca.* 20 nm-diameter internal channels. In contrast, the prepared PAN nanofiber and carbon nanofiber (CNF) exhibit diameters similar to the multicore nanofiber and MCNF without phase-separation and inner channel structure (**Figure 25d** and **Figure 25e**). The following oxidation procedure was carried out to functionalize the surface of the MCNFs. The MCNFs were treated with a mixture of 1 M sulfuric acid and 1 M nitric acid (3:1 volume ratio) at room temperature, where the reaction time was systematically controlled, and the resulting MCNF was washed with distilled water and dried at 60 °C. As a result, cMCNF was well-fabricated, exhibiting well-defined structures without the collapse of the channels,

as suggested in **Figure 25c**. The resulting cCNF also exhibited an intact structure (**Figure 25f**). In addition, due to the control of oxidation time, the quantity of the carboxyl-functional groups was optimized. If the oxidation time is longer than 12 h, there were overall morphology changes that the multichannel structure of the MCNFs was collapsed and the outer shells of the fibers were combined with each other (**Figure 26**).

Fourier-transform infrared (FTIR) spectra of the cMCNFs are presented in **Figure 27**. Functionalization of the surface of the MCNFs is evidenced by peaks associated with oxygen, including the C=O stretching peak at  $1720\text{ cm}^{-1}$ , the stretching vibration and deformation peaks of -OH groups at  $3430\text{ cm}^{-1}$  and  $1400\text{ cm}^{-1}$ , and the stretching vibration peaks of C-O bonds (including those in phenol groups) at  $1080$  and  $1230\text{ cm}^{-1}$ . The peak at  $1590\text{ cm}^{-1}$  corresponds to structural lattice vibrations of the carbon nanofibers and indicates that the structure of the cMCNFs remained intact after acid treatment. The increase in the intensity of the characteristic peaks at  $1230$ ,  $1720$ , and  $3430\text{ cm}^{-1}$  suggests that carboxyl groups were properly formed on the surface of the MCNFs as the acid treatment time.

The chemical composition of these cMCNFs was also investigated by X-ray photoelectron spectroscopy (XPS). **Figure 28** displays high-resolution XPS spectra for the C (1s) region around 284.5 eV; these peaks were deconvolved into component peaks that the C=C and C–C (284.3 eV) in the aromatic rings, C–O (286.0 eV) in the epoxy and hydroxyl groups, and C=O (288.0 eV) derived from carbonyl and carboxyl groups. An increase in peak intensity associated with carboxyl groups was observed by comparing the intensity of peaks referring to oxygen-related functional groups. This demonstrated that the intensity ratios  $I_{C-O}$  and  $I_{C=O}$  increased gradually as oxidation time increased, according to an increase in the quantity of oxygen in the cMCNFs. These spectral investigations indicate that carboxyl groups were well functionalized on the MCNFs through oxidative treatment.

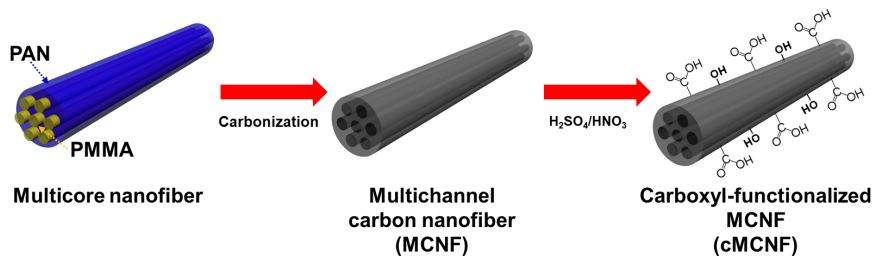


**Figure 24.** Schematic diagram of the carboxyl-functionalized multichannel carbon nanofiber (cMCNF)

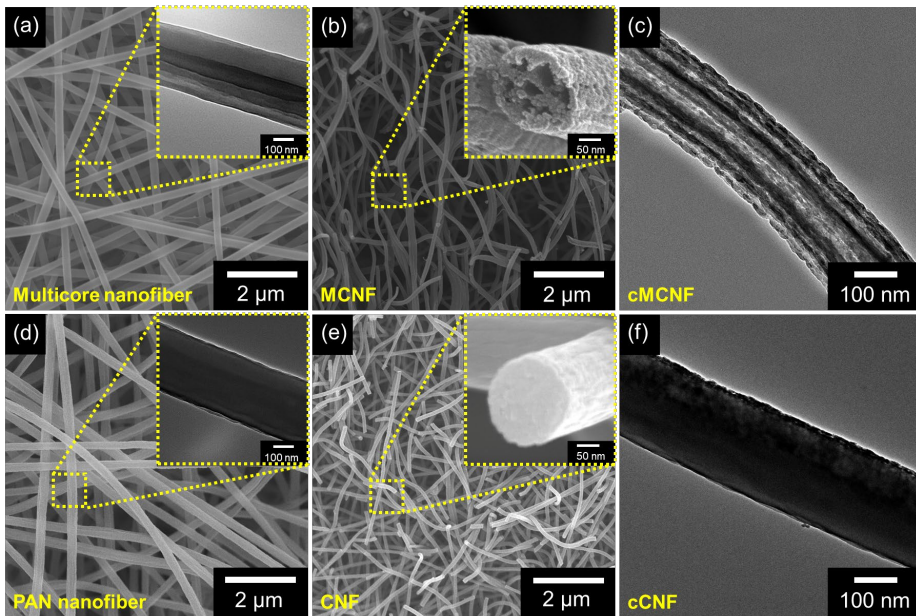


**Figure 25.** (a), (d) FE-SEM and TEM micrographs show the multicore nanofiber and PAN nanofiber, (b), (e) FE-SEM micrographs of the multichannel carbon nanofiber (MCNF) and PAN carbon nanofiber (CNF). The insets of (b) and (e) show the magnified cross-section of MCNF and CNF. (c), (f) TEM micrographs of cMCNF and cCNF.

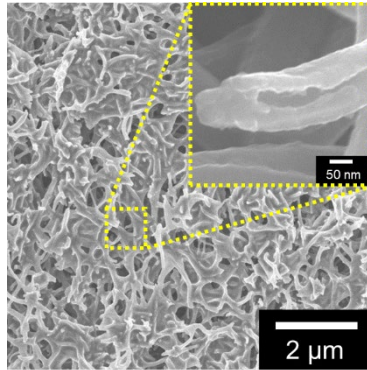


**Figure 26.** FE-SEM micrographs of the over-oxidized MCNFs. The inset shows a magnified image of a MCNF with collapsed multichannel structure when oxidized more than 12 h.

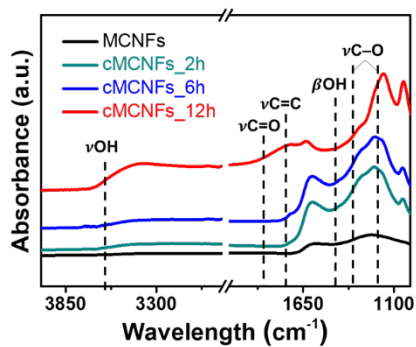


**Figure 27.** FTIR spectra of MCNFs and the cMCNFs formed with oxidation times of 2, 6, and 12 h.

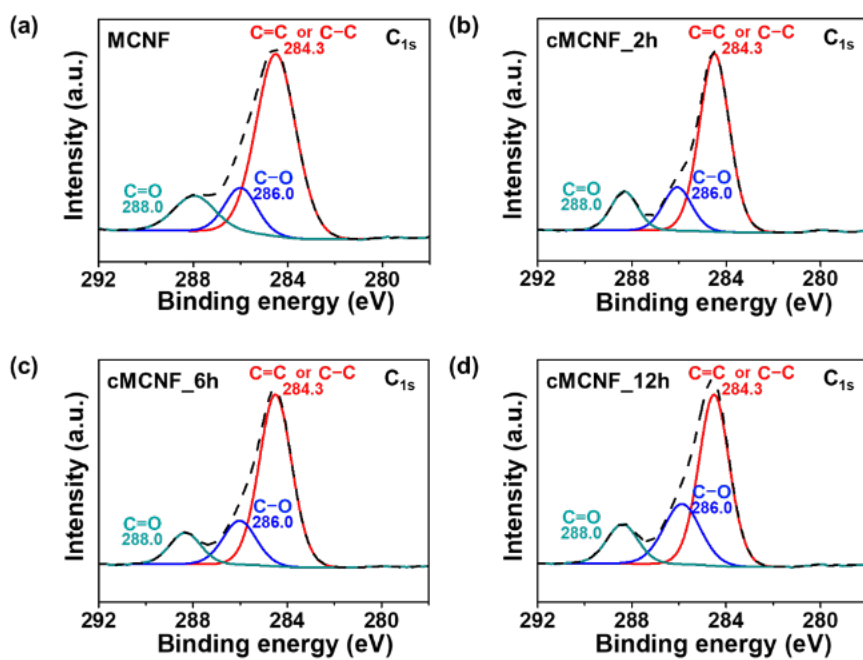


**Figure 28.** XPS C (1s) survey spectra of MCNFs and the cMCNFs formed with oxidation times of 2, 6, and 12 h.

### 3.1.2. Fabrication of bio-receptors-modified MCNFs FET sensors (anti-BPA aptamer & anti-NES1 antibody)

To fabricate a sensitive FET sensor electrode, the transducer cMCNF was located between the binding receptors (anti-BPA aptamer and anti-NES1 antibody) and the electrode *via* covalent bonding of functional groups, respectively. The anti-BPA aptamer-modified MCNF (A-MCNF), the anti-NES1 antibody-modified MCNF (Ab-MCNF), and the anti-NES1 antibody-modified CNF (Ab-CNF) were fabricated through identical coupling reactions. **Figure 29** depicts a schematic illustration detailing the formation of bio-receptors-modified MCNFs on the electrode substrate. The final step of the scheme illustrates the configuration of the FET sensor, which included an electrolyte liquid-ion gate dielectric and the A-MCNF as a conductive channel. An interdigitated array (IDA) consisting of two sets of 25 interdigitated gold electrodes was used as the substrate for immobilization. The surface of the IDA substrate was modified with amine groups ( $\text{—NH}_2$ ) using 3-aminopropyl-trimethoxysilane (APS) and the cMCNFs were fixed to the electrode substrate *via* coupling reactions between the carboxyl groups ( $\text{—COOH}$ ) of the cMCNFs and the  $\text{—NH}_2$  groups of the APS involving the condensation agent 4-(4,6-

dimethoxy-1,3,5-triazin-2-yl)-4-methylmorpholinium chloride (DMT-MM). The carboxyl groups of the cMCNFs enabled the formation of covalent bonds with the substrate, as well as with the binding bio-receptors. In case of anti-BPA-binding aptamer, the 5'-end of the BPA-binding aptamers were decorated with a primary amino group to achieve covalent bonding of the bio-receptors onto the carboxyl group, which was separated from the 5'-end base *via* a six-carbon spacer to reduce steric interaction between the amino group and the oligomer. Subsequently, *via* identical coupling reactions with DMT-MM, the cMCNFs were conjugated to the BPA-binding aptamers without binding to the substrate. In addition, the anti-NES1 antibody modified to the cMCNFs in the same manner as the identical coupling reactions. Especially, as exhibited in **Figure 30** and **Figure 31**, the specific surface area increased due to the formation of internal channels, which increased the quantity of immobilized BPA-binding aptamers. Moreover, there were 5~10 nm mesopores which were pathways of the residual gas during the thermal decomposition process (see **Figure 31b**). Especially, because the size of the binding aptamers was approximately ~2 nm, they could pass through the 5~10 nm-diameter mesopores as well as 20 nm-diameter internal channels of the fibers.

In this manner, A-MCNFs and Ab-MCNFs were immobilized onto the sensor electrode substrate (insets of **Figure 30**).

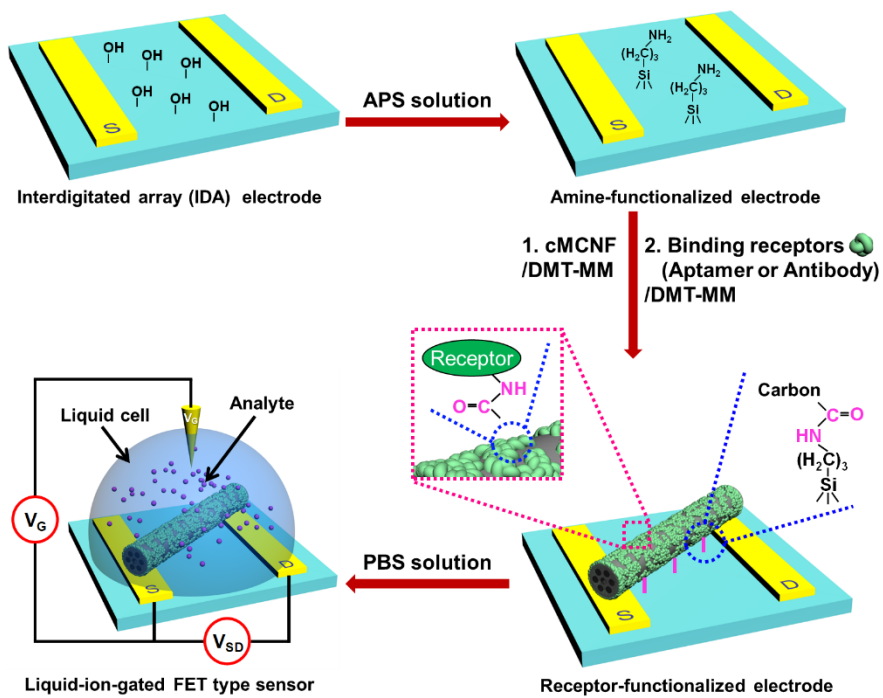


**Figure 29.** Schematic diagram of the immobilization of bio-receptors-modified cMCMFs on the electrode

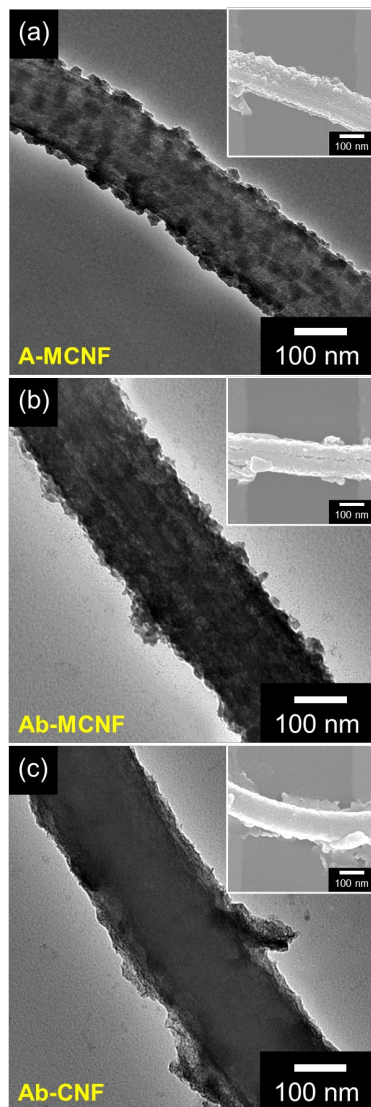


**Figure 30.** TEM micrographs of (a) aptamer-modified MCNF (A-MCNF), (b) antibody-modified MCNF (Ab-MCNF), and (c) antibody-modified CNF (Ab-CNF). The insets are FE-SEM micrographs of the A-MCNF, Ab-MCNF, and Ab-CNF on the IDA electrode, respectively.

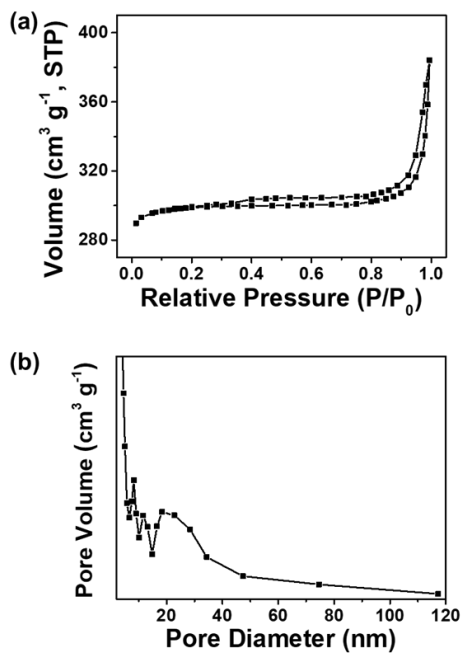


**Figure 31.** (a) N<sub>2</sub> adsorption-desorption isotherm curve (BET surface area: 798.25 m<sup>2</sup>g<sup>-1</sup>) and (b) Barrett-Joyner-Halenda (BJH) pore-size distribution curve for MCNFs.

### 3.1.3. Electrical measurement of anti-BPA aptamer-modified MCNF (A-MCNF) FET sensor detecting BPA

**Figure 32** indicates the current-voltage ( $I$ - $V$ ) characteristics of the A-MCNFs. The linear dependence of the current on the voltage from -0.1 to 0.1 V contrasts with the nonlinear characteristics exhibited by devices that contain Schottky barriers with electrical poor contact at the electrode. Namely, the conductive A-MCNFs formed Ohmic contacts with the electrodes. The  $dV/dI$  value increased with increasing acid treatment time, due to the increase in the number of carboxyl groups. However, the order of magnitude of  $dV/dI$  did not change, and linear Ohmic properties were maintained after aptamer immobilization. These results suggest that covalent immobilization of the aptamers was successful and that the electrical contacts were reproducible. **Figure 32b** means the source-drain current,  $I_{SD}$ , as a function of the source-drain bias,  $V_{SD}$ , with various gate biases,  $V_g$ , for a liquid-ion-gated FET device formed with an acid treatment time of 12 h. Compared with conventional back-gating, liquid-ion gating enabled intimate contact with the CNFs, which increased transconductance. The  $I$ - $V$  measurements show that  $I_{SD}$  increased (became more negative) as  $V_g$  decreased from +0.8 to -1.0 V,

indicating *p*-type behavior (i.e., hole transport). Varying  $V_g$  altered the oxidation level of the cMCNFs and hence the charge carrier distribution.

To evaluate the sensing characteristics of the liquid-ion-gated A-MCNFs FET sensors, changes in  $I_{SD}$  were observed in real-time, with  $V_g = 50$  mV and  $V_{SD} = 50$  mV, during the introduction of solutions containing various concentrations of BPA. **Figure 33a** exhibited the real-time response of sensors formed after oxidization *via* acid treatment for 2, 6, and 12 h. Following the injection of BPA,  $I_{SD}$  decreased rapidly within *ca.* 1 s and saturated. The decrease in  $I_{SD}$  was caused by interactions between BPA and the aptamers during the formation of aptamer–BPA complexes. The immobilized aptamers were negatively charged and BPA binds specifically to the A-MCNFs due to the intermolecular interactions, such as the stacking of aromatic rings, electrostatic, and van der Waals interactions, or hydrogen bonding with target compounds. When the aptamer–BPA complex forms, there may be some structural rearrangement of the aptamer strand, leading to influence the negative charge density at the surface of the A-MCNFs. This induces the screening effect on the negative charge of the aptamers and changes the charge-transport properties of

the A-MCNFs that may reduce the hopping rate of charge carriers, resulting in a decrease in  $I_{SD}$  (**Figure 34**).

As shown in **Figure 33a**, the sensitivity of the A-MCNFs FET sensors increased with acid treatment time. The greater the degree of oxidization of the MCNFs, the denser the chemical functionality; in other words, the amount of carboxylic acid group and immobilized aptamer increased as the acid treatment time increased. For this reason, the A-MCNFs oxidized for 12 h were able to detect BPA rapidly and remarkably down to 1 fM (signal-to-noise ratio  $\geq 3.0$ ), considering other various sensors developed for the analysis of BPA (**Table 1**). **Figure 33b** exhibits the sensitivity,  $S$ , of the A-MCNFs as a function of BPA concentration. The sensitivity was determined from the normalized change in the current (i.e., the saturation level of  $[ΔI/I_0]_{SD} \times 100$  measured after exposure to the analyte for 10 s). Over a large concentration range of  $10^0$ – $10^4$  fM, the sensitivity of the A-MCNF sensor to BPA increased linearly with concentration. The linear equations were as follows:

$$S (\%) = 2.8597 \log C + 1.0768$$

$$S (\%) = 2.7794 \log C - 1.6748$$

$$S (\%) = 2.2235 \log C - 3.4251$$

, where C is BPA concentration (fM). Owing to the enhancement of the functional sites for binding BPA with increasing acid treatment time, the sensitivity of the A-MCNF sensor treated for 12 h was the highest.

In **Figure 35**, The specificity of the A-MCNFs FET sensors was examined using the following BPA structural analogs: 4,4'-(butane-2,2-diyl) diphenol (Bisphenol B, BPB), 4,4-Bis(4-hydroxyphenyl) valeric acid (VA), 4,4'-(hexafluoroisopropylidene) diphenol (6F), and 4,4'-dihydroxybiphenyl (4,4'-Biphenol, BP) (see molecular diagrams in **Figure 36**). The A-MCNFs FET sensor exhibited insignificant changes in  $I_{SD}$  following exposure to 1  $\mu\text{M}$  solution of the structural analogs (i.e., non-target molecules). However, a much larger change in the signal occurred immediately following exposure to a 1 fM solution of BPA, as described in **Figure 35a**. In addition, 1  $\mu\text{M}$  solutions of mixed structural analogs were prepared with and without 1 fM of BPA and were added consecutively and individually to further investigate the specificity. As presented in **Figure 35b**, there was a significant change in  $I_{SD}$  following the introduction of mixtures containing BPA, relative to that experienced without BPA. This

demonstrated that the A-MCNFs FET sensor was highly specific for BPA.

On the basis of the above results of the real-time response, the real samples were prepared to make sure of the sensing performance of the A-MCNFs FET sensor to BPA. Polycarbonate (PC) bottles and thermal printing paper are typical examples that leach out BPA in a hot environment.<sup>62-63</sup> Real examples 1 and 2 were extracted from a PC bottle with hot water and from thermal printing paper immersed in hot ethanol, respectively. **Figure 35c** shows the real-time response of the A-MCNFs FET sensor to actual BPA extracted samples. Owing to the high sensitivity and specificity of the aptasensor, the current signal strikingly changed when the sensor exposed in the serial order of the real samples. Consequently, results presented in **Figure 35** display that the A-MCNFs FET sensor is able to discriminate BPA in real samples and it can be applied to the further applications of BPA determinations.

**Figure 37** depicts the stability of the sensor, based on the responses of various A-MCNFs FET sensors over a period of several weeks. The A-MCNFs FET sensors were maintained in a closed receptacle at 25 °C in dry conditions for 4 weeks. In addition, the signal stability of A-

MCNFs FET sensors with a 1 pM solution of BPA was observed over a period of 7 days. Prior to sequentially dropping target molecules onto the FET sensors, the sensors were washed with PBS solution and rinsing with distilled water to removing salt residues. After 4 weeks, the sensitivity decreased by 87 %, 89 %, and 90 % for sensors formed with 2 h, 6 h, and 12 h acid treatments, respectively. This decrease in sensitivity is attributed to damage to the sensor array or degradation of the binding aptamers. However, the sensing performance was maintained during repeated response tests and the decrease in sensitivity over time was not large. Judging from these results, the stability is attributed to the covalent bonding between the binding aptamers, the cMCNFs, and the electrode substrate. Besides, the binding aptamer itself has its own endurance in the external environment. From this point of view, the A-MCNFs FET sensors are stable and can be reused for repeated assays.

Compared to other several biosensors to detect BPA, the A-MCNFs FET sensors have much superiority in various aspects. The first is an unprecedented limit of detection (LOD) of 1 fM ( $1 \times 10^{-15}$  M) for detecting BPA which is upper than other BPA biosensors including aptamer-based sensors. In addition to the sensitivity, the A-MCNFs

FET sensor responds directly in seconds when exposed to BPA, whereas other methods such as electrochemical or catalytic processes need time. In terms of the cost, the aptasensor utilizes multichannel structured carbon nanofibers which are cheap and facile to fabricate through the electrospinning method. The structural benefit provides enhanced reaction sites to detect BPA extremely low. Considering the above features, the FET sensor consisted of A-MCNFs as a transducer has predominant advantages.

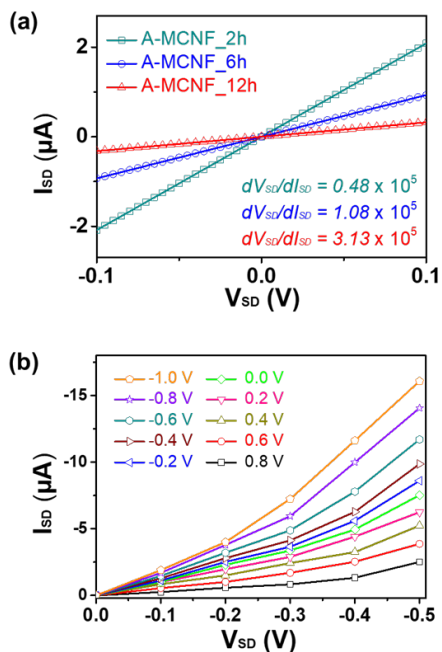


**Figure 32.** (a) Source-drain current-voltage ( $I_{SD}$ - $V_{SD}$ ) curves of sensors formed using A-MCNFs are shown for oxidation times of 2, 6, and 12 h following the introduction of BPA-binding aptamers. (b)  $I_{SD}$ - $V_{SD}$  characteristics of A-MCNFs FET electrodes are shown for gate voltages of  $-1.0 \text{ V} \leq V_g \leq +0.8 \text{ V}$  in steps of 0.2 V with a  $V_{SD}$  scan rate of  $10 \text{ mV s}^{-1}$ .

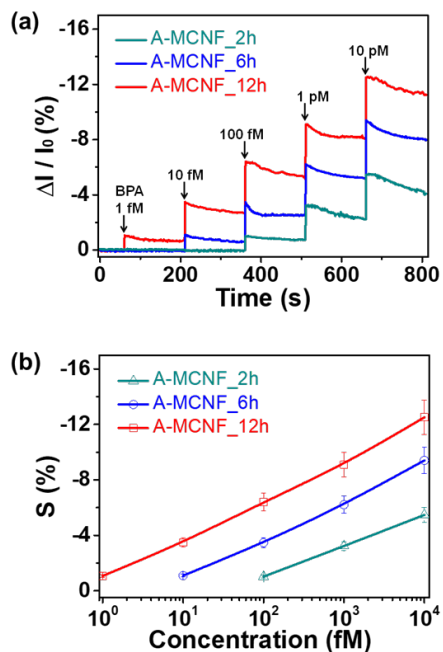


**Figure 33.** (a) Real-time response of the normalized current (i.e.,  $[\Delta I/I_0]_{SD} \times 100$ ) of A-MCNFs FET sensors formed with various oxidation times. (b) Calibration curves of FET sensors formed with various acid treatment times as a function of BPA concentration. Here  $S$  denotes the normalized current following 10 s of exposure to the BPA solution. Dark cyan, blue, and red correspond to oxidation times of 2, 6, and 12 h, respectively. The gate bias was  $V_g = 50$  mV and the source-drain bias was  $V_{SD} = 50$  mV.

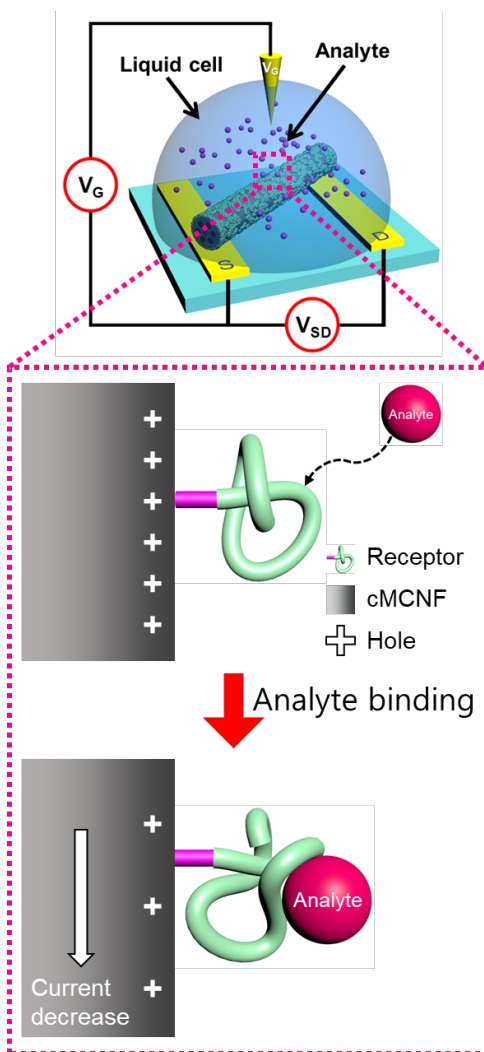


**Figure 34.** Schematic diagram of the sensing mechanism of liquid-ion-gated FET sensor.

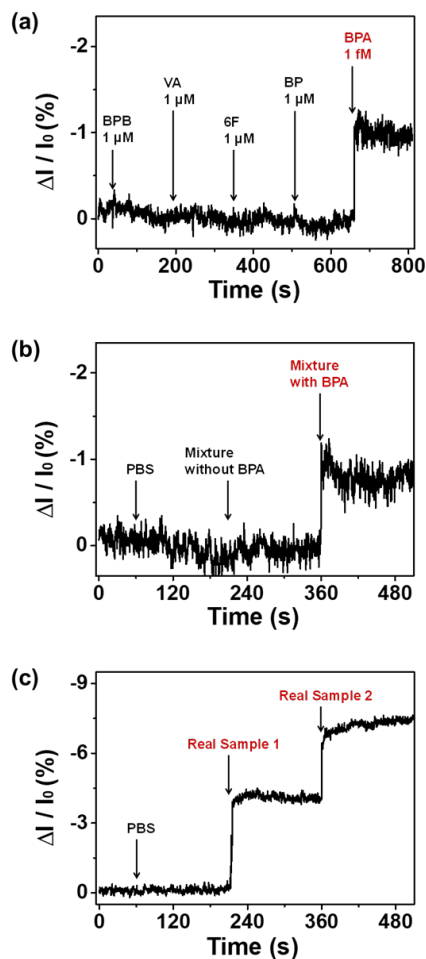


**Figure 35.** The real-time response of A-MCNFs FET sensor (a) to BPA structural analogs BPB, VA, 6F and BP, (b) to various analytes before and after being mixed with BPA, (c) to actual BPA extracted samples (real sample 1: polycarbonate (PC) bottle, sample 2: thermal printing paper). The gate bias was  $V_g = 50$  mV and the source-drain bias was  $V_{SD} = 50$  mV.

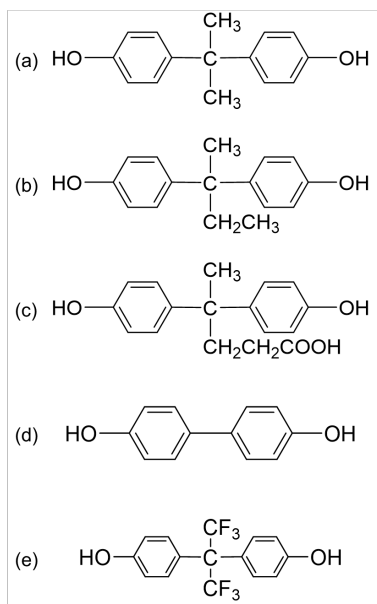


**Figure 36.** Molecular diagrams of the structural analogs of BPA. (a) 4,4'-(propane-2,2-diyl)diphenol (Bisphenol-A, BPA), (b) 4,4'-(butane-2,2-diyl) diphenol (Bisphenol B, BPB), (c) 4,4-Bis(4-hydroxyphenyl) valeric acid (VA), (d) 4,4'-(hexafluoroisopropylidene) diphenol (6F), and (e) 4,4'-dihydroxybiphenyl (4,4'-Biphenol, BP).

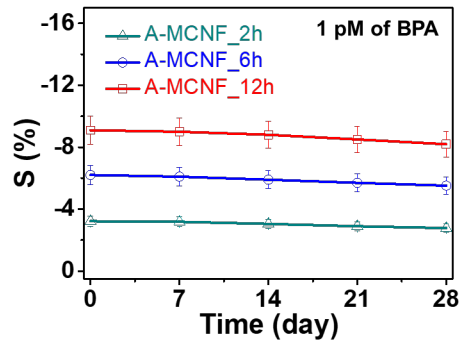


**Figure 37.** Stability of the A-MCNFs FET sensors measured over 4 weeks with intervals of 7 days. Dark cyan, blue, and red correspond to oxidation times of 2, 6, and 12 h, respectively.

**Table 1.** Performances of various sensors developed for the analysis of bisphenol-A (BPA) [199-204]

Type of sensor	Detection element	Detection range	Limit of detection
Electrochemical sensor	Exfoliated graphene electrode	$1.56 - 50 \times 10^{-6}$ M	$7.6 \times 10^{-7}$ M (0.76 $\mu$ M)
Electrochemical sensor	PAMAM-AuNPs-SF <sup>a</sup>	$1 \times 10^{-9}$ $- 1.3 \times 10^{-6}$ M	$0.5 \times 10^{-9}$ M (0.5 nM)
Electrochemical and optical biosensor	Laccase	120 – 500 $\mu$ M	$1.0 \times 10^{-6}$ M (1 $\mu$ M)
Chemi-luminescence Optical sensor	MIP <sup>b</sup>	$1.0 \times 10^{-9}$ $- 2.10 \times 10^{-8}$ g mL <sup>-1</sup>	$7.13 \times 10^{-10}$ g mL <sup>-1</sup> (1.63 $\mu$ M)
Immunosensor	MAbs <sup>c</sup>	-	$0.22 \times 10^{-9}$ M (0.22 nM)
Aptamer-based fluorescence sensor	Aptamer-AuNPs	-	$0.01 \times 10^{-9}$ g L <sup>-1</sup> (2.28 nM)
Aptamer-based FET sensor	A-CMCNFs	100 – 104 fM	$1.0 \times 10^{-15}$ M (1 fM)

<sup>a</sup> PAMAM-AuNPs-SF : poly(amidoamine)-gold nanoparticles-silk fibroin

<sup>b</sup> MIP : molecularly imprinted polymer

<sup>c</sup> MAbs : monoclonal antibodies

### 3.1.4. Electrical measurement of anti-NES1 antibody-modified MCNF (Ab-MCNF) FET sensor detecting NES1

**Figure 38a** indicates the current-voltage ( $I-V$ ) characteristics of the Ab-CNF and Ab-MCNF. Both before and after modified with antibody,  $I-V$  characteristics performed a linear dependence of the current on the voltage from -0.1 to 0.1 V. Namely, the conductive transducer materials formed Ohmic contacts with the electrodes. As the NES1-binding antibody act as resistance, the  $dV/dI$  value increased according to modifying antibody. However, the order of magnitude of  $dV/dI$  did not change, and linear Ohmic properties were maintained after antibody immobilization. These results suggest that covalent immobilization of the antibody was successful and that the electrical contacts were reproducible. In addition, the slope of the cMCNF is lower than cCNF due to the destroyed  $sp^2$  carbon structure which contributes to electrical conductivity. **Figure 38b** and **Figure 38c** means the source-drain current,  $I_{SD}$ , as a function of the source-drain bias,  $V_{SD}$ , with various gate biases,  $V_g$ , for a liquid-ion-gated FET devices formed with Ab-CNF and Ab-MCNF. Compared with conventional back-gating, liquid-ion gating enabled intimate contact with the CNFs, which increased transconductance. The  $I-V$

measurements show that  $I_{SD}$  increased (became more negative) as  $V_g$  decreased from +0.8 to -0.8 V, indicating *p*-type behavior (i.e., hole transport). Varying  $V_g$  altered the oxidation level of the CNFs and hence the charge carrier distribution.

To evaluate the sensing characteristics of the liquid-ion-gated Ab-MCNFs FET sensors, changes in  $I_{SD}$  were observed in real-time, with  $V_g = 50$  mV and  $V_{SD} = 50$  mV, during the introduction of solutions containing various concentrations of NES1 in PBS solution. **Figure 39a** exhibits the real-time response of the Ab-CNF and Ab-MCNF FET sensors. Following the injection of NES1,  $I_{SD}$  decreased rapidly within *ca.* 1 s and saturated. The decrease in  $I_{SD}$  was caused by interactions between NES1 and the antibody during the formation of antibody–NES1 complexes. The NES1 binds specifically to the Ab-MCNFs due to the intermolecular interactions, for example, electrostatic forces, hydrogen bonds, hydrophobic interactions, and van der Waals interactions with target compounds. The antibody–target complex formation leading to influence the negative charge density at the surface of the Ab-MCNFs. This changes the charge-transport properties of the Ab-MCNFs that may reduce the hopping rate of charge carriers, resulting in a decrease in  $I_{SD}$ . As shown in

**Figure 39a**, the sensitivity of the Ab-MCNFs FET sensor performed higher than the Ab-CNFs FET sensor. This result indicates that the change of the surface charge density affected more to the Ab-MCNFs FET sensor than the Ab-CNFs FET sensor. For this reason, the A-MCNFs were able to detect NES1 rapidly and remarkably down to 0.1 fM (signal-to-noise ratio  $\geq 3.0$ ). **Figure 39b** exhibits the sensitivity,  $S$ , of the Ab-MCNFs and Ab-CNFs as a function of NES1 concentration. The sensitivity was determined from the normalized change in the current (i.e., the saturation level of  $[\Delta I/I_0]_{SD} \times 100$  measured after exposure to the analyte for 10 s). Salivary NES1 is normally secreted at levels ranging from 2 pM  $\pm$  300 fM, and remarkably increase in epileptic patients' saliva up to 340 pM  $\pm$  29 pM. Therefore, a biosensor for salivary NES1 needs to contain the range under 1 pM to 1000 pM. Over a large concentration range of  $10^{-5}$ – $10^7$  pM, the sensitivity of the Ab-MCNF and Ab-CNF sensor to NES1 in PBS solution increased linearly with concentration, containing the range of NES1 concentration ( $\sim$ pM) in real saliva.

In **Figure 40**, the specificity of the A-MCNFs FET sensors was examined using non-target samples (glucose, hepatitis B, cortisol) which able to find in real saliva. The Ab-MCNFs FET sensor

exhibited insignificant changes in  $I_{SD}$  following exposure to 1  $\mu\text{M}$  solution of the non-target molecules. However, a much larger change in the signal occurred immediately following exposure to a 100 pM solution of NES1, as described in **Figure 40a**. In addition, 1  $\mu\text{M}$  solutions of mixed non-target molecules were prepared with and without 100 pM of BPA and were added consecutively and individually to further investigate the specificity. As presented in **Figure 40b**, there was a significant change in  $I_{SD}$  following the introduction of mixtures containing NES1, relative to that experienced without NES1. This demonstrated that the Ab-MCNFs FET sensor was highly specific for BPA.

As mentioned, the range of salivary NES1, including normal and epileptic patient, contain 1 pM to 1000 pM. **Figure 41** shows the real-time performance using artificial saliva sample analytes of the Ab-MCNF FET sensor, indicating that as low as 10 fM detection limit and a wide dynamic sensing range including the real-world extent.

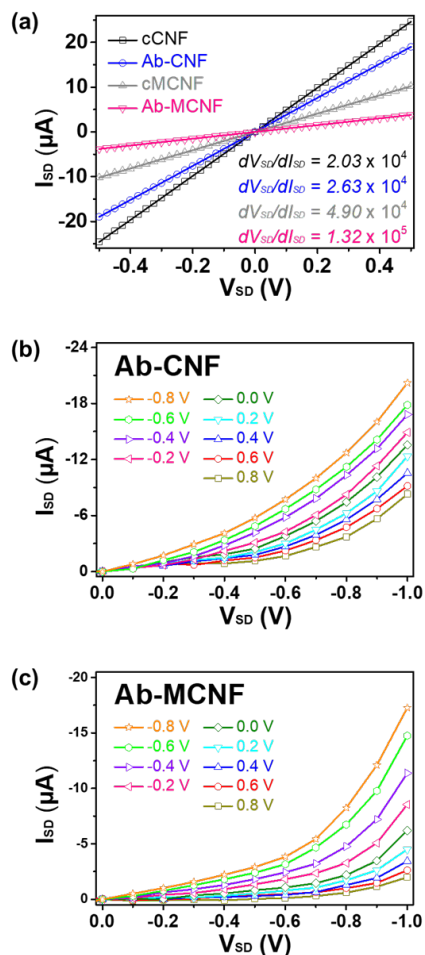


**Figure 38.** (a) Source-drain current-voltage ( $I_{SD}$ - $V_{SD}$ ) curves of sensors formed using Ab-CNFs and Ab-MCNFs which are shown with or without NES1-binding antibody.  $I_{SD}$ - $V_{SD}$  characteristics of (b) Ab-CNF and (c) Ab-MCNFs FET electrodes are shown for gate voltages of  $-0.8 \text{ V} \leq V_g \leq +0.8 \text{ V}$  in steps of 0.2 V with a  $V_{SD}$  scan rate of  $10 \text{ mV s}^{-1}$ .

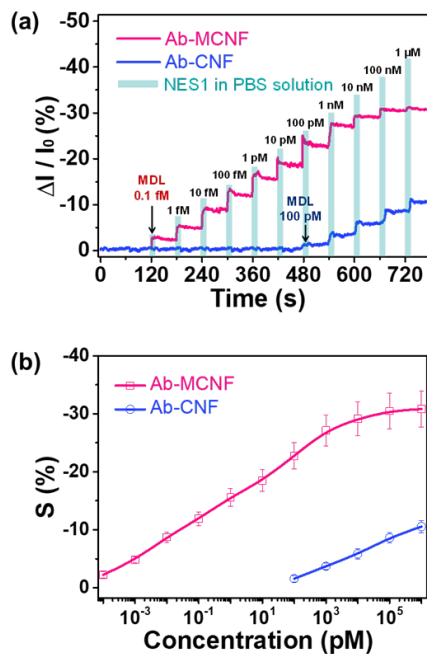


**Figure 39.** (a) Real-time response of the normalized current of Ab-CNFs and Ab-MCNFs FET sensors. (b) Calibration curves of FET sensors formed as a function of NES1 concentration. Here  $S$  denotes the normalized current following 10 s of exposure to the NES1 in PBS solution. The gate bias was  $V_g = 50$  mV and the source-drain bias was  $V_{SD} = 50$  mV.

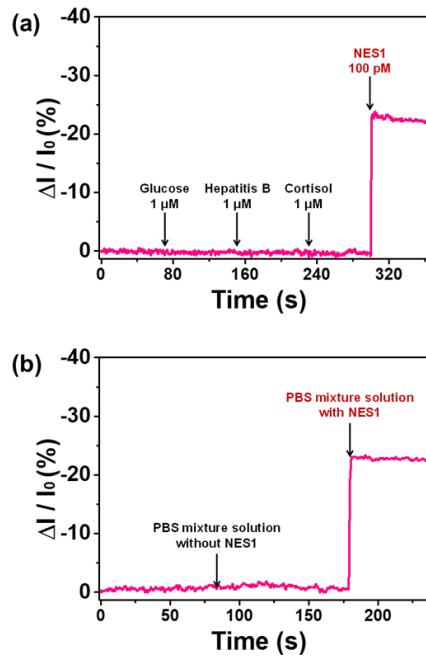


**Figure 40.** The real-time response of Ab-MCNFs FET sensor (a) to non-target (glucose, hepatitis B, cortisol) and target (NES1), (b) to various analytes before and after being mixed with NES1. The gate bias was  $V_g = 50$  mV and the source-drain bias was  $V_{SD} = 50$  mV.

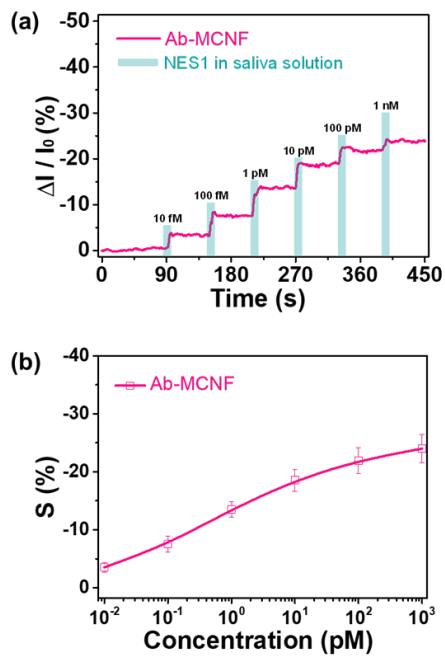


**Figure 41.** (a) Real-time response of the normalized current and (b) calibration curve of Ab-MCNFs FET sensor as various concentrations of NES1 in artificial saliva solution. The gate bias was  $V_g = 50$  mV and the source-drain bias was  $V_{SD} = 50$  mV.

## **3.2. Ruthenium nanoparticles-embedded multichannel carbon nanofibers for liquid-ion-gated non-enzymatic FET sensor detecting dopamine**

### **3.2.1. Fabrication of Ru-mCNF**

**Figure 42** illustrates an overall fabrication of the ruthenium nanoparticles-embedded multichannel carbon nanofiber (Ru-mCNF) based on oxygen plasma treatment. As starting materials, phase-separated multicore polymer nanofibers are fabricated by a single-nozzle co-electrospinning method using a blend solution consisting of two immiscible polymers (PAN and Ru-precursor ( $\text{RuCl}_3$ )-containing PS). PAN and  $\text{RuCl}_3$ -containing PS are separated as surrounding and discontinuous areas due to the surface tension difference in the polymer blend (upper inset of **Figure 22**). Throughout the electrospinning process, the surrounding PAN forms an outer layer of the  $\text{RuCl}_3$ -containing PS area. This effect prohibits the collapse of PS into droplets by towing and stabilizing the PS fluid (lower inset of **Figure 22**). Thus, the surrounding PAN acts as a template for the multicore PS layer in the electrospun polymer nanofibers.

The multicore nanofibers are then treated by oxygen plasma to generate oxygen functional groups in the PAN polymer chain. The

oxygen functional groups (acyl, alkoxy, and peroxy) form chemical bonds with ruthenium ions ( $\text{Ru}^{3+}$ ) in the PS layer and increase the cross-linking of each PAN main chain. Fourier-transform infrared (FTIR) spectra of the multicore nanofibers with and without the oxygen plasma exposure are presented in **Figure 43**. Both multicore nanofibers exhibit peaks related to PAN and PS: aromatic C–H stretching at  $3026\text{ cm}^{-1}$  (PS), C–H stretching at  $2934\text{ cm}^{-1}$  (PAN),  $\text{C}\equiv\text{N}$  stretching at  $2242\text{ cm}^{-1}$  (PAN), aromatic C–C stretching at  $1404$  and  $1452\text{ cm}^{-1}$  (PS), aromatic group at  $755$  and  $697\text{ cm}^{-1}$  (PS). On the other hand, the plasma-treated nanofibers exhibit improved peaks of C=C stretching at  $1595\text{ cm}^{-1}$  in PAN, C=O vibration at  $1730\text{ cm}^{-1}$ , asymmetric C–O–C stretching (at  $1065\text{ cm}^{-1}$ ) and symmetric C–O–C stretching or alkoxy C–O ( $1038\text{ cm}^{-1}$ ). In addition, C–N/C–C stretching at  $1250\text{ cm}^{-1}$ ,  $\text{CH}_3$  deformation at  $1360\text{ cm}^{-1}$ , C=C conjugated dienes in PAN or PS at  $1650\text{ cm}^{-1}$  peaks are reduced. Therefore, after plasma treat, partially stabilized between PAN chains and oxygen-containing radicals are produced in the polymer chain upon the plasma exposure.

The plasma-treated multicore nanofibers are then subjected to conventional heat treatments (stabilization and carbonization) to

convert  $\text{Ru}^{3+}$  and PAN to ruthenium nanoparticles (RuNPs) and carbon, respectively. In the stabilization step, the nanofibers are heated up to 270 °C under controlled air conditions for the cyclization and dehydrogenation of the PAN chains to protect the decomposition during the carbonization. Simultaneously,  $\text{Ru}^{3+}$  bonded to oxygen functional groups in PAN is changed to Ruthenium oxide (RuOx) in response to oxygen in the air. **Figure 44** shows that RuOx nuclei nanoparticles (*ca.* 2 nm  $\pm$  1 nm) are generated in the structure after the stabilization. Additionally, the peroxy radical, one of the oxygen functional groups, increases the cyclization of the PAN chain through the electrophile attack of the nitrile group. The nanofibers are then heated up to 800 °C in an inert atmosphere to synthesize the final product (Ru-mCNF) (**Figure 45**). During the carbonization step, the PAN layer is transformed into a conventional PAN-based carbon structure, while the PS multicore is decomposed without carbon residue. The sizes of the RuNPs are increased (approximately 10  $\pm$  5 nm) as the generated RuOx in the stabilization step acts as a nucleation site and thermally reduced to RuNPs. The inset of the **Figure 45f** shows the HR-TEM image of Ru indicates an interplanar spacing 0.2 nm for the (101) and 0.23 nm for the (100) of hexagonal

close-packed (hcp) ruthenium and confirms growth of pure crystalline nanoparticles. Electron energy-loss spectroscopy (EELS) dot mapping of the Ru-mCNF (**Figure 46**) confirms the elemental composition.

Additionally, to determine the crystallinity and composition of the particles, X-ray diffraction (XRD) (**Figure 47**) using a JCPDS 06-0663 system and X-ray photoelectron spectroscopy (XPS) (**Figure 48**) were used, respectively. In **Figure 47**, mCNF and Ru-mCNF both displays the broad peak from 20~30 degree indicating structure of graphite. The important diffraction peaks corresponding to (100), (002), (101), and (102) planes of RuNPs crystals are indexed to the hcp phase Ru. In **Figure 48a** displays the wide range spectra of mCNF and Ru-mCNF over 0-1350 eV. The XPS spectrum of mCNF reveals only the presence of C, N, and O atoms, while the spectrum of Ru-mCNF expresses the presence of C, N, O, and Ru atoms. The presence of Ru atoms in the Ru-mCNF spectrum indicates that RuNPs are formed on the mCNF. The O 1s peak region of Ru-mCNF is slightly more intense than that of mCNF, which means more oxygen-containing functional groups remained on Ru-mCNF. **Figure 48b** describes the high-resolution of Ru3p, displaying that two peaks with binding energy values of 462.27 eV for Ru3p<sub>3/2</sub> and 484.5 eV for

Ru3p<sub>1/2</sub> show the valance state of Ru<sup>+3</sup>. The C1s high-resolution spectrum of Ru-mCNF is exhibited in **Figure 48d**. Because the spin-orbit split doublet corresponds to zero-valent metallic state Ru3d<sub>5/2</sub> and Ru3d<sub>3/2</sub>, two peaks with binding energy values of 280.7 eV and 284.8 eV show the valance state of Ru<sup>+3</sup>. Compared to **Figure 48c**, Ru3d<sub>5/2</sub> peak at 280.7 is found because XPS peaks of C1s and Ru3d are overlapped at similar binding energy. **Figure 48e** and **Figure 48f** indicate that the intensity of the oxygen-containing functional groups increased and Ru–O peak appeared. Therefore, RuNPs as Ru<sup>0</sup> were well-formed on mCNFs.

Furthermore, the size and density of the decorated RuNPs were controlled by the concentration of the RuCl<sub>3</sub>, which varied from 0.05 to 0.15 g. The Ru-mCNFs with 0.05, 0.10, and 0.15 g RuCl<sub>3</sub> are denoted as Ru-mCNF\_0.05, Ru-mCNF\_0.10, and Ru-mCNF\_0.15, respectively. **Figure 49** shows TEM images of the Ru-mCNFs with increasing amount of precursor. The size and density of decorated Ru particles are increased with the amount of precursor. Raman spectroscopy presents the microstructure of the mCNF and Ru-mCNF (**Figure 50**). The main two peaks of 1350 cm<sup>-1</sup> and 1590 cm<sup>-1</sup> are D band and G band, respectively, indicating disordered carbon and

graphite. The ratio of the D and G bands ( $I_D/I_G$ ) corresponds to the  $sp^3/sp^2$  carbon ratio. This ratio represents the degree of graphitization of the carbon structure. The ratio of the four patterns tends to slightly decrease with no significant difference. According to the amount of Ru, the Ru-mCNF\_0.05, Ru-mCNF\_0.10, and Ru-mCNF\_0.15 show increasing peaks at  $645^{-1}$  and  $680\text{ cm}^{-1}$ , representing the presence and intensity of Ru. In short, the size and density of the RuNPs are increased with the amount of precursor.

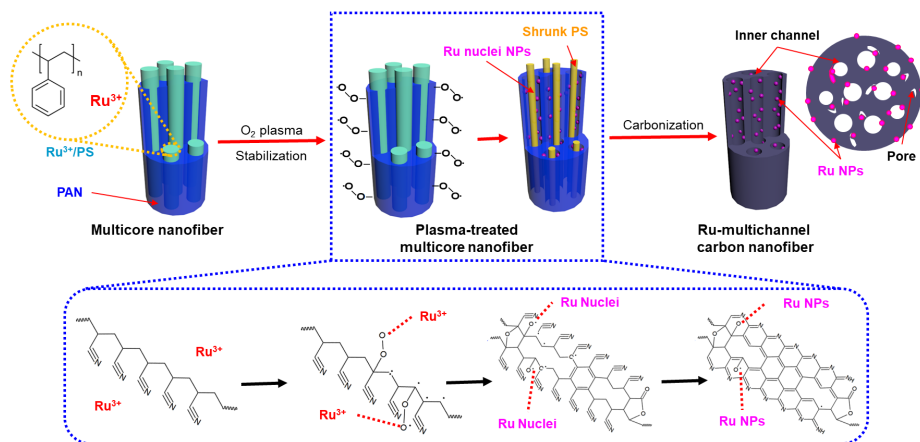


**Figure 42.** Illustration of the sequential synthesis of the Ru-mCNF. (The inset: structural changes of the electrospun multicore nanofibers after each fabrication step.)

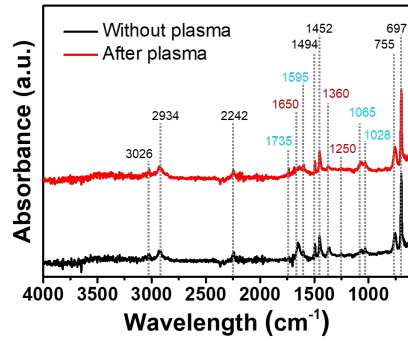


**Figure 43.** Fourier-transform infrared (FTIR) spectra of the electrospun multicore nanofibers (PAN/PS/RuCl<sub>3</sub>) before (black) and after (red) oxygen plasma treatment.

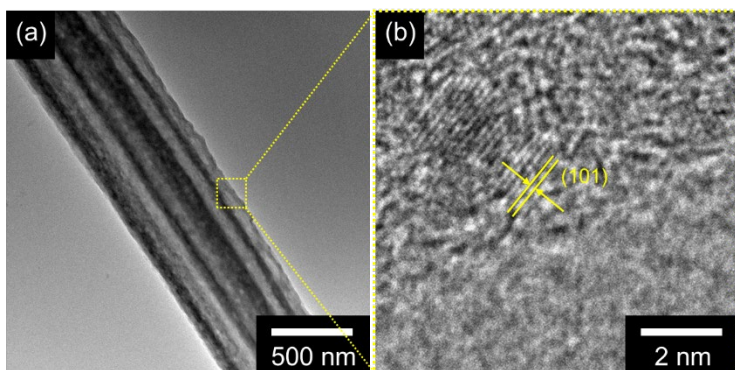


**Figure 44.** (a) TEM and (b) HR-TEM images of stabilized multicore nanofiber after oxygen plasma.

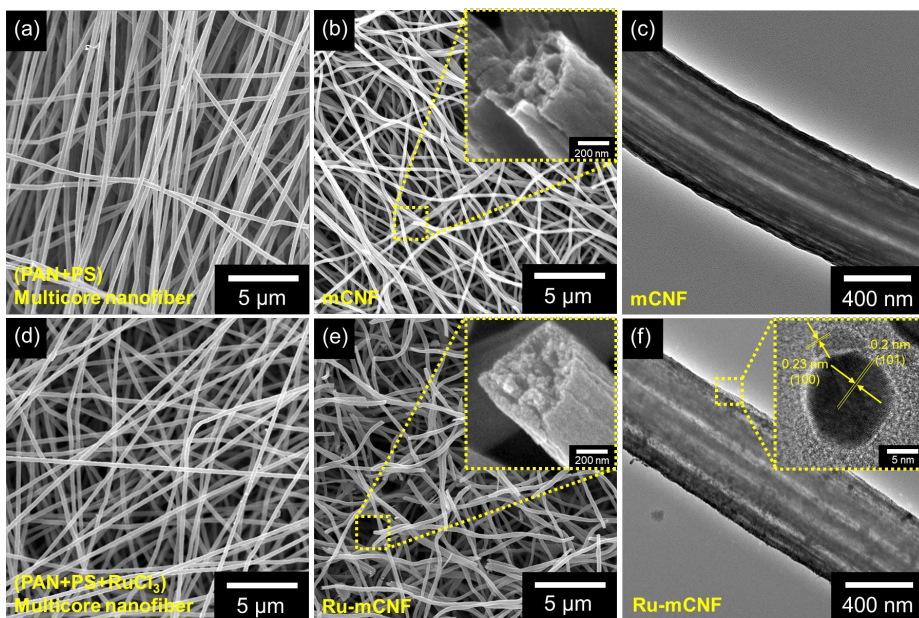


**Figure 45.** (a), (d) FE-SEM micrographs show the multicore nanofiber without or with ruthenium precursor, (b), (e) FE-SEM micrographs of the multichannel carbon nanofiber (mCNF) and ruthenium nanoparticles-embedded mCNF (Ru-mCNF). The insets of (b) and (e) show the magnified cross-section of mCNF and Ru-mCNF. (c), (f) TEM micrographs of mCNF and Ru-mCNF. The inset of (f) show a high-resolution TEM (HR-TEM) image of the ruthenium nanoparticle component in the carbon nanofiber structure.

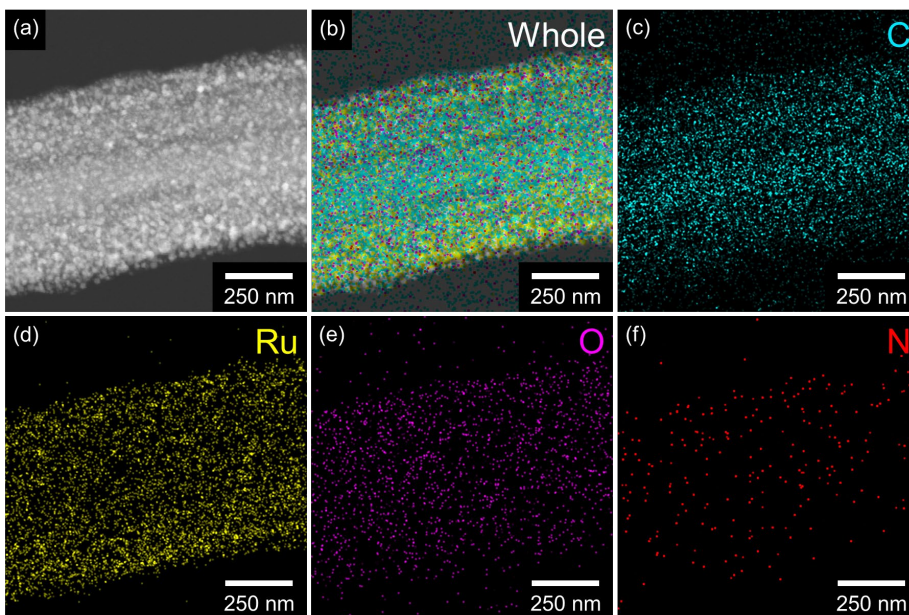


**Figure 46.** Electron energy-loss spectroscopy (EELS) dot mapping of the Ru-mCNF (cyan: C, yellow: Ru, magenta: O, red: N)

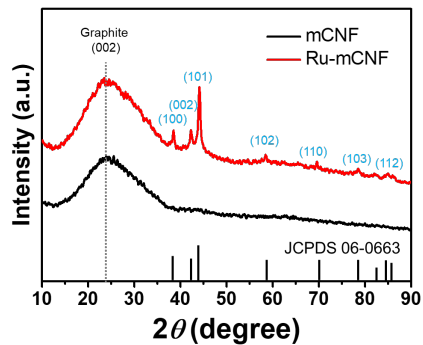


**Figure 47.** X-ray diffraction (XRD) spectra of mCNF (black) and Ru-mCNF (red).

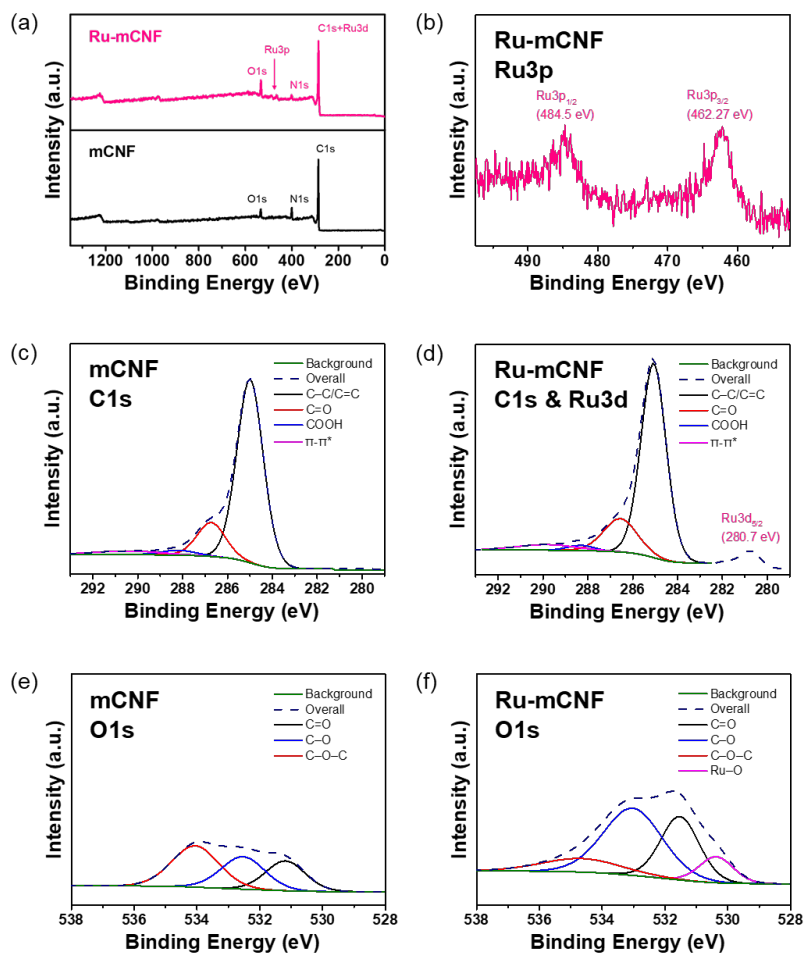


**Figure 48.** X-ray photoelectron spectroscopy (XPS) spectra of (a) Ru-mCNF and mCNF, (b) High-resolution Ru3p XPS spectra of Ru-mCNF. High-resolution C1s, O1s XPS spectra of (c), (e) mCNF and (d), (f) Ru-mCNF.

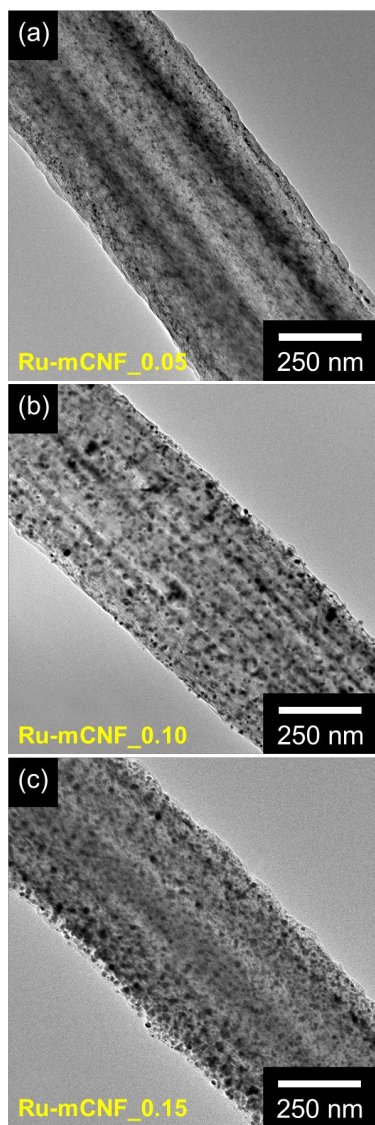


**Figure 49.** TEM micrographs of Ru-mCNFs with various amount of ruthenium precursor (0.05, 0.10, 0.15 g) resulting various RuNPs size distribution.

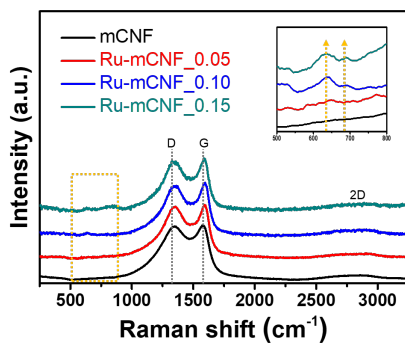


**Figure 50.** Raman spectra of (black) mCNF, (red) Ru-mCNF\_0.05, (blue) Ru-mCNF\_0.10, and (dark cyan) Ru-mCNF\_0.15.

### 3.2.2. Fabrication of Ru-mCNFs non-enzymatic FET sensor

The stability in the liquid-ion solution is a critical factor in the fabrication of highly sensitive non-enzyme FET sensor electrodes. To improve stability, the immobilization of the transducer on the sensor electrode is achieved via the covalent bonding of functional groups. **Figure 51** provides a schematic diagram of the procedure for the Ru-mCNF based non-enzyme FET sensor configuration. An interdigitated microelectrode array (IDA), composed of pairs of 25 lines of gold fingers on the glass plate, was used as an immobilization substrate of Ru-mCNF. The IDA glass substrate was treated with 3-aminopropyl-trimethoxysilane (APS) to functionalize the surface with amine groups ( $-\text{NH}_2$ ). Subsequently, the Ru-mCNFs were anchored to the substrate through a condensation reaction between the carboxyl group ( $-\text{COOH}$ ) of the CNFs and the  $-\text{NH}_2$  of the substrate involving the condensing agent (4-(4,6-dimethoxy-1,3,5-triazin-2-yl)-4-methylmorpholinium chloride (DMT-MM)). As a result, Ru-mCNFs were immobilized on the electrode substrate, and they demonstrated outstanding stability against environmental perturbation. Then, the Ru-mCNFs-immobilized IDA was formed FET-sensor platform with a PBS buffer solution (pH 7.4) as an electrolyte. In the FET configuration, two gold

IDA bands were the source (S) and drain (D) electrodes, and the gate electrode was immersed in the electrolyte. The gate potential ( $V_G$ ) was applied to the source electrode through a buffer solution. The distance between electrodes was fixed at 2 mm based on the resistivity of the buffer solution.

### 3.2.3. Electrical measurement of Ru-mCNFs non-enzymatic FET sensor

**Figure 52a** indicates the current-voltage ( $I$ - $V$ ) characteristics of the Ru-mCNFs. The linear dependence of the current on the voltage from -0.1 to 0.1 V contrasts with the nonlinear characteristics exhibited by devices that contain Schottky barriers with electrical poor contact at the electrode. Namely, the conductive Ru-mCNFs formed Ohmic contacts with the electrodes. The  $dV/dI$  value increased with an increasing amount of Ru. However, the order of magnitude of  $dV/dI$  did not change, and linear Ohmic properties were maintained after aptamer immobilization. These results suggest that the electrical contacts were reproducible. **Figure 52b** means the source-drain current,  $I_{SD}$ , as a function of the source-drain bias,  $V_{SD}$ , with various gate biases,  $V_g$ , for a liquid-ion-gated FET device formed with Ru-mCNF\_0.15. Compared with conventional back-gating, liquid-ion gating enabled intimate contact with the CNFs, which increased transconductance. The  $I$ - $V$  measurements show that  $I_{SD}$  increased (became more negative) as  $V_g$  decreased from +0.6 to -0.8 V, indicating  $p$ -type behavior (i.e., hole transport). Varying  $V_g$  altered the

oxidation level of the Ru-mCNFs and hence the charge carrier distribution.

The Ru-mCNFs-immobilized FET sensor rapidly detects dopamine (DA) molecules at room temperature. The sensing mechanism of the Ru-mCNFs is described as shown in **Figure 53**. The mCNF surface is adsorbed to dopamine molecules by  $\pi$ - $\pi$  interactions through conjugated carbon ring of mCNF and six-membered benzene ring of dopamine structure. The adsorbed dopamine is electro-oxidized to O-dopaminequinone at the surface of the Ru particles through catalytic effect and electrons, originated from dopamine, are transferred to mCNF, leading to a decrease in the number of holes in the mCNF structure and diminishing  $I_{SD}$  (because of the mCNF acting as a p-type transducer).

To evaluate the sensing characteristics of the liquid-ion-gated Ru-mCNFs FET sensors, changes in  $I_{SD}$  were observed in real-time, with  $V_g = 50$  mV and  $V_{SD} = 50$  mV, during the introduction of solutions containing various concentrations of dopamine. **Figure 54a** exhibited the real-time response of sensors with mCNF, Ru-mCNF\_0.05, Ru-mCNF\_0.10, and Ru-mCNF\_0.15. Following the injection of dopamine,  $I_{SD}$  decreased rapidly within *ca.* 1 s and saturated. The

sensitivity of the Ru-mCNFs FET sensors increased with the amount of ruthenium; that is, the Ru-mCNF FET sensor made from the Ru-mCNF\_0.15 is capable of detecting dopamine rapidly and remarkably down to 1 fM (signal-to-noise ratio  $\geq 3.0$ ). **Figure 54b** exhibits the sensitivity,  $S$ , of the Ru-mCNFs as a function of dopamine concentration. The sensitivity was determined from the normalized change in the current (i.e., the saturation level of  $[ΔI/I_0]_{SD} \times 100$  measured after exposure to the analyte for 10 s). Over a large concentration range of  $10^{-3}$ – $10^4$  pM, the sensitivity of the Ru-mCNF sensor to dopamine increased linearly with concentration.

In **Figure 55**, The specificity of the Ru-mCNFs FET sensors was examined using the following non-target molecules: epinephrine (EP), norepinephrine (NE), phenethylamine (PEA), tyrosine (TR), ascorbic acid (AA), and uric acid (UA) (see molecular diagrams in **Figure 56**). UA and AA appear with dopamine in some animal tissues. Since NE and EP are catecholamines, their molecular structures are similar to that of dopamine. PEA and TR are selected owing to not only their similar molecular structures being similar to that of dopamine but also their appearance with dopamine in some animal tissues. The A-mCNFs FET sensor exhibited insignificant changes in  $I_{SD}$  following

exposure to 1 pM solutions of the non-target molecules: however, considerable changes occurred following exposure to a 1 fM solution of dopamine (**Figure 55a**). Despite the similar structure of PEA and TR with dopamine, there are no current changes due to the absence of catechol structures that induced the catalytic reaction between Ru and analytes. AA and UA also display no significant current change due to the absence of phenyl groups in their molecular structures, which led to only weak  $\pi$ - $\pi$  interactions between the receptor and analyte. NE and EP presented unimpressive sensitivity to the Ru-mCNF FET sensor compared with dopamine. Inspect of the molecular structure, the additional functional groups (-OH and -CH<sub>3</sub>) at the ethylamine group enlarged the size of biomolecules. Consequently, the increased size of these biomolecules reduced the effects of  $\pi$ - $\pi$  interactions and catalytic activities of the RuNPs. Additionally, to further confirm the selectivity of the FET sensors, real-time responses were conducted with the addition of non-target molecule mixtures (10 pM) with or without 1 pM dopamine. **Figure 55b** shows significant signal changes after the addition of mixtures containing dopamine, compared with the signal obtained for mixtures without dopamine. The  $\pi$ - $\pi$  interaction between the phenyl structure of DA and mCNF structure is attributed

to the easily adsorbed DA molecules to the surface of the Ru-mCNF-based electrode. As a result, the Ru-mCNF FET sensor exhibits high selectivity to the dopamine molecules in the presence of excess interferences.

**Figure 57** depicts the stability of the sensor, based on the responses of various Ru-mCNFs FET sensors over a period of several weeks. The Ru-mCNFs FET sensors were maintained in a closed receptacle at 25 °C in dry conditions for 4 weeks. In addition, the signal stability of Ru-mCNFs FET sensors with a 1 pM solution of dopamine was observed over a period of 7 days. Prior to sequentially dropping target molecules onto the FET sensors, the sensors were washed with PBS solution and rinsing with distilled water to removing salt residues. After 4 weeks, the sensitivity decreased by 87.8 %, 90.2 % and 93.2 % for sensors formed with Ru-mCNF\_0.05, Ru-mCNF\_0.10. and Ru-mCNF\_0.15, respectively.

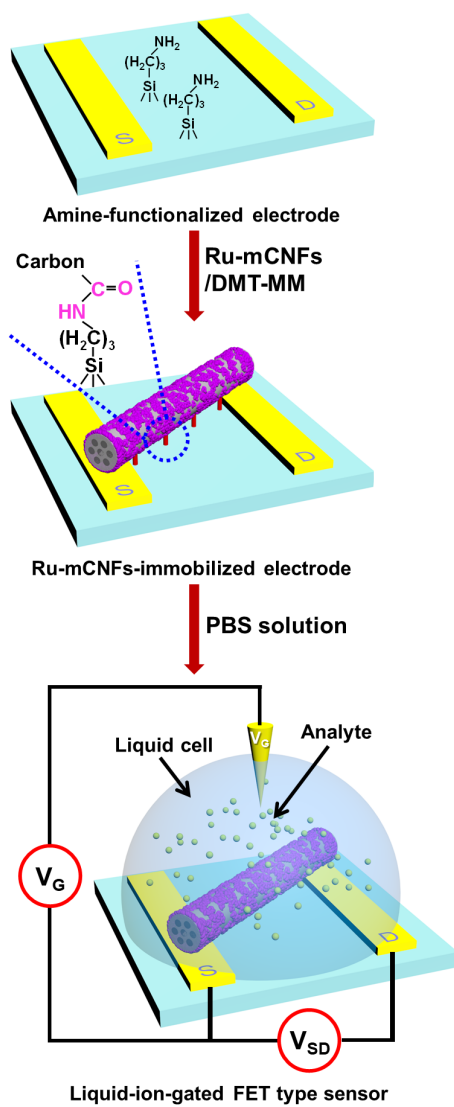


**Figure 51.** Schematic illustration of the liquid-ion-gated FET with the immobilized Ru-mCNF arrays on the IDA electrode.

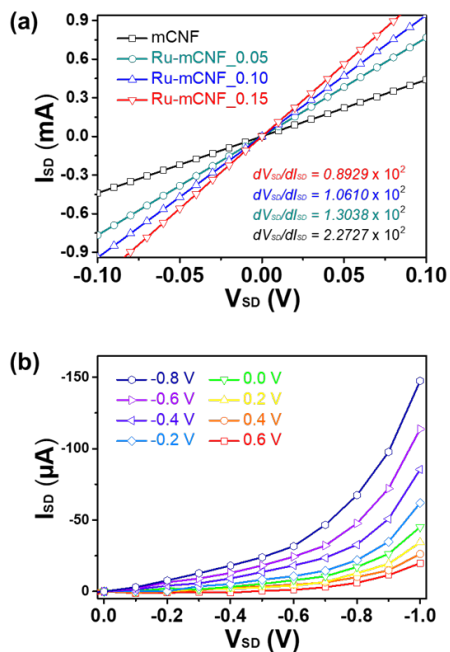


**Figure 52.** (a) Source-drain current-voltage ( $I_{SD}$ - $V_{SD}$ ) curves of sensors with mCNF, Ru-mCNF\_0.05, Ru-mCNF\_0.10, and Ru-mCNF\_0.15. (b)  $I_{SD}$ - $V_{SD}$  characteristics of Ru-mCNFs FET electrodes are shown for gate voltages of  $-0.8 \text{ V} \leq V_g \leq +0.6 \text{ V}$  in steps of  $0.2 \text{ V}$  with a  $V_{SD}$  scan rate of  $10 \text{ mV s}^{-1}$ .

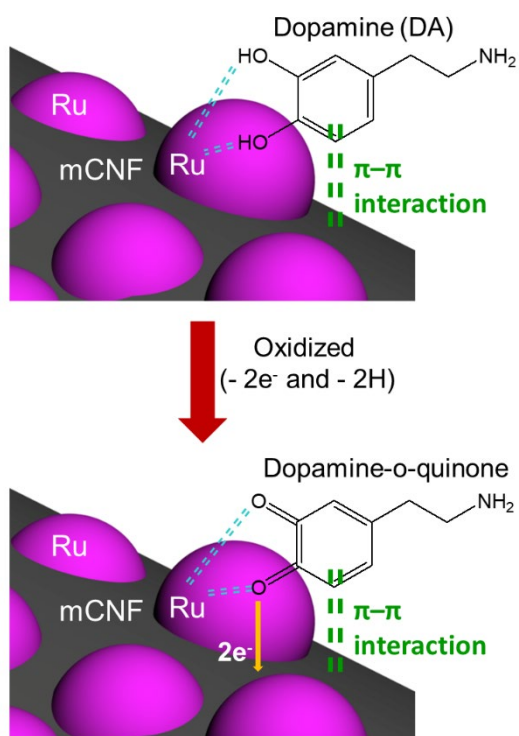


**Figure 53.** Schematic diagram of the dopamine sensing mechanism of liquid-ion-gated non-enzymatic FET sensor.

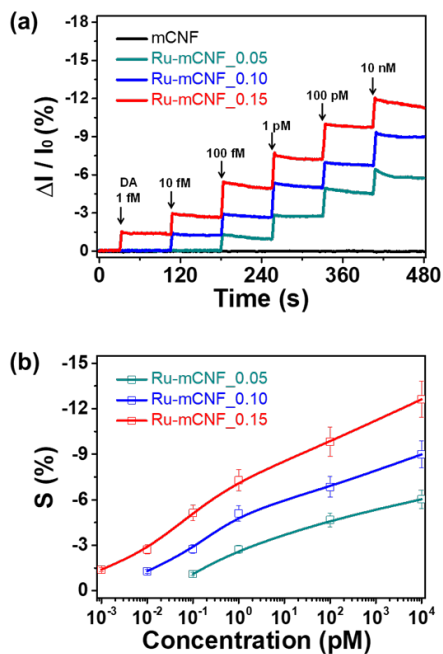


**Figure 54.** (a) Real-time response of the normalized current (i.e.,  $[\Delta I/I_0]_{SD} \times 100$ ) of Ru-mCNFs FET sensors. (b) Calibration curves of FET sensors formed with various ruthenium amounts as a function of DA concentration. Here  $S$  denotes the normalized current following 10 s of exposure to the DA solution. Dark cyan, blue, and red correspond to ruthenium precursor 0.05, 0.10, and 0.15 g, respectively. The gate bias was  $V_g = 50$  mV and the source-drain bias was  $V_{SD} = 50$  mV.

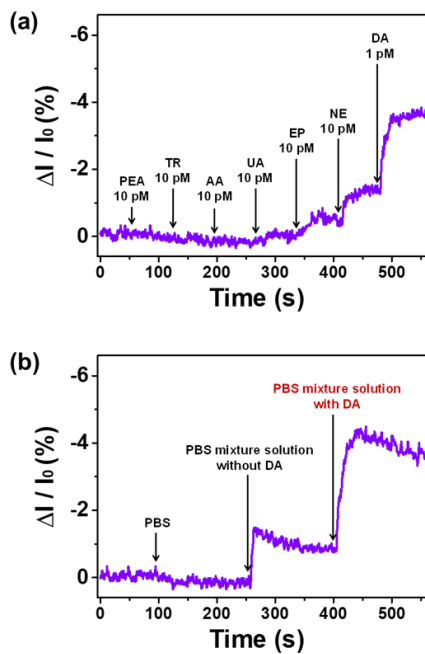


**Figure 55.** The real-time response of Ru-mCNFs FET sensor (a) to various non-target (phenethylamine (PEA), tyrosine (TR), ascorbic acid (AA), uric acid (UA), epinephrine (EP), and norepinephrine (NE)) analytes and target (dopamine (DA)), and (b) to various analytes before and after being mixed with NES1. The gate bias was  $V_g = 50$  mV and the source-drain bias was  $V_{SD} = 50$  mV.

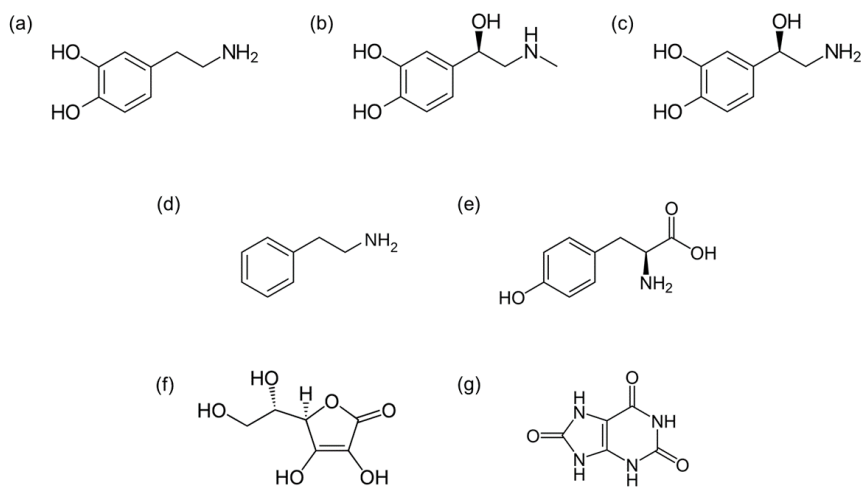


**Figure 56.** Molecular diagrams of (a) dopamine (DA), (b) epinephrine (EP), (c) norepinephrine (NE), (d) phenethylamine (PEA), (e) tyrosine (TR), (f) ascorbic acid (AA), and (g) uric acid (UA).

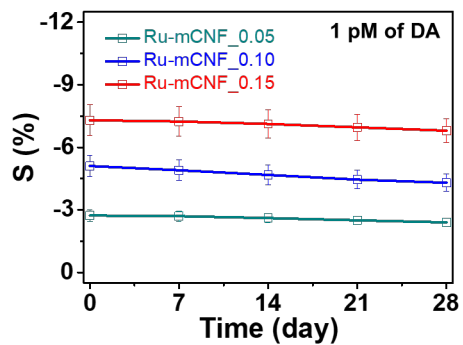


**Figure 57.** Stability of the Ru-mCNFs FET sensors measured over 4 weeks with intervals of 7 days. Dark cyan, blue, and red correspond to Ru-mCNF\_0.05, Ru-mCNF\_0.10, and Ru-mCNF\_0.15, respectively.

### **3.3. Iron oxide nanoparticles-embedded multichannel carbon nanofibers for resistive type wireless chemical sensor detecting hydrogen sulfide**

#### **3.2.1. Fabrication of Fe-mCNF**

**Figure 58** illustrates an overall fabrication of the iron oxide nanoparticles-embedded multichannel carbon nanofiber (Fe-mCNF) based on oxygen plasma treatment. As starting materials, phase-separated multicore polymer nanofibers are fabricated by a single-nozzle co-electrospinning method using a blend solution consisting of two immiscible polymers (PAN and Fe-precursor-(FeCl<sub>3</sub>)-containing PS). Since the surface tensions of PAN and FeCl<sub>3</sub>-containing PS are different in the polymer blend, these are separated as surrounding and discontinuous areas (upper inset of **Figure 22**). Throughout the electrospinning process, the surrounding PAN forms an outer layer of the FeCl<sub>3</sub>-containing PS area. This effect prohibits the collapse of PS into droplets by towing and stabilizing the PS fluid (lower inset of **Figure 22**). Thus, the surrounding PAN acts as a template for the multicore PS layer in the electrospun polymer nanofibers.

The multicore nanofibers are then treated by oxygen plasma to generate oxygen functional groups in the PAN polymer chain. The

oxygen functional groups (acyl, alkoxy, and peroxy) form chemical bonds with ruthenium ions ( $\text{Fe}^{3+}$ ) in the PS layer and increase the cross-linking of each PAN main chain. Fourier-transform infrared (FTIR) spectra of the multicore nanofibers with and without the oxygen plasma exposure are presented in **Figure 59**. Both multicore nanofibers exhibit peaks related to PAN and PS: aromatic C–H stretching at  $3026\text{ cm}^{-1}$  (PS), C–H stretching at  $2934\text{ cm}^{-1}$  (PAN),  $\text{C}\equiv\text{N}$  stretching at  $2242\text{ cm}^{-1}$  (PAN), aromatic C–C stretching at  $1404$  and  $1452\text{ cm}^{-1}$  (PS), aromatic group at  $755$  and  $697\text{ cm}^{-1}$  (PS). On the other hand, the plasma-treated nanofibers exhibit improved peaks of C=C stretching at  $1595\text{ cm}^{-1}$  in PAN, C=O vibration at  $1730\text{ cm}^{-1}$ , asymmetric C–O–C stretching (at  $1065\text{ cm}^{-1}$ ) and symmetric C–O–C stretching or alkoxy C–O ( $1038\text{ cm}^{-1}$ ). In addition, C–N/C–C stretching at  $1250\text{ cm}^{-1}$ ,  $\text{CH}_3$  deformation at  $1360\text{ cm}^{-1}$ , C=C conjugated dienes in PAN or PS at  $1650\text{ cm}^{-1}$  peaks are reduced. Therefore, after plasma treat, partially stabilized between PAN chains and oxygen-containing radicals are produced in the polymer chain upon the plasma exposure.

The plasma-treated multicore nanofibers are then subjected to heat treatments (stabilization and carbonization) to convert  $\text{Fe}^{3+}$  and PAN

to iron oxide nanoparticles ( $\text{Fe}_2\text{O}_3$  NPs) and carbon, respectively. In the stabilization step, the nanofibers are heated up to  $250\text{ }^\circ\text{C}$  under controlled air conditions for the cyclization and dehydrogenation of the PAN chains to protect the decomposition during the carbonization. Simultaneously,  $\text{Fe}^{3+}$  bonded to oxygen functional groups in PAN is changed to iron oxide ( $\text{FeOx}$ ) in response to oxygen in the air. Additionally, the peroxy radical, one of the oxygen functional groups, increases the cyclization of the PAN chain through the electrophile attack of the nitrile group. The nanofibers are then heated up to  $600\text{ }^\circ\text{C}$  in an inert atmosphere to synthesize the final product ( $\text{Fe-mCNF}$ ). During the carbonization step, the PAN layer is transformed into a conventional PAN-based carbon structure, while the PS multicore is decomposed without carbon residue. The sizes of the  $\text{Fe}_2\text{O}_3$  NPs are increased (approximately  $15 \pm 5\text{ nm}$ ) as the generated  $\text{FeOx}$  in the stabilization step acts as a nucleation site.

**Figure 60** shows low- and high-magnified TEM images of the  $\text{Fe-mCNFs}$  with an increasing amount of precursor. The size and density of the decorated  $\text{FeNPs}$  were controlled by the amount of the  $\text{FeCl}_3$ , which varied from 0.10 to 0.24 g. The  $\text{Fe-mCNFs}$  with 0.10, 0.16, and 0.24 g  $\text{FeCl}_3$  are denoted as  $\text{Fe-mCNF}_{0.10}$ ,  $\text{Fe-mCNF}_{0.16}$ , and  $\text{Fe-}$

mCNF\_0.24, respectively. Scanning TEM and energy dispersive spectroscopy (STEM-EDS) line mapping of the Fe-mCNF and Electron energy-loss spectroscopy (EELS) dot mapping of the Fe-mCNF (**Figure 61**) confirms the elemental composition. **Figure 61a** indicates remained multichannel structure from line C, and Fe<sub>2</sub>O<sub>3</sub> nanoparticles are well-dispersed on the Fe-mCNF from line O and Fe. The EELS dot mapping images (**Figure 61b~f**) indicate that each atomic component (iron, oxygen, carbon, and nitrogen) is located in the multichannel structure of the Fe-mCNF.

**Figure 62** shows the HR-TEM image of Fe indicates an interplanar spacing 0.25 nm for the (110) and 0.27 nm for the (104) of hematite Fe<sub>2</sub>O<sub>3</sub> and confirms that  $\alpha$ -Fe<sub>2</sub>O<sub>3</sub> phase is generated after heat treatment step. Additionally, to determine the crystallinity of the particles, X-ray diffraction (XRD) (**Figure 63**) using a JCPDS 33-0664 system was used. The peaks both in the mCNF and Fe-mCNF displays the broad peak from 20~30 degrees indicating the structure of graphite. The peaks of the inorganic materials in the Fe-mCNF are well-matched  $\alpha$ -Fe<sub>2</sub>O<sub>3</sub> phase (hematite), indicating the formation of  $\alpha$ -Fe<sub>2</sub>O<sub>3</sub> nanoparticles into the carbon structure.

Raman spectroscopy presents the microstructure of the mCNF and Fe-mCNF (**Figure 64**). The main two peaks of  $1350\text{ cm}^{-1}$  and  $1590\text{ cm}^{-1}$  are D band and G band, respectively, indicating disordered carbon and graphite. The ratio of the D and G bands ( $I_D/I_G$ ) corresponds to the  $\text{sp}^3/\text{sp}^2$  carbon ratio. This ratio represents the degree of graphitization of the carbon structure. The ratio of the four patterns tends to slightly increase according to the amount of  $\text{Fe}_2\text{O}_3$ . In addition, the Fe-mCNF\_0.10, Fe-mCNF\_0.16, and Fe-mCNF\_0.24 show increasing peaks at  $222\text{ cm}^{-1}$  and  $289\text{ cm}^{-1}$ , representing the presence and intensity of hematite. In short, the size and density of  $\text{Fe}_2\text{O}_3$  NPs are increased with the amount of precursor.

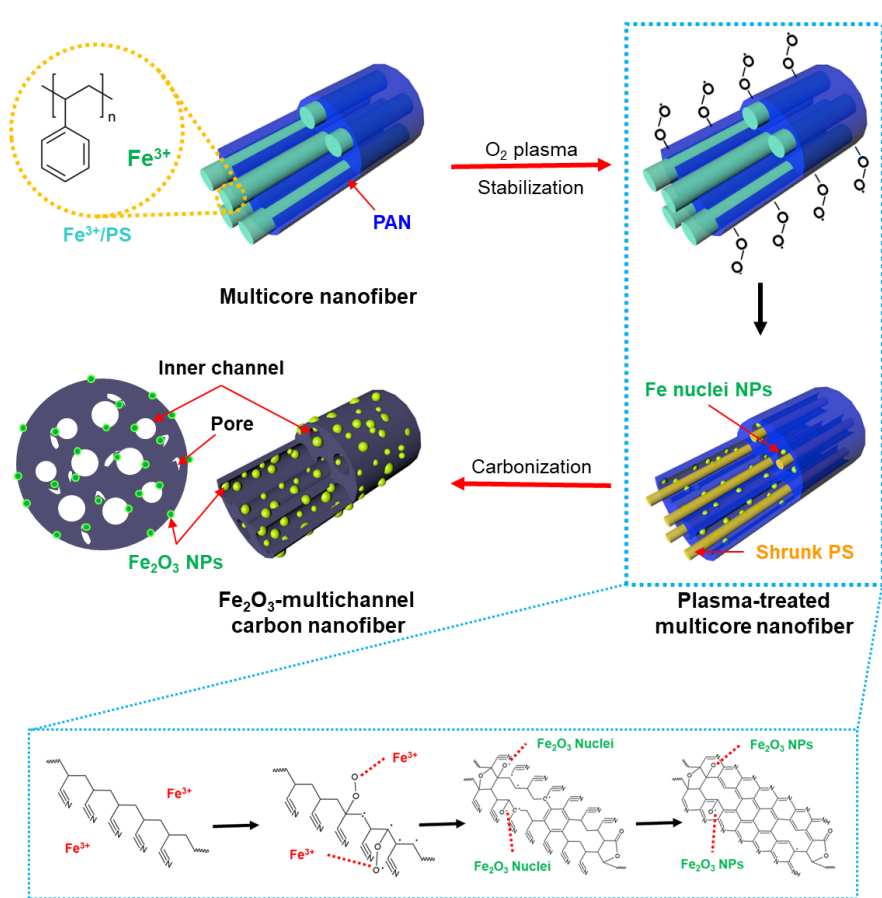


**Figure 58.** Illustration of the sequential synthesis of the Fe-mCNF (The inset: structural changes of the electrospun multicore nanofibers after each fabrication step.)

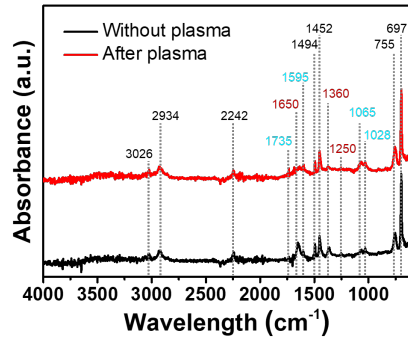


**Figure 59.** Fourier-transform infrared (FTIR) spectra of the electrospun multicore nanofibers (PAN/PS/FeCl<sub>3</sub>) before (black) and after (red) oxygen plasma treatment

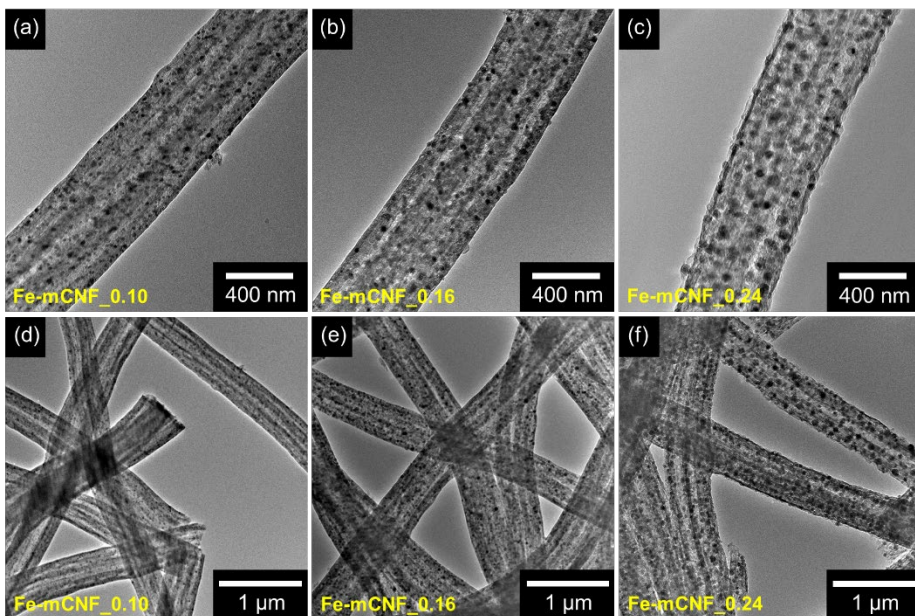


**Figure 60.** (a)~(c) High-magnified and (d)~(f) low-magnified TEM micrographs of Fe-mCNFs with various amount of Fe precursor (0.10, 0.16, 0.24 g) resulting various Fe<sub>2</sub>O<sub>3</sub> NPs size distribution.

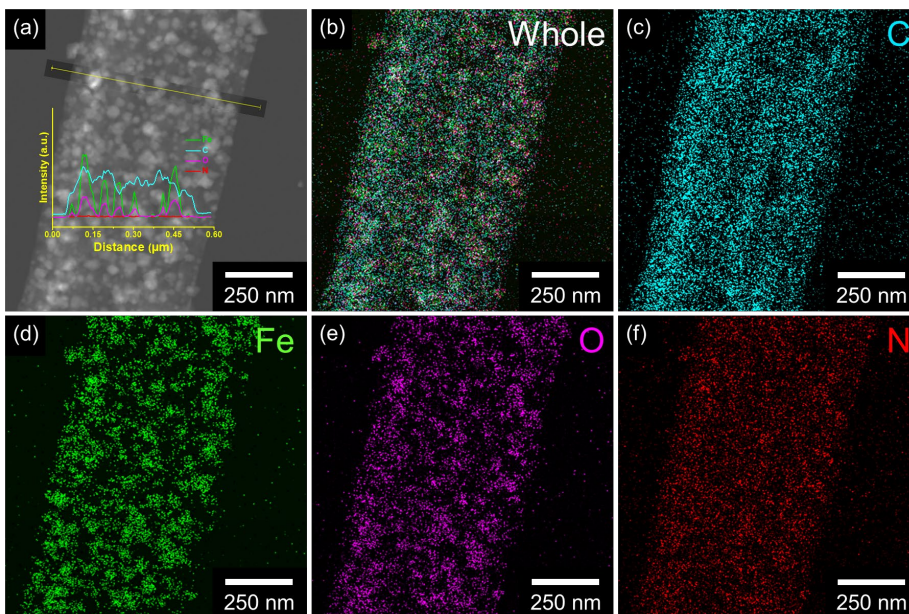


**Figure 61.** (a) Scanning TEM and energy dispersive spectroscopy (STEM-EDS) line mapping of the Fe-mCNF. (b)~(f) Electron energy-loss spectroscopy (EELS) dot mapping of the Fe-mCNF (cyan: C, green: Fe, magenta: O, red: N).

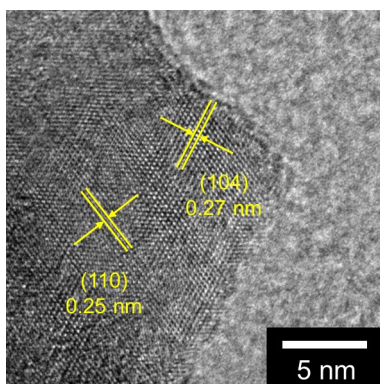


**Figure 62.** High-resolution TEM (HR-TEM) image of Fe<sub>2</sub>O<sub>3</sub> nanoparticle component in the carbon nanofiber structure

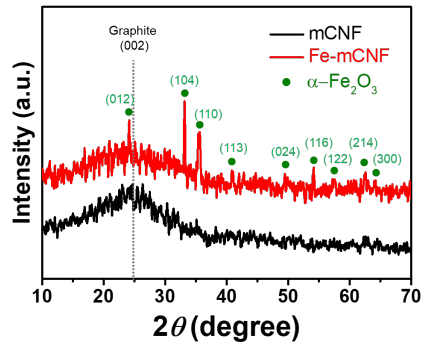


**Figure 63.** X-ray diffraction (XRD) spectra of mCNF (black) and Fe-mCNF (red).

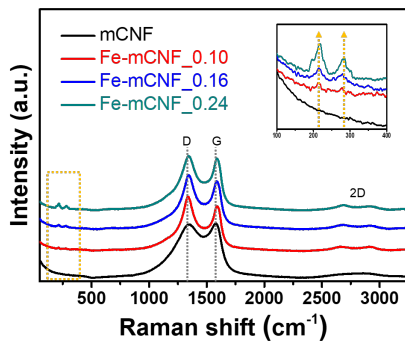
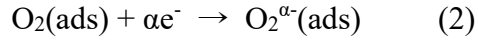
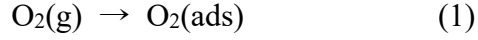


**Figure 64.** Raman spectra of (black) mCNF, (red) Fe-mCNF\_0.10, (blue) Fe-mCNF\_0.16, and (dark cyan) Fe-mCNF\_0.24.

### 3.2.2. Electrical measurement of Fe-mCNFs chemical sensor

To characterize the electrical properties of the Fe-mCNF-based sensor device, the composite nanotubes are immobilized on an interdigitated array (IDA) sensor electrode using a spin-coating method. **Figure 65a** displays linear current-voltage (I–V) curves of the various nanotubes for the voltage range from -0.1 to +0.1 V. A linearity of the I–V curves indicates that the nanofibers are uniformly immobilized on the sensor electrode with ohmic contact rather than Schottky barriers. Especially,  $dI/dV$  ( $=1/R$ ) value of the electrodes decreases with an increase in the population of the  $Fe_2O_3$  particles on the carbon surface due to high resistive metal oxide semiconductor particles enhancing the resistivity of the nanofiber composites. The uniformly dispersed  $Fe_2O_3$  particles on the carbon surface rapidly detect  $H_2S$  gas at room temperature by a chemical reaction between adsorbed oxygen species and  $H_2S$  gas (**Figure 66**). The sensing mechanism of the Fe-mCNF is illustrated as below. Initially, an electron depletion layer, composed of negatively charged adsorbing oxygen species ( $O^{2-}$ ,  $O^-$ , and  $O_2^-$ ), is formed on the  $Fe_2O_3$  particle surface after exposing the sensor electrode to air. Chemical reactions of adsorbed oxygen species are suggested as follows:



When the sensor electrode is exposed to H<sub>2</sub>S gas, the chemisorbed oxygen species on the Fe<sub>2</sub>O<sub>3</sub> particles oxidize H<sub>2</sub>S gas. In detail, the oxygen species disassemble H<sub>2</sub>S gas into H<sub>2</sub>O and SO<sub>2</sub> gases with transferring electrons to the Fe<sub>2</sub>O<sub>3</sub> and the carbon nanofiber structure. The oxidation reaction of H<sub>2</sub>S gas on the Fe<sub>2</sub>O<sub>3</sub> particles is described by



The resistance of the sensor electrode increases with electron transfer due to the decrease in a population of charge carriers (hole) through the recombination of the transferred electron and the hole in the carbon structure. Then, H<sub>2</sub>O and SO<sub>2</sub> gases from the oxidation of H<sub>2</sub>S are desorbed by exposure air contained gas (N<sub>2</sub> 80 vol% and O<sub>2</sub> 20 vol%) again. Consequently, the amount of chemisorbed oxygen species on the Fe<sub>2</sub>O<sub>3</sub> surface effects on the sensing ability of the

sensor electrode. Thus, a large population of the small-sized-Fe<sub>2</sub>O<sub>3</sub> provides an increase in specific surface area to H<sub>2</sub>S gas and efficient electron transfer to the carbon structure.

To investigate the sensing abilities of the Fe-mCNF-based sensor electrode, real-time responsive resistance changes are evaluated for different concentrations of H<sub>2</sub>S gas at room temperature. **Figure 65b** Upon various concentrations of H<sub>2</sub>S exposure, the Fe-mCNF-based electrodes display a rapid resistance increase. A minimum detection level (MDL) of each electrode exhibits as followed: 0.2 ppm for the Fe-mCNF\_0.24; 1 ppm for the Fe-mCNF\_0.16; 5 ppm for the Fe-mCNF\_0.10. **Figure 65c** presents the electrical responses of the sensor electrodes upon periodic disclosure to 5 ppm of H<sub>2</sub>S at room temperature. The Fe-mCNF-based electrodes show similar resistance changes with repetitive H<sub>2</sub>S sensing, without retardation of the response and recovery signals. The sensitivity (S) that is defined as the value of the normalized resistance change after 50 s gas exposure is determined with different H<sub>2</sub>S concentrations (**Figure 65d**). The linear tendency of the sensitivity of the Fe-mNCF electrodes is observed over a wide range of H<sub>2</sub>S concentration from 0.2 ppm to 100 ppm. In addition, **Figure 66** shows the stability of the sensor based on the

sensitivities of various Fe-mCNFs electrodes over a period of several weeks. After 3 weeks, the sensitivity decreased by 87 %, 88 %, and 89 % for sensors formed with Fe-mCNF\_0.10, Fe-mCNF\_0.16. and Fe-mCNF\_0.24, respectively. Therefore, the sensor electrode based on the Fe-mCNF exhibits reversible and reproducible responses to various concentrations of the target analyte (H<sub>2</sub>S).

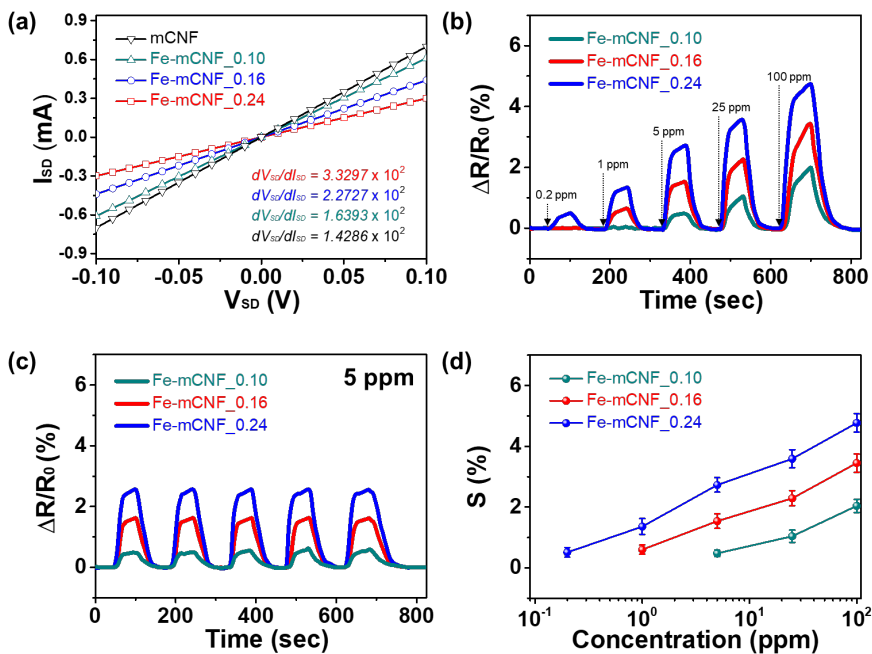


**Figure 65.** (a) Source-drain current-voltage ( $I_{SD}$ - $V_{SD}$ ) curves of sensors with mCNF, Fe-mCNF\_0.10, Ru-mCNF\_0.16, and Ru-mCNF\_0.24. Real-time responses of normalized resistance changes of the different Fe-mCNFs at room temperature on (b) sequential exposure to various H<sub>2</sub>S gas concentrations and (c) periodic exposure to 5 ppm of H<sub>2</sub>S gas (at a constant current:  $10^{-6}$  A). (d) Calibration curves of the different Fe-mCNFs as a function of various H<sub>2</sub>S gas concentrations. (dark cyan: Fe-mCNF\_0.10; red: Fe-mCNF\_0.16; blue: Fe-mCNF\_0.24)

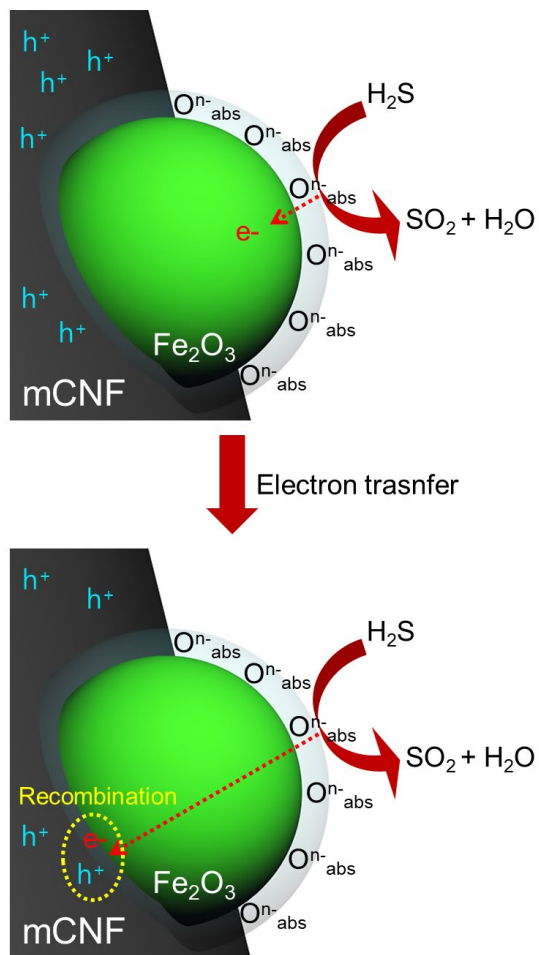


**Figure 66.** Schematic diagram of the H<sub>2</sub>S sensing mechanism of the Fe-mCNF sensor

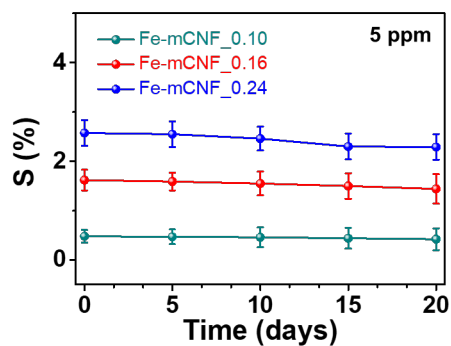


**Figure 67.** Stability of the Fe-mCNFs FET sensors measured over 20 days with intervals of 5 days. Dark cyan, red, and blue correspond to Fe-mCNF\_0.10, Fe-mCNF\_0.16, and Fe-mCNF\_0.24, respectively.

### **3.2.3. Wireless sensor measurement of Fe-mCNFs UHF-RFID wireless sensor**

In order to introduce the Fe-mCNF on the UHF-RFID tag system, the Fe-mCNF-based conductive paste (Fe-mCNF paste) was prepared by mixing the Fe-mCNF (80 wt%), super-P (10 wt%), and PVDF binder (10 wt%) in an *N*-methyl-2-pyrrolidone solvent. The prepared Fe-mCNF paste is applied to detect H<sub>2</sub>S gas in the RFID-based wireless sensing system. The wireless sensing system is composed of two parts that are the RFID-reader antenna-connected network analyzer (as a wireless signal reader) and the Fe-mCNF paste-printed RFID tag (as a sensor tag) (**Figure 68**). The wireless sensing system works using signal backscattering between the RFID-reader antenna and the sensor tag. In detail, the network analyzer emits an interrogation signal using the RFID-reader antenna to activate the sensor tag by means of the electromagnetic field between the RFID-reader antenna and the sensor tag. Then the wireless signal is reflected to the RFID reader antenna by sensor tag with slightly resistance change of the antenna pattern in the sensor tag when H<sub>2</sub>S gas exposed.

To apply an RFID tag as a sensor tag, the antenna pattern of the RFID tag is disconnected by perforating a conductive aluminum

pattern. As shown in **Figure 69a**, the disconnected passive RFID tag is reconnected by a screen-printing method using Fe-mCNF paste by using punched PET film as a printing pattern. The hole of the punched PET film is designed to the next position of the hole in the RFID tag. After that, the conductive paste reconfigures easily the disconnected antenna pattern, resulting in an RFID-based wireless sensor tag. In **Figure 69b**, the reconnected RFID sensor tag exhibits mechanical stability with different deformations due to enough viscous and good adhesion properties of the Fe-mCNF paste.

The sensor tag is applied to RFID-based wireless H<sub>2</sub>S gas sensing system. **Figure 70a** describes the change in the reflection of the radio frequency after a 2 min exposure to different concentrations of H<sub>2</sub>S gas at room temperature, at a distance of 10 cm. The reflection signal is defined by a network analyzer, which is expressed in terms of the power of the reflected wave (Re, dB) versus the frequency (MHz). Owing to the impedance matching between the antenna and the IC chip, the RFID sensor tag illustrates specific reflection curves. When the sensor tag is exposed to H<sub>2</sub>S gas, reflection amount and activated frequency of the sensor tag decrease owing to increase the resistance of the conductive paste-connected antenna pattern. The resistance

change causes an impedance mismatch between the antenna and the IC chip compared to them without the gas state. Then the RFID sensor tag decreases the radar cross-section resulting in decreasing the reflection and the operating frequency. The significant change of reflection and frequency shift is displayed as low as 0.2 ppm of H<sub>2</sub>S. In addition, the amount of reflection change is improved up to 100 ppm of the gas concentration.

**Figure 70b** shows normalized reflectance amount and operating frequency as a function of the H<sub>2</sub>S concentration. (The normalized reflectance is expressed as  $\Delta Re/Re_0 = (Re - Re_0)/Re_0$  where Re is the reflection at a 2 min H<sub>2</sub>S exposure and Re<sub>0</sub> is the reflectance at a beginning of the sensing.) According to the increasing concentrations, the change amount of the normalized reflectance increases, and the operating frequency decreases, indicating the saturation tendency of the sensor tag because of limited reaction sites of the Fe<sub>2</sub>O<sub>3</sub> component in the nanocomposite paste.

**Figure 71a** suggests the reflection changes with different remote distance (from 5 cm to 40 cm) between the sensor tag and the reader antenna. As the wireless distance increases, the change in reflectance reduces due to the decrease of the backscattering effect. There is no

significant reflection peak above 40 cm because of the absence of the backscattering effect.

Additionally, the flexibility of the sensor tag substrate (PET) and the conductive Fe-mCNF paste enables consistent sensing performance even when the sensor is deformed in several ways. The resonant reflection of the sensor tag represents a similar modulated wave with a deformation such as a twist and a bend at 5 ppm of the H<sub>2</sub>S gas (**Figure 71b**). The average reflectance change for various bending angles of the sensor tag is also presented in **Figure 71c**. There is no significant effect during repeated bending deformation (up to 500 cycles) owing to the uniformity of the sensor tag components on the substrate. Moreover, the sensor tag shows long-term reflectance stability for several weeks at a low concentration (0.2 ppm) of the gas due to the passive operating (without battery) working mechanism (**Figure 71d**). Conclusively, the proposed Fe-mCNF-based RFID sensor tag is promising for applications as a wearable or implantable wireless sensing system.

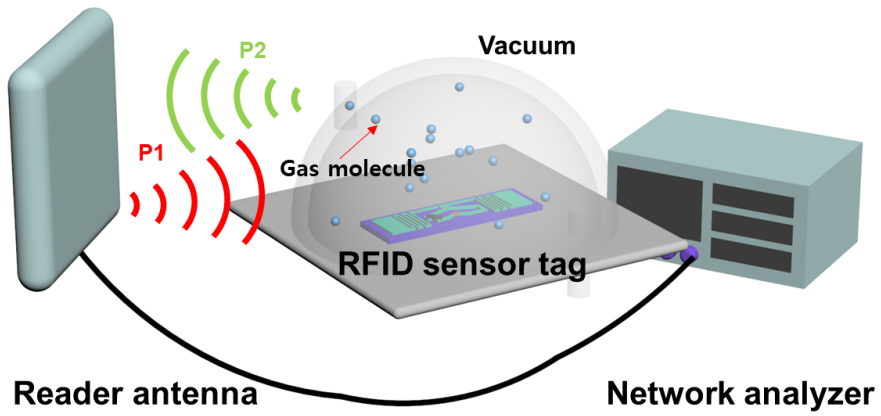


**Figure 68.** Schematic diagram of the RFID based-wireless sensor system consisting of reader antenna-connected network analyzer and a sensor tag

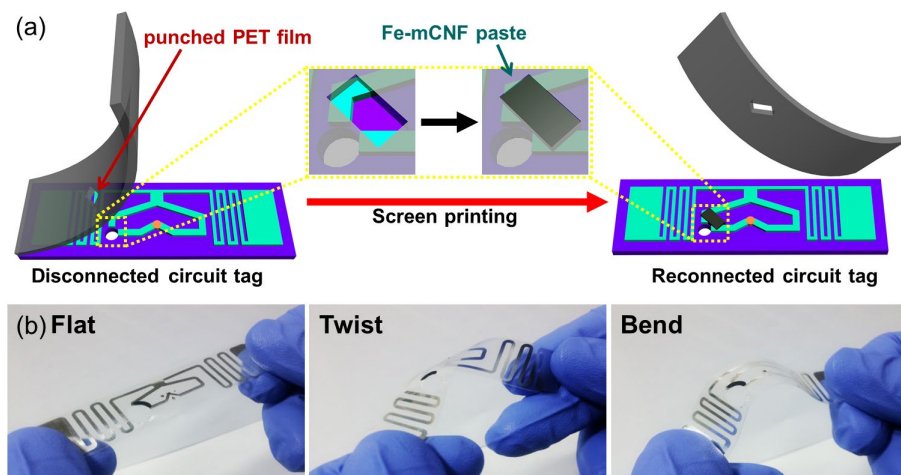


**Figure 69.** (a) Schematic diagram of the sequential fabrication process of the RFID sensor tag. (b) Photographs of the RFID-tag sensor under various deformations.

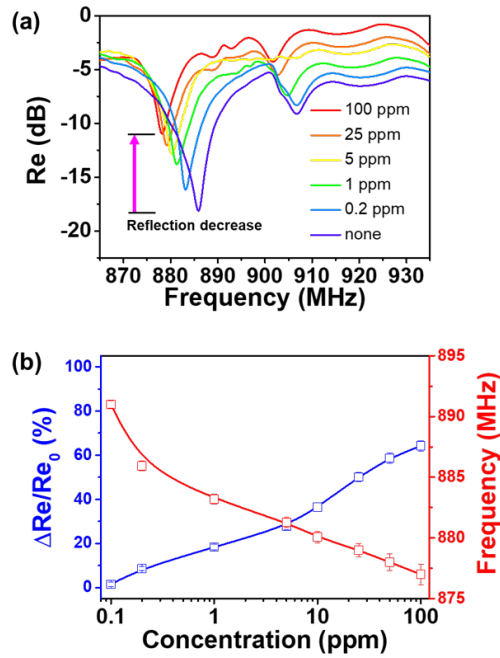


**Figure 70.** (a) Variation of reflectance characteristics of the Fe-mCNF-based wireless sensor with various  $H_2S$  gas concentrations (purple: without; blue: 0.5 ppm; green: 1 ppm, yellow: 5 ppm; orange: 25 ppm; red: 100 ppm). (b) Calibration of reflectance and phase shift curves as a function of the  $H_2S$  concentration.

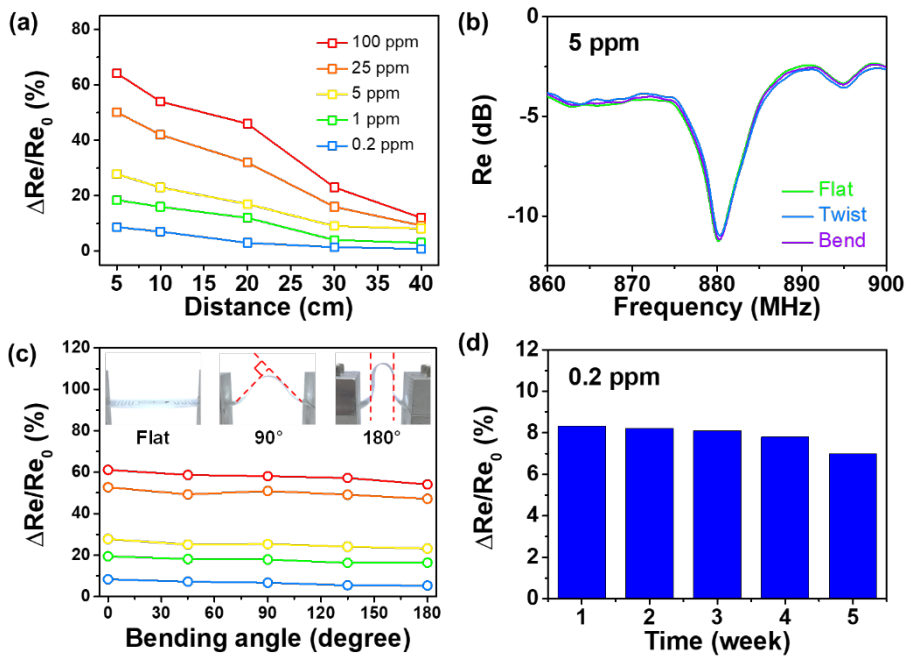


**Figure 71.** (a) Reflectance change of the wireless sensor system for different distances between RFID sensor tag and antenna with various  $H_2S$  gas concentrations. (b) Reflectance properties under different deformations at 5 ppm (flat, twist, and bend). (c) The normalized reflectance curves under various bending angles at 10 cm distance apart with different  $H_2S$  gas concentrations. (d) The long-term stability of the Fe-mCNF-based wireless sensor under 0.2 ppm  $H_2S$  gas.

## 4. Conclusion

In this dissertation, the multichannel carbon nanofibers-based various hybrid materials were fabricated including different kinds of materials such as bio-receptors, noble metal nanoparticles, and metal oxide nanoparticles by facile synthesis methods, and the synthesized nanomaterials suggested potential properties in the diverse sensor applications. The subtopics could be concluded in the viewpoint of each subtopic as follows:

1-1. The polyacrylonitrile (PAN) and poly(methyl methacrylate) (PMMA)-based multichannel carbon nanofibers (MCNFs) were fabricated using a single-nozzle co-electrospinning technique and conventional heat treatments. At first, for sensor applications, the as-prepared MCNFs were acid-treated with various time up to inner channel collapse to immobilize anti-bisphenol-A (BPA) aptamers on the surface of the MCNFs and to immobilize on the interdigitated array (IDA) electrode. The aptamer-modified MCNFs (A-MCNFs) FET sensors were well-fabricated through covalent bonding with aptamers and the electrodes. The maximized acid-treatment time of the MCNFs enhanced the amount of functionalized BPA-binding

aptamers, increasing its affinity to BPA. As a result, the A-MCNFs FET sensor exhibited a minimum detect level (MDL) of  $\sim 1$  fM to BPA. The optimized degree of functionalization and large specific surface area resulted in good sensitivity and selectivity for BPA. Owing to the immobilization of the aptamers via covalent bonding, the A-MCNFs FET sensors were stable and could be reused over a period of 4 weeks.

1-2. The anti-nesfatin-1 (NES1) antibody-modified MCNFs (Ab-MCNFs) FET sensor was fabricated in the same manner as the A-MCNFs FET sensor with the maximized oxidation time. As a control, PAN-based carbon nanofibers (CNFs) which have a similar diameter without multichannel were fabricated *via* electrospinning and thermal treatment, followed by fabrication of the antibody-modified CNFs (Ab-CNFs) FET sensor in the same way. As a result, in PBS solution, the Ab-MCNFs FET sensor exhibited good sensitivity (MDL = 0.1 fM), good selectivity, and wide range sensing coverage including real epilepsy patients NES1 concentrations (1.7~369 pM). Moreover, in the artificial saliva solution, the Ab-MCNFs FET sensor exhibited 10 fM MDL to NES1 and included sensing coverage of epilepsy patients NES1 concentrations.

2. The polyacrylonitrile (PAN) and polystyrene (PS)-based multichannel carbon nanofibers (mCNFs) were fabricated in the same way of MCNFs. The ruthenium nanoparticles-embedded mCNFs (Ru-mCNFs) were fabricated by electrospinning, followed by oxygen plasma method and heat treatment. The Ru-mCNFs-immobilized non-enzymatic FET sensors were fabricated using immobilization of the Ru-mCNFs on the electrode surface. The decorated Ru particles enhanced the oxidation amount of dopamine, increasing sensitivity to dopamine molecules. As a result, the Ru-mCNFs FET sensors exhibited 1 fM MDL to dopamine. Moreover, the Ru-mCNFs FET sensor displayed good selectivity to the dopamine molecules than other non-target molecules, as well as performed good stability (4 weeks) attributed to the covalent bonding of the immobilization process.

3-1. The iron oxide nanoparticles-embedded mCNFs (Fe-mCNFs) were fabricated by electrospinning, followed by oxygen plasma method and heat treatment, in a similar process as the fabrication of the Ru-mCNFs. The as-prepared Fe-mCNFs were used in gas sensor platform on IDA electrodes for detecting the hydrogen sulfide gas

with good sensitivity (MDL = 0.2 ppm) and good stability at room temperature.

3-2. Furthermore, the Fe-mCNF-based conductive paste was prepared with a PVDF binder and applied to the passive UHF-RFID tag for detecting the hydrogen sulfide gas in the wireless sensor system. The Fe-mCNF-based conductive paste was screen printed onto the exposed antenna pattern area in the disconnected RFID tag to reconnect the circuit. The wireless sensing system works using signal backscattering between the RFID-reader antenna and the sensor tag with a slight resistance change of the antenna pattern in the sensor tag when hydrogen sulfide gas exposed. The flexible sensor tag confirmed good sensitivity even if the deformation of the sensor tag in the wireless platform. Conclusively, the proposed Fe-mCNF-based RFID sensor tag is promising for applications as a wearable or implantable wireless sensing system.

In summary, various hybrid materials using electrospun PAN-based multichannel carbon nanofibers for bio and chemical sensor applications. First, multichannel carbon nanofibers were fabricated

through single-nozzle electrospinning and heat treatment. Bio-receptors-modified multichannel carbon nanofibers were prepared using the acid treatment and following catalytic reaction between carboxyl group and amine group of the bio-receptors. According to the bio-receptors, anti-bisphenol-A (BPA) aptamer was immobilized for detecting BPA and anti-nesfatin-1 (NES1) antibody was immobilized for detecting NES1. Second, noble metal (Ru) and metal oxide ( $\text{Fe}_2\text{O}_3$ ) nanoparticles-embedded multichannel carbon nanofibers were suggested by the facile method including oxygen plasma treatment before heat treatment. The as-prepared diverse hybrid multichannel carbon nanofibers exhibited ultrahigh ability in the bio/chemical sensor application due to its large active surface area originated from multichannel and porous structure. In addition, these prepared materials can be also utilized in other applications such as energy storage and biotherapy, etc.

## References

- [1] J. Jang, Conducting Polymer Nanomaterials and Their Applications. In *Emissive Materials Nanomaterials*, 2006; pp 189.
- [2] M. Lazzari, M. A. López-Quintela, *Advanced Materials* **2003**, *15* (19), 1583.
- [3] Q. Qiu Zhao, A. Boxman, U. Chowdhry, *Journal of Nanoparticle Research* **2003**, *5* (5), 567.
- [4] S. Das, J. Perez-Ramirez, J. Gong, N. Dewangan, K. Hidajat, B. C. Gates, S. Kawi, *Chem Soc Rev* **2020**, *49* (10), 2937.
- [5] L. Dai, Y. Wang, X. Zou, Z. Chen, H. Liu, Y. Ni, *Small* **2020**, *16* (13), e1906567.
- [6] M. A. Zeb Gul Sial, M. A. Ud Din, X. Wang, *Chem Soc Rev* **2018**, *47* (16), 6175.
- [7] Y. Chen, Z. Fan, Z. Zhang, W. Niu, C. Li, N. Yang, B. Chen, H. Zhang, *Chem Rev* **2018**, *118* (13), 6409.
- [8] O. S. Kwon, H. S. Song, T. H. Park, J. Jang, *Chem Rev* **2019**, *119* (1), 36.
- [9] V. V. Pokropivny, V. V. Skorokhod, *Physica E: Low-dimensional Systems and Nanostructures* **2008**, *40* (7), 2521.
- [10] C. Buzea, Pacheco, II, K. Robbie, *Biointerphases* **2007**, *2* (4), MR17.
- [11] Z. Kang, S. T. Lee, *Nanoscale* **2019**, *11* (41), 19214.
- [12] E. G. Barbagiovanni, D. J. Lockwood, P. J. Simpson, L. V. Goncharova, *Applied Physics Reviews* **2014**, *1* (1).
- [13] A. Agrawal, S. H. Cho, O. Zandi, S. Ghosh, R. W. Johns, D. J. Milliron, *Chem Rev* 2018, *118* (6), 3121.
- [14] J. S. Lee, D. H. Shin, J. Jang, *Energy & Environmental Science* **2015**, *8* (10), 3030.

- [15] G. Lee, J. Jang, *Journal of Power Sources* **2019**, *423*, 115.
- [16] J. Jun, J. S. Lee, D. H. Shin, J. Oh, W. Kim, W. Na, J. Jang, *Journal of Materials Chemistry A* **2017**, *5* (33), 17335.
- [17] K. Lee, J. Kim, H. Yu, J. W. Lee, C.-M. Yoon, S. K. Kim, J. Jang, *Journal of Materials Chemistry A* **2018**, *6* (47), 24560.
- [18] G. Lee, C. Lee, C. M. Yoon, M. Kim, J. Jang, *ACS Appl Mater Interfaces* **2017**, *9* (6), 5222.
- [19] J. Kim, G. Lee, K. Lee, H. Yu, J. W. Lee, C. M. Yoon, S. G. Kim, S. K. Kim, J. Jang, *Chem Commun (Camb)* **2020**, *56* (4), 535.
- [20] T. H. Le, Y. Kim, H. Yoon, *Polymers (Basel)* **2017**, *9* (4).
- [21] J. Jang, J. H. Oh, X. L. Li, *Journal of Materials Chemistry* **2004**, *14* (19).
- [22] R. Paul, F. Du, L. Dai, Y. Ding, Z. L. Wang, F. Wei, A. Roy, *Adv Mater* **2019**, *31* (13), e1805598.
- [23] G. Yang, L. Li, W. B. Lee, M. C. Ng, *Sci Technol Adv Mater* **2018**, *19* (1), 613.
- [24] H. D. Tran, D. Li, R. B. Kaner, *Advanced Materials* **2009**, *21* (14-15), 1487.
- [25] Q. Wei, F. Xiong, S. Tan, L. Huang, E. H. Lan, B. Dunn, L. Mai, *Adv Mater* **2017**, *29* (20).
- [26] M. Ge, C. Cao, J. Huang, S. Li, Z. Chen, K.-Q. Zhang, S. S. Al-Deyab, Y. Lai, *Journal of Materials Chemistry A* **2016**, *4* (18), 6772.
- [27] Q. Xu, W. Li, L. Ding, W. Yang, H. Xiao, W. J. Ong, *Nanoscale* **2019**, *11* (4), 1475.
- [28] S. Peng, G. Jin, L. Li, K. Li, M. Srinivasan, S. Ramakrishna, J. Chen, *Chem Soc Rev* **2016**, *45* (5), 1225.
- [29] F. Zhou, H. N. Tien, Q. Dong, W. L. Xu, B. Sengupta, S. Zha, J. Jiang, D. Behera, S. Li, M. Yu, *Journal of Materials Chemistry A* **2020**, *8* (3), 1084.

- [30] T. Zhai, X. Fang, L. Li, Y. Bando, D. Golberg, *Nanoscale* **2010**, 2 (2), 168.
- [31] L. Wang, G. Yang, S. Peng, J. Wang, W. Yan, S. Ramakrishna, *Energy Storage Materials* **2020**, 25, 443.
- [32] A. Ebina, S. Hossain, H. Horihata, S. Ozaki, S. Kato, T. Kawawaki, Y. Negishi, *Nanomaterials (Basel)* **2020**, 10 (6).
- [33] I. Zucker, S. M. Hashmi, J. Yang, Y. He, L. D. Pfefferle, M. Elimelech, *Langmuir* **2019**, 35 (43), 13958.
- [34] C. L. Hsu, S. J. Chang, *Small* **2014**, 10 (22), 4562.
- [35] F. X. Xiao, J. Miao, H. B. Tao, S. F. Hung, H. Y. Wang, H. B. Yang, J. Chen, R. Chen, B. Liu, *Small* **2015**, 11 (18), 2115.
- [36] Z. Yin, Q. Zheng, *Advanced Energy Materials* **2012**, 2 (2), 179.
- [37] J. Song, M. Kim, H. Lee, *Polymers (Basel)* **2020**, 12 (6).
- [38] X. Yan, M. Yu, S. Ramakrishna, S. J. Russell, Y. Z. Long, *Nanoscale* **2019**, 11 (41), 19166.
- [39] L. Shang, Y. Yu, Y. Liu, Z. Chen, T. Kong, Y. Zhao, *ACS Nano* **2019**, 13 (3), 2749.
- [40] D. Li, Y. Xia, *Advanced Materials* **2004**, 16 (14), 1151.
- [41] S. R. Merritt, A. A. Exner, Z. Lee, H. A. von Recum, *Advanced Engineering Materials* **2012**, 14 (5), B266.
- [42] T. Kyotani, *Carbon* **2000**, 38 (2), 269.
- [43] J. Zhang, Z. Li, X. W. D. Lou, *Angew Chem Int Ed Engl* **2017**, 56 (45), 14107.
- [44] S. H. Yoo, H.-I. Joh, S. Lee, *Applied Surface Science* **2017**, 402, 456.
- [45] Z. Wang, S. Wu, J. Wang, A. Yu, G. Wei, *Nanomaterials (Basel)* **2019**, 9 (7).
- [46] H. Zhang, W. Zhou, T. Chen, B. Y. Guan, Z. Li, X. W. Lou, *Energy & Environmental Science* **2018**, 11 (8), 1980.
- [47] J. Yoon, H. S. Yang, B. S. Lee, W. R. Yu, *Adv Mater* **2018**, 30

- (42), e1704765.
- [48] Y. J. Jeong, W. T. Koo, J. S. Jang, D. H. Kim, M. H. Kim, I. D. Kim, *ACS Appl Mater Interfaces* **2018**, *10* (2), 2016.
- [49] Z.-H. Huang, Z. Yang, F. Kang, M. Inagaki, *Journal of Materials Chemistry A* **2017**, *5* (2), 470.
- [50] J. Wu, N. Wang, Y. Zhao, L. Jiang, *Journal of Materials Chemistry A* **2013**, *1* (25).
- [51] S. K. Nataraj, K. S. Yang, T. M. Aminabhavi, *Progress in Polymer Science* **2012**, *37* (3), 487.
- [52] M. Inagaki, Y. Yang, F. Kang, *Adv Mater* **2012**, *24* (19), 2547.
- [53] S. Peng, L. Li, J. Kong Yoong Lee, L. Tian, M. Srinivasan, S. Adams, S. Ramakrishna, *Nano Energy* **2016**, *22*, 361.
- [54] L. Li, S. Peng, J. K. Y. Lee, D. Ji, M. Srinivasan, S. Ramakrishna, *Nano Energy* **2017**, *39*, 111.
- [55] Z. Zhou, T. Liu, A. U. Khan, G. Liu, *Science Advances* **2019**, *5* (2), eaau6852.
- [56] Y. Xue, J. Liu, J. Liang, *Polymer Degradation and Stability* **2013**, *98* (1), 219.
- [57] Y. Xue, J. Liu, F. Lian, J. Liang, *Polymer Degradation and Stability* **2013**, *98* (11), 2259.
- [58] N. Hameed, J. Sharp, S. Nunna, C. Creighton, K. Magniez, P. Jyotishkumar, N. V. Salim, B. Fox, *Polymer Degradation and Stability* **2016**, *128*, 39.
- [59] J. Zhao, J. Zhang, T. Zhou, X. Liu, Q. Yuan, A. Zhang, *RSC Advances* **2016**, *6* (6), 4397.
- [60] N. Yusof, A. F. Ismail, *Journal of Analytical and Applied Pyrolysis* **2012**, *93*, 1.
- [61] E. Fitzer, W. Frohs, M. Heine, *Carbon* **1986**, *24* (4), 387.
- [62] T.-H. Le, H. Yoon, *Carbon* **2019**, *152*, 796.
- [63] Y. Yang, T. Le, F. Kang, M. Inagaki, *Carbon* **2017**, *111*, 546.

- [64] S. Bhojate, P. K. Kahol, B. Sapkota, S. R. Mishra, F. Perez, R. K. Gupta, *Surface and Coatings Technology* **2018**, *345*, 113.
- [65] X. Sun, W. Li, X. Zhong, Y. Yu, *Energy Storage Materials* **2017**, *9*, 112.
- [66] Y. E. Miao, Y. Huang, L. Zhang, W. Fan, F. Lai, T. Liu, *Nanoscale* **2015**, *7* (25), 11093.
- [67] J. Zhang, Z. Li, X. W. Lou, *Angewandte Chemie International Edition* **2017**, *56* (45), 14107.
- [68] Y. Pan, X. Cheng, Y. Huang, L. Gong, H. Zhang, *ACS Appl Mater Interfaces* **2017**, *9* (41), 35820.
- [69] J. Liu, Z. Xiong, S. Wang, W. Cai, J. Yang, H. Zhang, *Electrochimica Acta* **2016**, *210*, 171.
- [70] Z. Li, J. T. Zhang, Y. M. Chen, J. Li, X. W. Lou, *Nat Commun* **2015**, *6*, 8850.
- [71] N. C. Abeykoon, J. S. Bonso, J. P. Ferraris, *RSC Advances* **2015**, *5* (26), 19865.
- [72] K. Wei, K.-O. Kim, K.-H. Song, C.-Y. Kang, J. S. Lee, M. Gopiraman, I.-S. Kim, *Journal of Materials Science & Technology* **2017**, *33* (5), 424.
- [73] X. Sun, C. Wang, Y. Gong, L. Gu, Q. Chen, Y. Yu, *Small* **2018**, *14* (35), e1802218.
- [74] D. Bikiaris, A. Vassiliou, K. Chrissafis, K. M. Paraskevopoulos, A. Jannakoudakis, A. Docoslis, *Polymer Degradation and Stability* **2008**, *93* (5), 952.
- [75] L. Liang, W. Xie, S. Fang, F. He, B. Yin, C. Tlili, D. Wang, S. Qiu, Q. Li, *Journal of Materials Chemistry C* **2017**, *5* (44), 11339.
- [76] S.-W. Lee, H.-Y. Lee, S.-Y. Jang, S. Jo, H.-S. Lee, W.-H. Choe, S. Lee, *Carbon* **2013**, *55*, 361.
- [77] S. H. Mortazavi, S. Pilehvar, M. Ghoranneviss, M. T.

- Hosseinnejad, L. Dejam, *Molecular Crystals and Liquid Crystals* **2014**, 592 (1), 115.
- [78] S. Hamideh Mortazavi, S. Pilehvar, M. Ghoranneviss, M. T. Hosseinnejad, S. Zargham, A. A. Mirarefi, A. Y. Mirarefi, *Applied Physics A* **2013**, 113 (3), 703.
- [79] H. K. Shin, M. Park, H.-Y. Kim, S.-J. Park, *Carbon letters* **2015**, 16 (1), 11.
- [80] S.-Y. Kim, S. Lee, S. Park, S. M. Jo, H.-S. Lee, H.-I. Joh, *Carbon* **2015**, 94, 412.
- [81] S. Park, S. H. Yoo, H. R. Kang, S. M. Jo, H. I. Joh, S. Lee, *Sci Rep* **2016**, 6, 27330.
- [82] L. Peng, Z. Fang, Y. Zhu, C. Yan, G. Yu, *Advanced Energy Materials* **2018**, 8 (9).
- [83] Q. Yun, Q. Lu, X. Zhang, C. Tan, H. Zhang, *Angewandte Chemie - International Edition* 2018, 57 (3), 626.
- [84] R. S. Geonmonond, A. Silva, P. H. C. Camargo, *An Acad Bras Cienc* **2018**, 90 (1 Suppl 1), 719.
- [85] C. Wang, X. Gao, Z. Chen, Y. Chen, H. Chen, *Polymers* **2017**, 9 (12).
- [86] S. Hong, H. Lee, J. Yeo, S. H. Ko, *Nano Today* **2016**, 11 (5), 547.
- [87] X. Wang, J. Feng, Y. Bai, Q. Zhang, Y. Yin, *Chemical Reviews* **2016**, 116 (18), 10983.
- [88] T. Wang, H. K. Kim, Y. Liu, W. Li, J. T. Griffiths, Y. Wu, S. Laha, K. D. Fong, F. Podjaski, C. Yun, R. V. Kumar, B. V. Lotsch, A. K. Cheetham, S. K. Smoukov, *Journal of the American Chemical Society* **2018**, 140 (19), 6130.
- [89] C. Neumann, D. Kaiser, M. J. Mohn, M. Fuser, N. E. Weber, O. Reimer, A. Golzhauser, T. Weimann, A. Terfort, U. Kaiser, A. Turchanin, *ACS Nano* **2019**, 13 (6), 7310.
- [90] P. Colson, C. Henrist, R. Cloots, *Journal of Nanomaterials* **2013**,

2013.

- [91] L. Lee, B. Kang, S. Han, H. E. Kim, M. D. Lee, J. H. Bang, *Small* **2018**, *14* (25).
- [92] S. Kim, J. M. Kim, J. E. Park, J. M. Nam, *Advanced Materials* **2018**, *30* (42).
- [93] S. Kundu, A. Patra, *Chemical Reviews* **2017**, *117* (2), 712.
- [94] D. W. Hatchett, M. Josowicz, *Chemical Reviews* **2008**, *108* (2), 746.
- [95] S. J. Park, C. S. Park, H. Yoon, *Polymers* **2017**, *9* (5).
- [96] L. S. K. Achary, A. Kumar, B. Barik, P. S. Nayak, N. Tripathy, J. P. Kar, P. Dash, *Sensors and Actuators, B: Chemical* **2018**, *272*, 100.
- [97] R. S. Andre, R. C. Sanfelice, A. Pavinatto, L. H. C. Mattoso, D. S. Correa, *Materials and Design* **2018**, *156*, 154.
- [98] N. L. W. Septiani, Y. V. Kaneti, B. Yulianto, Nugraha, H. K. Dipojono, T. Takei, J. You, Y. Yamauchi, *Sensors and Actuators, B: Chemical* **2018**, *261*, 241.
- [99] Q. Shi, C. Zhu, D. Du, Y. Lin, *Chemical Society Reviews* **2019**, *48* (12), 3181.
- [100] H. Zhang, Y. Liu, H. Wu, W. Zhou, Z. Kou, S. J. Pennycook, J. Xie, C. Guan, J. Wang, *Journal of Materials Chemistry A* **2018**, *6* (41), 20214.
- [101] J. Qu, D. Chen, N. Li, Q. Xu, H. Li, J. He, J. Lu, *Small* **2018**, *14* (16).
- [102] W. Li, Y. Liu, M. Wu, X. Feng, S. A. T. Redfern, Y. Shang, X. Yong, T. Feng, K. Wu, Z. Liu, B. Li, Z. Chen, J. S. Tse, S. Lu, B. Yang, *Advanced Materials* **2018**, *30* (31).
- [103] Z. Bai, W. Dong, Y. Ren, C. Zhang, Q. Chen, *Langmuir* **2018**, *34* (6), 2235.
- [104] Y. Liang, Y. Li, H. Wang, J. Zhou, J. Wang, T. Regier, H. Dai,

- Nature Materials* **2011**, *10* (10), 780.
- [105] Y. Zhao, L. P. Wang, M. T. Sougrati, Z. Feng, Y. Leconte, A. Fisher, M. Srinivasan, Z. Xu, *Advanced Energy Materials* **2017**, *7* (9).
- [106] Z. Xiang, Y. Song, J. Xiong, Z. Pan, X. Wang, L. Liu, R. Liu, H. Yang, W. Lu, *Carbon* **2019**, *142*, 20.
- [107] X. F. Lu, L. F. Gu, J. W. Wang, J. X. Wu, P. Q. Liao, G. R. Li, *Advanced Materials* **2017**, *29* (3).
- [108] W. H. Low, P. S. Khiew, S. S. Lim, C. W. Siong, E. R. Ezeigwe, *Journal of Alloys and Compounds* **2019**, *775*, 1324.
- [109] M. S. Javed, N. Shaheen, S. Hussain, J. Li, S. S. A. Shah, Y. Abbas, M. A. Ahmad, R. Raza, W. Mai, *Journal of Materials Chemistry A* **2019**, *7* (3), 946.
- [110] J. Zhang, Z. Yang, J. Qiu, H. W. Lee, *Journal of Materials Chemistry A* **2016**, *4* (16), 5802.
- [111] H. Yoon, J. Jang, *Advanced Functional Materials* **2009**, *19* (10), 1567.
- [112] J. Zhou, Q. Liu, W. Feng, Y. Sun, F. Li, *Chemical Reviews* **2015**, *115* (1), 395.
- [113] N. P. Dasgupta, J. Sun, C. Liu, S. Brittman, S. C. Andrews, J. Lim, H. Gao, R. Yan, P. Yang, *Advanced Materials* **2014**, *26* (14), 2137.
- [114] M. Amjadi, K. U. Kyung, I. Park, M. Sitti, *Advanced Functional Materials* **2016**, *26* (11), 1678.
- [115] K. Zhou, Y. Zhao, X. Sun, Z. Yuan, G. Zheng, K. Dai, L. Mi, C. Pan, C. Liu, C. Shen, *Nano Energy* **2020**, *70*, 104546.
- [116] L. Wang, L. Wang, Y. Zhang, J. Pan, S. Li, X. Sun, B. Zhang, H. Peng, *Advanced Functional Materials* **2018**, *28* (42), 1804456.
- [117] M. L. Hammock, A. Chortos, B. C. K. Tee, J. B. H. Tok, Z. Bao, *Advanced Materials* **2013**, *25* (42), 5997.

- [118] K. Chatterjee, S. Sarkar, K. Jagajjanani Rao, S. Paria, *Advances in Colloid and Interface Science* **2014**, *209*, 8.
- [119] C. He, D. Liu, W. Lin, *Chemical Reviews* **2015**, *115* (19), 11079.
- [120] Y. Zhou, Y. Fang, R. P. Ramasamy, *Sensors (Basel)* **2019**, *19* (2).
- [121] J. Wang, *Chemical Reviews* **2008**, *108* (2), 814.
- [122] E. Katz, I. Willner, *Angewandte Chemie - International Edition* **2004**, *43* (45), 6042.
- [123] T. Kuila, S. Bose, P. Khanra, A. K. Mishra, N. H. Kim, J. H. Lee, *Biosensors and Bioelectronics* **2011**, *26* (12), 4637.
- [124] J. Homola, *Chemical Reviews* **2008**, *108* (2), 462.
- [125] S. J. Park, H. S. Song, O. S. Kwon, J. H. Chung, S. H. Lee, J. H. An, S. R. Ahn, J. E. Lee, H. Yoon, T. H. Park, J. Jang, *Sci Rep* **2014**, *4*, 4342.
- [126] O. S. Kwon, S. H. Lee, S. J. Park, J. H. An, H. S. Song, T. Kim, J. H. Oh, J. Bae, H. Yoon, T. H. Park, J. Jang, *Adv Mater* **2013**, *25* (30), 4177.
- [127] D. H. Shin, W. Kim, J. Jun, J. S. Lee, J. H. Kim, J. Jang, *Sensors and Actuators B: Chemical* **2018**, *264*, 216.
- [128] W. Kim, J. S. Lee, D. H. Shin, J. Jang, *J Mater Chem B* **2018**, *6* (8), 1272.
- [129] K. H. Cho, D. H. Shin, J. Oh, J. H. An, J. S. Lee, J. Jang, *ACS Appl Mater Interfaces* **2018**, *10* (34), 28412.
- [130] M. Kaisti, *Biosensors and Bioelectronics* **2017**, *98*, 437.
- [131] E. Den Hond, H. Tournaye, P. De Sutter, W. Ombelet, W. Baeyens, A. Covaci, B. Cox, T. S. Nawrot, N. Van Larebeke, T. D'Hooghe, *Environ. Int.* **2015**, *84*, 154.
- [132] J. E. Schneider, J. M. Brozek, E. Keen-Rhinehart, *Horm. Behav.* **2014**, *66*, 104.
- [133] V. Futran Fuhrman, A. Tal, S. Arnon, *J. Hazard. Mater.* **2015**, *286*, 589.

- [134] S. M. Rappaport, M. T. Smith, *Science* **2010**, *330*, 460.
- [135] C. S. Rosenfeld, *Front. Neurosci.* **2015**, *9*.
- [136] X. Huo, D. Chen, Y. He, W. Zhu, W. Zhou, J. Zhang, *Int. J. Environ. Res. Public Health* **2015**, *12*, 11101.
- [137] L. H. Duntas, *Endocrine* **2015**, *48*, 53.
- [138] V. Mustieles, R. Perez-Lobato, N. Olea, M. F. Fernandez, *Neurotoxicology* **2015**, *49*, 174.
- [139] L. N. Vandenberg, R. Hauser, M. Marcus, N. Olea, W. V. Welshons, *Reprod. Toxicol.* **2007**, *24*, 139.
- [140] M. Khatami, C. J. Baglolle, J. Sun, S. Harris, E. Y. Moon, F. Al-Mulla, R. Al-Temaimi, D. Brown, A. Colacci, C. Mondello, J. Raju, E. Ryan, J. Woodrick, I. Scovassi, N. Singh, M. Vaccari, R. Roy, S. Forte, L. Memeo, H. K. Salem, A. Amedei, R. A. Hamid, L. Lowe, T. Guarnieri, W. H. Bisson, P. A. Thompson, *Carcinogenesis* **2015**, *36*, S232.
- [141] R. Rezg, S. El-Fazaa, N. Gharbi, B. Mornagui, *Environ. Int.* **2014**, *64*, 83.
- [142] F. Rancière, J. G. Lyons, V. H. Y. Loh, J. Botton, T. Galloway, T. Wang, J. E. Shaw, D. J. Magliano, *Environ. Health* **2015**, *14*.
- [143] S. J. Oppeneer, K. Robien, *Public Health Nutr.* **2015**, *18*, 1847.
- [144] P. Mirmira, C. Evans-Molina, *Transl. Res.* **2014**, *164*, 13.
- [145] T. Geens, D. Aerts, C. Berthot, J. P. Bourguignon, L. Goeyens, P. Lecomte, G. Maghuin-Rogister, A. M. Pironnet, L. Pussemier, M. L. Scippo, J. Van Loco, A. Covaci, *Food Chem. Toxicol.* **2012**, *50*, 3725.
- [146] J. Mathieu-Denoncourt, S. J. Wallace, S. R. de Solla, V. S. Langlois, *Gen. Comp. Endocrinol.* **2015**, *219*, 74.
- [147] B. S. Rubin, *J. Steroid Biochem. Mol. Biol.* **2011**, *127*, 27.
- [148] Commission Directive 2004/19/EC of 1 March 2004 amending Directive 2002/72/EC relating to plastic materials and articles

- intended to come into contact with foodstuffs. *Off. J. Eur. Communities* **2004**, L71, 8.
- [149] European Food Safety Authority (EFSA). Opinion of the Scientific Panel on food additives, flavourings, processing aids and materials in contact with food (AFC) related to 2,2-bis(4-hydroxyphenyl)-propane. *EFSA J.* **2006**, 428, 1.
- [150] X. Li, A. A. Franke, *Anal. Bioanal. Chem.* **2015**, 407, 3869.
- [151] A. Ballesteros-Gomez, S. Rubio, D. Perez-Bendito, *J. Chromatogr. A* **2009**, 1216, 449.
- [152] A. L. Capriotti, C. Cavaliere, V. Colapicchioni, S. Piovesana, R. Samperi, A. Laganà, *J. Chromatogr. A* **2013**, 1313, 62.
- [153] M. Jo, J. Y. Ahn, J. Lee, S. Lee, S. W. Hong, J. W. Yoo, J. Kang, P. Dua, D. K. Lee, S. Hong, S. Kim, *Oligonucleotides* **2011**, 21, 85.
- [154] A. G. Asimakopoulos, N. S. Thomaidis, M. A. Koupparis, *Toxicol. Lett.* **2012**, 210, 141.
- [155] S. Ramgopal, S. Thome-Souza, M. Jackson, N. E. Kadish, I. Sánchez Fernández, J. Klehm, W. Bosl, C. Reinsberger, S. Schachter, T. Loddenkemper, *Epilepsy and Behavior* **2014**, 37, 291.
- [156] W. Löscher, *Progress in Neurobiology* **1997**, 53 (2), 239.
- [157] R. D. Nass, R. Sassen, C. E. Elger, R. Surges, *Seizure* **2017**, 47, 51.
- [158] E. Clynen, A. Swijsen, M. Raijmakers, G. Hoogland, J. M. Rigo, *Molecular Neurobiology* **2014**, 50 (2), 626.
- [159] E. Oribe, R. Amini, E. Nissenbaum, B. Boal, *Neurology* **1996**, 47 (1), 60.
- [160] H. Shimizu, S. Oh-I, S. Okada, M. Mori, *Endocrine Journal* **2009**, 56 (4), 537.
- [161] A. Stengel, M. Goebel, L. Wang, Y. Taché, *Peptides* **2010**, 31

(2), 357.

- [162] L. Lepen, B. Lorber, *Zdravniski Vestnik* **2013**, 82 (7), 466.
- [163] S. Aydin, E. Dag, Y. Ozkan, O. Arslan, G. Koc, S. Bek, S. Kirbas, T. Kasikci, D. Abasli, Z. Gokcil, Z. Odabasi, Z. Catak, *Peptides* **2011**, 32 (6), 1276.
- [164] D. K. Chen, Y. T. So, R. S. Fisher, *Neurology* **2005**, 65 (5), 668.
- [165] I. Lušic, I. Pintaric, I. Hozo, L. Boic, V. Čapkun, *Seizure* **1999**, 8 (4), 218.
- [166] S. Aydin, E. Dag, Y. Ozkan, F. Erman, A. F. Dagli, N. Kilic, I. Sahin, F. Karatas, T. Yoldas, A. O. Barim, Y. Kendir, *Mol Cell Biochem* **2009**, 328 (1-2), 49.
- [167] T. C. Sudhof, *Neuron* 2013, 80, 675.
- [168] D. L. Robinson, B. J. Venton, M. L. A. V. Heien, R. M. Wightman, *Clin. Chem.* **2003**, 49, 1763.
- [169] K. Jackowska, P. Krysinski, *Anal. Bioanal. Chem.* **2013**, 405, 3753.
- [170] A. Galvan, T. Wichmann, *Clin. Neurophysiol.* **2008**, 119, 1459.
- [171] J. W. Dalley, J. P. Roiser, *Neuroscience* **2012**, 215, 42.
- [172] E. Baldrich, R. Gomez, G. Gabriel, F. X. Munoz, *Biosens. Bioelectron.* **2011**, 26, 1876.
- [173] M. Marinelli, J. E. Mccutcheon, *Neuroscience* **2014**, 28, 176.
- [174] J-M. Beaulieu, *J. Psychiatry Neurosci.* **2012**, 37, 7.
- [175] N. Ye, T. Gao, J. Li, *Anal. Methods* **2014**, 6, 7518.
- [176] B-R. Li, Y-J. Hsieh, Y-X. Chen, Y-T. Chung, C-Y. Pan, Y-T. Chen, *J. Am. Chem. Soc.* **2013**, 135, 16034.
- [177] T. J. Castilho, A. D. P. T. Sotomayor, L. T. Kubota, *J. Pharm. Biomed. Anal.* **2005**, 37, 785.
- [178] L. Stoica, A. Lindgren-Sjolander, T. Ruzgas, L. Gorton, *Anal. Chem.* **2004**, 76, 4690.

- [179] K. Sankarasubramanian, P. Soundarrajan, T. Logu, K. Sethuraman, K. Ramamurthi, *New Journal of Chemistry* **2018**, *42* (2), 1457.
- [180] T. Yang, Y. Liu, H. Wang, Y. Duo, B. Zhang, Y. Ge, H. Zhang, W. Chen, *Journal of Materials Chemistry C* **2020**, *8* (22), 7272.
- [181] N. Nasiri, C. Clarke, *Sensors (Switzerland)* **2019**, *19* (3).
- [182] J. Dai, O. Ogbeide, N. Macadam, Q. Sun, W. Yu, Y. Li, B. L. Su, T. Hasan, X. Huang, W. Huang, *Chem Soc Rev* **2020**, *49* (6), 1756.
- [183] T. C. Wu, A. De Luca, Q. Zhong, X. Zhu, O. Ogbeide, D. S. Um, G. Hu, T. Albrow-Owen, F. Udrea, T. Hasan, *npj 2D Materials and Applications* **2019**, *3* (1).
- [184] G. Wang, X. Zhou, J. Qin, Y. Liang, B. Feng, Y. Deng, Y. Zhao, J. Wei, *ACS Applied Materials and Interfaces* **2019**, *11* (38), 35060.
- [185] Y. Zhao, J.-G. Song, G. H. Ryu, K. Y. Ko, W. J. Woo, Y. Kim, D. Kim, J. H. Lim, S. Lee, Z. Lee, J. Park, H. Kim, *Nanoscale* **2018**, *10*, 9338.
- [186] Z. Hua, C. Tian, Z. Qiu, Y. Li, X. Tian, M. Wang, E. Li, *Sens. Actuators, B* **2018**, *259*, 250.
- [187] J. Shu, Z. Qiu, S. Lv, K. Zhang, D. Tang, *Anal. Chem.* **2017**, *89*, 11135.
- [188] K. Tian, X.-X. Wang, Z.-Y. Yu, H.-Y. Li, X. Guo, *ACS Appl. Mater. Interfaces* **2017**, *9*, 29669.
- [189] H. Wu, Z. Chen, J. Zhang, F. Wu, C. He, B. Wang, Y. Wu, Z. Ren, *J. Mater. Chem. A* **2016**, *4*, 1096.
- [190] A. F. S. Abu-Hani, Y. E. Greish, S. T. Mahmoud, F. Awwad and A. I. Ayesh, *Sens. Actuators, B* **2017**, *253*, 677.
- [191] A. B. Bodade, A. M. Bende, G. N. Chaudhari, *Vacuum* **2008**, *82*, 588.

- [192] R. S. Mackay, *Nature* **1964**, *204*, 355.
- [193] H. Messer, A. Zinevich, P. Alpert, *Science* **2006**, *312*, 713.
- [194] R. A. M. Receveur, F. W. Lindemans, N. F. d. Rooij, *Journal of Micromechanics and Microengineering* **2007**, *17*, R50.
- [195] W. J. Fleming, *New Automotive Sensors—A Review*, **2008**.
- [196] K. Finkenzerler, *RFID Handbook: Fundamentals and Applications in Contactless Smart Cards and Identification*, Wiley, **2003**.
- [197] H. Lehpamer, *RFID Design Principles*, **2008**.
- [198] R. A. Potyrailo, C. Surman, N. Nagraj, A. Burns, *Chem Rev* **2011**, *111* (11), 7315.
- [199] T. Ndlovu, O. A. Arotiba, S. Sampath, R. W. Krause, B. B. Mamba, *Sensors* **2012**, *12* (9), 11601.
- [200] H. Yin, Y. Zhou, S. Ai, R. Han, T. Tang, L. Zhu, *Microchim. Acta* **2010**, *170* (1-2), 99.
- [201] V. Scognamiglio, I. Pezzotti, G. Pezzotti, J. Cano, I. Manfredonia, K. Buonasera, F. Arduini, D. Moscone, G. Palleschi, M. T. Giardi, *Anal. Chim. Acta* **2012**, *751*, 161.
- [202] F. Lu, M. Sun, L. Fan, H. Qiu, X. Li, C. Luo, *Sens. Actuators B-Chem.* **2012**, *173*, 591.
- [203] M. J. Moreno, P. D'Arienzo, J. J. Manclus, A. Montoya, *J. Environ. Sci. Health. B* **2011**, *46* (6), 509.
- [204] K. V. Ragavan, L. S. Selvakumar, M. S. Thakur, *Chem. Comm.* **2013**, *49* (53), 5960.

## 구문초록

최근 물리적, 화학적, 전기적 특성이 개선된 나노 물질 연구와 새로운 나노 물질의 합성 방법이 재료 과학에서 지속적으로 발전하고 있다. 그 중에서도, 전도성 고분자, 나노 구조 금속 복합체 및 탄소 나노 재료를 포함하는 전도성 나노 재료는 그 고유한 특성으로 인해 많이 연구되어왔다. 1 차원 (1D) 전도성 나노 물질은 높은 종횡비와 높은 비표면적 및 빠른 방향 전하 수송 특성과 같은 단순한 구조 특성으로 인해 특히 센서 변환기로써 효과적인 것으로 알려져 있다. 1D 전도성 나노 물질 중 하나인 탄소 나노 물질은 공유결합,  $\pi$ -스태킹과 같은 다양한 방법을 사용하여 표면을 개질할 수 있어 전기 화학 및 생물학적 응용에 중요하다. 특히, 탄소 나노 섬유 (CNF)는 점성 고분자 용액을 사용하여 1D 나노 물질을 제조하는 방법 중 하나인 전기 방사법을 통해 간단히 얻을 수 있으며, 효율, 비용, 수율 및 재현성 측면에서 상대적으로 유리하다. 전기 방사된 탄소 나노 섬유는 온도, 방사 용액 성분, 전구체 조성 등을 포함하여 공정 조건을 변경하여 전기 화학적 특성 및 구조를 쉽게 제어할 수 있기

때문에 센서 응용 분야에 특히 매력적이다. 그러나 다차원 나노 섬유 생산 또는 하이브리드 나노 물질 제조에 있어서 전기 화학적 및 구조적 이점을 위해 안정적인 공정 최적화가 필요하다.

이 논문은 바이오 및 화학 센서 응용을 위해 전기 방사된 폴리아크릴로나이트릴 (PAN) 기반 다중 채널 탄소 나노 섬유를 사용하는 다양한 하이브리드 재료의 제조를 설명한다. 다채널 탄소 나노 섬유는 단일 노즐 공동 전기 방사 및 열처리를 통해 제조되었다. 다채널 탄소 나노 섬유는 바이오 센서 응용을 통한 센서 변환기로서의 유용성을 갖는 것을 확인할 수 있었다. 첫째로, 산 처리를 거친 다채널 탄소 나노 섬유의 카르복실기와 바이오 수용체의 아민기 사이의 촉매 반응에 따라 생체 수용체가 고정된 다채널 탄소 나노 섬유를 제조하였다. 생체 수용체에 따라서 내분비계 교란 물질 (비스페놀-A, BPA)을 검출하기 위해서 압타머를 사용하였고 타액 간질 바이오 마커 (네스파틴-1, NES1)를 검출하기 위해서는 항체를 도입하였다.

둘째, 열처리 전 산소 플라즈마 처리를 포함하는 손쉬운 방법으로 귀금속 (Ru) 및 금속 산화물 ( $Fe_2O_3$ ) 나노입자가 도입된 다채널 탄소 나노 섬유를 제안하였다. 루테튬

나노입자가 도입된 다채널 탄소 나노 섬유 (Ru-mCNF)는 신경 전달 물질 분자 (도파민)의 검출을 위해 사용되었고, 산화철 나노입자가 도입된 다채널 탄소 나노 섬유 (Fe-mCNF)는 독성 가스 (황화수소)를 검출하기 위해 적용되었다.

이 논문은 다채널 및 다공성 구조로부터 유래된 큰 활성 표면적으로 인해 바이오/화학 센서 응용에서 초고성능을 나타내는 다양한 유형의 다채널 탄소 나노 섬유 기반 하이브리드 나노 재료의 가능성 및 용이한 제조 방법을 제공한다. 이 논문에 제시된 나노 물질은 액체 이온 게이트 바이오 리셉터 (압타머 또는 항체) 전계 효과 트랜지스터 (FET) 센서, 비 효소 형 FET 센서, 독성 가스 무선 화학 센서 플랫폼과 같은 다양한 감지 시스템에 도입될 수 있다.

주요어: 다채널 탄소 나노 섬유; 금속 나노입자; 내분비계 교란 물질; 타액 간질 바이오 마커; 신경 전달 물질; 독성 가스; 센서.

학 번: 2014-21583